Technical University of Denmark

DTU

Nanostructuring with Bonding and Structural Studies of Plasma Assisted Wafer Bonding

Poulsen, Mette; Jensen, Flemming; Feidenhans'l, R.

Link back to DTU Orbit

DTU Library
Technical Information Center of Denmark

Nanostructuring with bonding and structural studies of plasma assisted wafer bonding

Mette Poulsen
Ph.d Thesis
MIC - Department of Micro and Nanotechnology
Technical University of Denmark

February 2006

Abstract

The work presented within this thesis consists of two parts both related to wafer bonding and x-ray scattering.

The first purpose of this project has been to investigate low temperature plasma assisted wafer bonding. This was done by performing x-ray reflectivity measurements at the bonded interfaces in combination with other characterization methods e.g. bond strength measurements. The mechanism behind the low temperature plasma assisted bonding is unknown and the aim of the x-ray reflectivity measurements was therefore to obtain structural information about the bonding interface and thereby contribute to a better microscopic understanding of the system. The need for a more detailed microscopic understanding of the low temperature bonding process is important, both to optimize the process, but also to ensure stability of devices fabricated using the bonding step.

Oxygen plasma activated bonding of silicon wafers at room temperature has been investigated systematically using a reactive ion etch (RIE) and an inductively coupled RIE (ICP-RIE) system. The influence of various process parameters on the oxide thickness, bond strength and the density profile across the interface were studied, and the bond strength measurements were used to optimize on the activation process in order to obtain highest possible bond strengths. Highest bond strengths were found to be around to $1.6 \mathrm{Jm}^{-2}$, which is comparable to standard fusion bonded wafers annealed at 500-700 degrees.

The second purpose of the project was to use our knowledge within water bonding to fabricate x-ray wave guides. X-ray wave guides can be used to produce x-ray micro or nano beams with high flux and significant small cross section and open op a whole range of new area of applications within scattering, microscopy and spectroscopy with a real space resolution in the nanometer range.

The wave guides made and investigated in this project were made by etching nano structures in silicon wafers and using wafer bonding techniques for closing these etched structures. In this way nano dimensional air channels buried in silicon were obtained and since air is used as the guiding medium in principle no problems of intensity decrease caused by absorption were expected. The x-ray beam was coupled into the the guide from the front and for a certain combination of dimensions and incidence angles a standing wave inside the cavity is obtained. Far field intensities of the propagating modes were measured and compared to theoretical calculations. The success of waveguiding depends on the quality of the etch cavity structures. The roughness of the channel surfaces has to be minimizied and if guiding in two dimensions, it also has to be considered whether the sidewalls are perpendicular. The waveguide fabricated in this project was made by RIE etching and both one dimensional and two dimensional wave guiding were observed.

Resume

Formålet med dette projekt har været at undersøge lav temperatur plasma assisteret wafer bonding ved hjælp af røntgen reflektivitet, fremstille og karakterisere røntgenbølgeledere ved brug af wafer bonding samt at undersøge interfacet af bondede wafere, bonded med krystal orienteringen af waferne drejet eller tilted i forhold til hinanden. Afhandlingen vil behandle de første to af disse emner.

Plasma aktiveret lav tempertur bonding er interessant, da man kan opnå en høj styrke af bondingen allerede ved stuetemperatur. Dette gør metoden anvendelig til fremstilling af komponenter der er varmefølsomme og derved ikke kan fremstilles ved konventionel waferbonding. Årsagen til den høje bonde-styrke og den generelle mekanisme bag processen er stadig uklar og formålet med vores målinger var at undersøge bonde interfacet ved hjælp af røntgen reflektivitet. De strukturrelle undersøgelser blev kobineret med standard karakteriserings metoder indenfor waferbonding teknologi.

To typer af aktiverinssystemer er blevet undersøgt i forhold til, hvordan forskellige process parametre påvirker bondestyrken og strukturen af bondegrænsefladen. Process parametrene for de to systemer blev optimeret i forhold til bondestyken og bondestyrker på optil 1.6 Jm^{-2} blev målt. Dette svarer til bondestyrken af direkte hydrofob bondede prøver opvarmet til 600 - 700 grader.

Den anden del af afhandlingen er relateret til fremstilling af bølgeledere ved brug af standard silicium process teknologi i kombination med waferbonding. Anvendelsen af røntgenbølgeledere til at fremstille intense velfokuserede micro eller nano beams åbner op for et helt nyt område indenfor spredning, microskopi og spectroskopi med opløsninger ned i nanometer området.

Vi har fremstillet både en og to dimensionale strukturer i silicium, og succesfuldt demonstreret at de fremstillede strukturer udviser bølgeleder egenskaber. Ved at bruge luft som guide medium er vi ikke begrænset af absorbtion og kan derved lettere opnå enkelt mode guiding.

Preface

This thesis has been written as a partial fulfillment of the requirements for obtaining the Ph.D. degree at the Technical University of Denmark (DTU). The Ph.D. project has been carried out at the Department of Micro- and Nanotecnology (MIC) at DTU and at the Materials Research Department at Risø National Laboratory in the period from July 2001 to February 2006. All the x-ray experiments were performed with the wiggler beamline BW2 at the Deutches Electronen Syncrotron in Hamburg and at the ID1 beamline at The European Synchrotron Radiation Facility (ESRF), located in Grenoble, in close collaboration with the x-ray group at Risø. The preparation of samples was mainly done in the cleanroom facilities at DANCHIP, DTU. The project has been supervised by Professor Robert Feidenhans'l and Flemmig Jensen and has been funded by Statens Naturvidenskabelige Forskningsråd (SNF).

The project was a collaboration between MIC and Risø. A lot of people both from MIC and RISØ have been involved, and I am very grateful for all the fruitful discussions and for the contributions to the work. Specially I would like to thank the following people:

First of all, I would like to thank two my supervisors:
Robert Feidenhans'l for great collaboration, contributions and guidance. It has been very inspiring for me working with you throughout the project. Despite you are a busy man with a very booked calender you always took time for discussions, solving problems and participating in the experimental work.

Flemming Jensen also for great collaboration and guidance in the cleanroom process development. It has been a pleasure discussing and working with you.

I would also like to thank specially Oliver Bunk for good collaboration, discussions and always being helpful. You have been a good and patience teacher during the work, especially at the beam line.

Further I would like to thank Anne Egebjerg, who wrote her master thesis within the subject plasma assisted bonding, for good discussions and hard work in the cleanroom. I admire your "love of order", which was sometimes really needed.

I would like to thank Dag Breiby and Anette Jensen, who have been a great help during the work with the waveguide with both theoretical calculations and with performing the x-ray measurements, and Martin Nielsen, who developed the programme used for analyzing the

Contents

List of Figures

Chapter 1

Introduction

The work within this project can be divided into three main parts all related to wafer bonding and x-ray scattering. Semiconductor wafer bonding is a technique known for many years used for joining materials together, and it has been used widely within the microelectronic and -mechanical industry for fabricating complicated structures and devices. X-ray scattering is also a well established field and with the development of strong synchrotron radiation it has become a strong tool for structural investigation of materials.

The three subjects that has been worked with are:

- Structural investigations of low temperature plasma assisted bonding.

- Fabrication and characterization of x-ray wave guides made by silicon wafer bonding.

- X-ray investigations of twist and tilt bonded wafers.

The first two of the three subjects will be discussed in details in the thesis, while the third one only shortly will be commented later in this chapter. To get an overview of the aims within the subjects some short comments are made on each of them including a presentation of the overall structure of the thesis.

Structural investigations of low temperature plasma assisted bonding.

In plasma assisted wafer bonding the surface is activated prior to the room temperature bonding step. The activation can be made in different ways, but the most common method to use is activation in a plasma chamber using either an oxygen or an argon plasma. After the activation the surfaces are very reactive and when bonding the two wafers very high bond strengths (measurement of the strength of adhesion) are observed all ready at room temperature. This is different from what is found when doing standard fusion bonding of hydrophilic or hydrophobic not activated wafers, which has to be annealed before same bond strengths are reached. The need for annealing makes the standard fusion bonding useless if heat sensitive devices have to be made. The annealing is not necessary if the surfaces have been activated and this makes the plasma assisted bonding attractive.

The mechanism behind the plasma assisted bonding and the influence of varying the process parameters within the activation process are unfortunately not very well understood. The fact that the bonding might be used to fabricate reliable devices like e.g airbag sensors is exactly the reason why good understanding of the bonding process is important. The aim of our project was to use x-ray reflectivity measurement in combination with other characterization methods to obtain detailed information about the interface structure and how it was influenced when changing the parameters in the activation chamber.

The work related to the investigations of the plasma assisted low temperature bonding is presented in the first part of the thesis, starting with a short introduction to general aspects of standard wafer bonding and low temperature bonding in chapter two. At the end of that chapter there is a short description of the cleanroom procedure for fabricating the activated bonded wafers. Chapter three is related to evaluation of the bonding quality. The most commonly used technique for evaluation, is measuring the bond strength using the razor blade method. This method is, even if it is widely used, very uncertain, and as a part of the project the method has been investigated in a student project. The result of that project,and a detailed discussion and evaluation of the method are also presented in chapter three. In chapter four there is a presentation of the optimization work. Pressure, power and activation time were varied in two different activation systems and the parameter combination resulting in the highest bond strengths was found. Chapter five contains a description of the used set-up in the x-ray measurements and the results from a selected amount of measured samples. The results are analyzed and density profiles for the interface are presented and discussed at the end.

Part of the work related to this subject of plasma assisted low temperature bonding has been summarized and published in [57], which can also be find in appendix C., and a paper of the final result of the x-ray measurements is in progress and scheduled to be published in the spring of 2006.

X-ray wave guides made by wafer bonding

The aim of the second subject, was to use our knowledge within wafer bonding to fabricate x-ray wave guides. The x-ray wave guides can be used to produce x-ray micro or nano beams with high flux and a significant small cross section and they are believed to be a useful device in the future for investigating e.g nano particles and structures or performing high resolution tomography.

Several types of wave guide structures have already been made and demonstrated, often having a PMMA core as the guiding layer and a Cr or Si layer as the cladding material. We propose to make both one- and two-dimensional x-ray wave guides in a simple way using standard silicon technology in combination with hydrophobic wafer bonding. The wave guides in our project were made by etching nano structures in silicon wafers and using the wafer bonding techniques for closing the etched structures. In this way nano dimensional air channels buried in silicon were obtained and since air is used as the guiding medium in principle no problems of intensity decrease caused by absorption are expected. Using air

as the guiding medium makes it possible to operate at lower energies, and since the mode separation depends increase as a function of energy this makes it easier to obtain single mode guiding.

Both one and two dimensional cavities were fabricated and characterized and wave guiding was successfully observed. The results from the work are presented in the second part of the thesis, starting with an introduction in chapter six. Chapter seven contains the theory necessary for describing the mode propagation, and what to expect when measuring the far-field intensities of the modes. At the end of the chapter there is a discussion of the coupling of intensity into the guide. In chapter eight there is a description of the fabrication. The used bonding technique is presented, and considerations related to bonding of structured are discussed. Further the chapter contains details about the used etching, and at the end some results of the pre-characterization of the etched structures can be found. In chapter nine there is a description of the x-ray measurements and some examples of measured wave guiding are presented and discussed. Finally in chapter ten is a conclusion on both subject.

The work related to the one dimensional waveguide measurements is published in reference [58], which is also to be find in appendix C. A paper of the results from the two dimensional guide is in progress.

X-ray investigations of twist and tilt bonded wafers.

The last subject that has been worked with is related to twist and tilt bonding of silicon wafers. Twist and tilt bonding refers to the bonding of two Si(001) wafers where the crystal plane of the wafers are not perfectly matching at the bonding interface. Instead they are either rotated or tilted proportional to each other. Bonding the wafers with a small well defined misorientation will result in a strain field created at the bonding interface, characterized by a periodic lattice of dislocations. As the period is related to the angels of misorientation, it can be controlled by controlling the angle. The periodic strain field will penetrate into the wafers, with a penetration depth also related to the misorientation. Further, if the upper crystal is thin enough the strain fields will penetrate to the top surface. Such bonded wafers are interesting as they can be used as templates for e.g. epitaxial growth or ordered arrays of nanoclusters or for creating nanometer periodic surface structures by selective etching.

As a part of the project a process recipe has been developed for fabricating such bonded wafers. This was done by thermal oxidation of a SOI wafer (silicon wafer with an oxide and silicon on top) resulting in a wafer with only a few nanometer of silicon. This thin silicon layer was then bonded to another silicon wafer in a way, such that the misorientation angle was controlled and the bonded wafers were annealed at different temperatures. The top wafer was now relatively thin and the strain field will be able to penetrate to the upper surface. The strain field at the interface was investigated by x-ray scattering and a theoretical model description was made. The upper surfaces were investigated by STM. From these investigations, it was speculated that the strained top crystal was relaxing as a function of temperature, and an experimental set-up for measuring x-ray in situ scattering from the

interface as a function of temperature was made.

Results from investigation of the strain field from ultra thin bonded Si wafers can be found in [47], also included in appendix C.

Chapter 2

Plasma assisted wafer bonding

Plasma assisted or activated wafer bonding is a special type of wafer bonding, which was developed as a new method for bonding semiconductor devices at low temperatures. In this chapter, general aspect of wafer bonding and the cleanroom procedure related to the fabrication of plasma assisted samples are presented.

2.1 Wafer bonding

Direct wafer bonding or fusion bonding is a process, where two clean and smooth surfaces are brought into proximity and adheres at room temperature. No macroscopic layers or applied forces are coercing the process. The process is spontaneous if the quality of the surfaces are sufficiently good. The principle is illustrated in figure 2.1
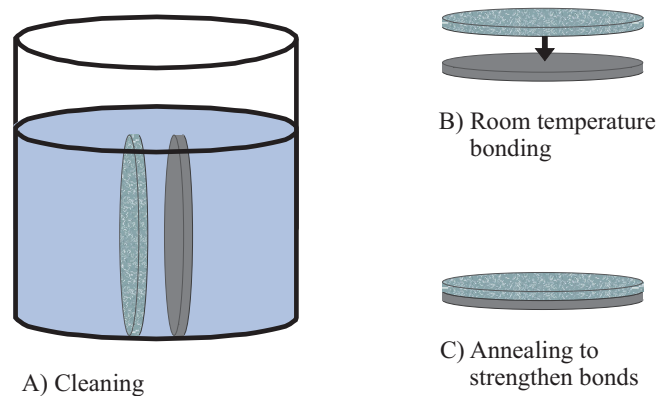
Figure 2.1: [21] Schematic illustration of direct bonding process. Three basic steps are involved in direct bonding: A) a cleaning step, which is used to rinse off particles and impurities, B) adhesion of the two wafers and formation of bonding and C) an annealing step, which is included to reach a reasonable bond strength.

The three steps in figure 2.1 are the basic steps involved in wafer bonding, but additional steps can be added depending of the specific choice of wafer bonding type. E.g for plasma assisted bonding, where the surface of the wafers are modified within an activation chamber

prior to the room temperature bonding (step B). The term bonding refers to the contacting of two wafers and formation of chemical or physical bonds at the interface. When the two wafers are brought in contact, a bonding wave will spread in a few seconds from the contact point to the edge of the wafers. It is important only to make a single contact, since otherwise air can be trapped at the interface, resulting in voids of unbonded areas. Further the process is very sensitive to particle contaminations and can only be carried out in clean environments.

The basic technique of wafer bonding has been known for many years based on the pioneering work of Rayleigh [60] back in 1936, where adhesion of two polished glass plates were examined. In the mid eighties an increased interest and further studies of Rayleighs work lead to the concept of wafer bonding known today, and indeed within the latest years, a widespread interest in modern bonding techniques has grown as a result of needs in the microelectronics industry. In the beginning it was mainly intended as a substitution of thick epitaxial growth on Silicon and to realize a Silicon-On-Insulator (SOI) structure, but it has developed as a widespread technique to construct layered devices.

Plasma activated bonding is a rather new method of bonding, which has been used since 1988, where the group of Tong reported on their experiences with Cool Plasma Activated Surface in Silicon-Wafer Direct Bonding Technology [68]. The first patents and papers documenting the use of Oxygen Plasma Activation in wafer bonding were presented in the early nineties. The technique was interesting, since it fulfilled the demand of low temperature, that many components require. E.g. in the bonding of dissimilar materials, where difference in thermal expansion induce stress in the sample and cause it to crack, or for sensors and other types of applications, where the accurate position of a heat sensitive material is vital.

The need for a more detailed microscopic understanding of the low temperature bonding process is a major concern, both for optimizing on the process, but also to ensure long term stability of devices using the bonding step within the fabrication. The technique has now been known for many years and several groups begins to see, that the bond quality is changing as a function of time on a long time scale and in worst cases debonding is observed[22]. In order to avoid these problems and if the low temperature wafer bonding is going to be used as a reliable technique in future applications, a better understanding of the bonding process is crucial.

In this work only room temperature bonding is considered. The prime motivation was to investigate room temperature bonded samples and obtain information about the mechanism responsible for the increased bond strength compared to other bonding techniques. X-ray reflectivity is used as the main tool for the structural investigations in combination with several standard bonding quality evaluation methods. The application of x-ray reflectivity is new compared to investigations made by other groups within the wafer bonding area, and has also been applied by [14, 62, 63].

2.1.1   Surface interactions

Molecules and atoms attach to surfaces in two different ways, either by physisorption or by chemisorption. In psysisorption van der Waals interactions between adsorbate and substrate form the basis of the attachment, while in chemisorption, chemical bonds(usually covalent) are formed between atoms at the surfaces. The enthalpy is negative for most substrates, whereas it is a spontaneous process. In a simple bonding process, where no external forces are applied and no adhesion layer is added the bonding process might be explained by the interactions between the adhered surfaces. We divide the interaction into three types.

Van der Waals interactions

Van der Waals forces are the attractive interactions between closed-shell molecules resulting from charges of opposite signs. They are responsible for the attraction between electrically polarized and polarisable molecules. Intermolecular forces like van der Waals forces between small molecules are weak compared to intramolecular forces that bond atoms together within a molecule. On the atomic scale, they are considered to be long ranged, whereas they are short ranged on the macroscopic scale. There are three types of van der Waals forces; dipole-dipole attractions, ion-dipole attractions and London dispersion forces.

They are all diminishing rapidly as the distance between two molecules increases, $F_{vdW} \propto$ d^{-7}. Considering two flat surfaces, the force can be approximated by a summation of all the interatomic forces[70]:

$$F_{vdW} = \frac{A}{6\pi d^3} \tag{2.1}$$

where A is the Hamaker(adhesion constant specific for the materials regarded). The contacting surfaces has a separation of d_o and are considered as flat surfaces, and the interaction energy per unit area is given by[70]

$$W_{vdW} = \int_{d_0}^{\infty} \frac{A}{6\pi x^3} dx = \frac{A}{6\pi d_0^2} \tag{2.2}$$

The plasma assisted bonding considered in this project corresponds to bonding of two silica surfaces. For such medium the Hamaker constant A is $6.5 \cdot 10^{-20}$J and based on earlier proposed structures of hydrophilic bonding[70], where the bonding takes place through several water molecules [70], d_0 is known, and expression 2.2 can be used to calculate the van der Waal interaction energy. Typically values are found to be in the range of 1.3 - 17.1 mJ·m^{-2} depending on the assumed number of intermediate water molecules (d_0) [21].

To relate these force values to a surface force appropriate for the considered system, bond strength measurements are considered. Bond strength measurements is a standard evaluation method of wafer bonding and is described in more details in the next chapter. From bond strength measurements typical values of 1500 $mJ \cdot m^{-2}$ is reported for the bonding and this is 100-1000 times larger than the calculated van der Waal values. Thus it is ev-

ident, that van der Waal forces are not the only responsible factor in the bonding mechanism.

The energy necessary to break bonds on bonded Si(100)surfaces that are dominated by hydrogen bonds is in the range of 400 $mJ \cdot m^{-2}$ [21]. This is considerable higher than the van der Waals forces, but still does not reach the bond strength values obtained in this project. The energy for a covalent bonded surface is approximately a factor of ten larger($4000 \ mJ^{-2}$) than the energy related to hydrogen bonds, but this is beyond the measured values, and a bonding interface, which is dominated by pure covalent bonds will not be a correct description.

Coulomb forces

The second types of interaction is the Coulomb force. Charge is macroscopically transferred to the surface of wafers as electrons or ions are adsorbed or desorbed. The charged surfaces may cause electrostatic forces to dominate the forces between interfaces. Nonetheless, this effect is insignificant when water or water vapor are present in the environment. In the basic clean room procedure of this project, a water dip is included just before bonding which presumably counteracts eventual charges on the surfaces, and Coulomb forces becomes superfluous.

Capillary forces

The last forces to be mentioned are capillary forces. They arise when the two surfaces are in a vapor which can condense on the surface. If the condensed liquid has a contact angle less than 90 degrees and if the gab between the surfaces are smaller than a critical distance it can be filled by a capillary condensed liquid and resulting in an additional capillary attractive force. The critical distance depends on the radius of curvature of the condensed liquid. Typically interaction energy originating from the capillary forces between two flat , hydrophilic silica surface is approx. 150 mJ·m^{-2} [70].

2.1.2   Hydrophilic and hydrophobic wafer bonding

Traditionally fusion bonding is divided into two main types, depending on the hydrophilic or hydrophobic nature of the wafers. Their surface termination - the outermost atomic layers - determines the possibilities of activation.

The naturally occurring oxide layer is an example of a hydrophilic surface-terminating layer. The formation is due to oxidation in atmospheric surroundings. The naturally occurring oxide might easily be activated by wet chemical treatment. H$^+$ as well as OH$^-$ react with siloxane bonds in the silica network to form silanol groups:

$$\text{Si}_2\text{O} + \text{H}^+ + \text{OH}^- \longrightarrow 2\text{SiOH} \tag{2.3}$$

Silanol groups are now present at the surface, and the two surfaces to be bonded are connected via the formation of hydrogen bonds between water molecules and silanol groups. Formation

of hydrogen bonds is crucial to the strength of hydrophilic bonded wafers at room temperature [70]. Different linkage possibilities between the surface terminating silanol groups and water molecules are illustrated in figure 2.2[70, 21].
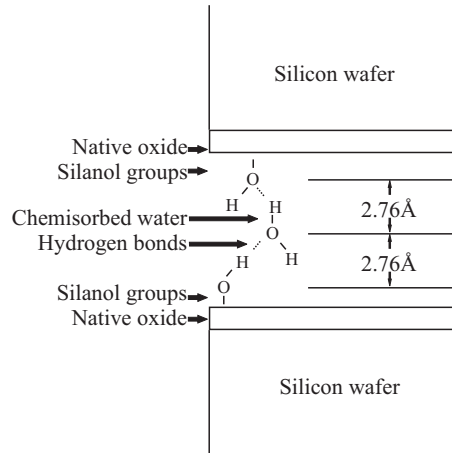
Figure 2.2: [21] Sketch of hydrophilic bonded wafers, and illustration of the different possibilities of linking silanol groups and water molecules via hydrogen bonds [70].

When adding two surfaces the hydrogen bonds are then capable of linking the surfaces through the use of water molecules. The number of linking water molecule layer differs depending on the specific surfaces and the bonding process environment. The use of water molecules reduce the demands of smoothness of the contacting surfaces, hence hydrophilic wafer bonding often is preferable especially when working at room temperature.

The hydrophobic surface termination is reached by removing the naturally appearing siloxane bonds in the oxide layer. Etching by use of HF eliminates oxide, whereupon SiF molecules at the surface react with water in the ambient:

$$\text{Si-O-Si} \overset{HF}{\rightarrow} \text{SiH} + \text{SiF}$$
$$\text{SiF} \overset{H_2O}{\rightarrow} \text{SiOH}$$

(2.4)

As the surface reacts with water in the ambient air and will turn hydrophilic, bonding of hydrophobic wafers has to be carried out immediately after etching.

In general the room temperature bonding is relatively week and annealing has to be performed in order to increase the bond strength. In figure 2.3 is illustrated how the bond strength increases as a function of annealing temperature. Further it is general known that the bond strengths of both the hydrophobic and hydrophilic type increase with storage time and reach a stable level after a few days [70].
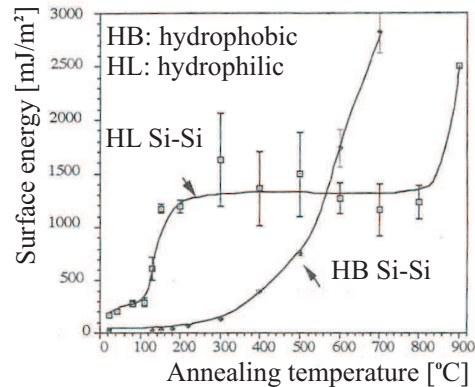
Figure 2.3: Bond strength variations for hydrophilic and -phobic wafers plotted against T [70].

2.2   Low temperature fusion bonding

The annealing temperature needed to form sufficient bond strength is for many practical applications a limiting factor. Depending on the application the minimum bond strength needed for a stable and reliable component might vary.

Samples made from standard hydrophobic and hydrophilic wafer bonding in general has to be annealed at relatively high temperatures whereas Plasma Activated Bonding is different by a having high bond strength already at room temperature. Using plasma activation, bond strengths in the interval 1000-1600mJ·m^2 (20ºC) have been obtained by several groups [64, 69], which is comparable to the strength of hydrophobic bonded wafers annealed at approximately 520-600ºC [70]. The bond strength of plasma treated samples reaches approximately 50% of the value for fusion bonded samples annealed at 1100ºC and is higher than the bond strength for the bonding used in a glass-silicon sensor. More details about the physics and chemistry of the plasma used can be found in [41, 75, 10, 44]

Several papers are published on different investigations of the plasma activated surfaces and bonding, but despite of the many results, basic understanding of the mechanism, in particular on the atomic level, is still missing. Conflicting results are stated, and the effect of the variable process parameters are not clear. It is believed, that water treatment of the activated surface plays an important role, either because its rinsing contamination induced by in the activation system away, or because its used for better linking of the surfaces at room temperature. The bond strength is reported to change as a function of both storage time and annealing, and in general it is believed the interfacial water rearrange and moves away from the interface and that part of the water is diffusing into the oxide generated from the activation process.

The plasma assisted bonding is a sensitive process and keeping track on how the different variables affect the system is difficult. The systems used by the different groups can behave different, even though same activation recipes are used, and the bonding procedure, con-

cerning environment, equipment and the step involved in the procedure are not necessary identical. Especially the time play an important role, both regarding the time passed from activation of the surface to the actual bonding, since the surface is believe to be extreme reactive, and also the time passed after the bonding to the characterization measurements Further the evaluation methods used often differ significant making it even more difficult to compare the results.

Examples of interesting related work can be found in references [3, 76, 8, 18, 19, 20, 33, 46, 52, 61, 7, 67, 77, 79]

2.2.1 Cleanroom procedure

All steps in the clean room procedure from cleaning to bonding are depicted in figure 2.4 below.

The chemicals used to clean the wafers are a solution designed to remove insoluble particles, organics and some metals called RCA1. Components in RCA1 cleaning solution are De-Ionized (DI) water, hydrogen peroxide (H_2O_2, 31%) and ammonium hydroxide (NH_4OH, 25%) in the ratio 5:1:1. The forces, which are responsible for the adhesion of particle contaminants to the surface, are mainly electrostatic forces induced by static charges, van der Waals forces, capillary forces and possibly chemical bonds as well. RCA1 is cogitated to reduce the strength of attractive forces and the surface energy. The surface of the particles is consequently modified, and particles are separated from the surface. As NH_4OH attacks the Si surface a native oxide layer will be present after the RCA1 cleaning, and a 5% solution of hydrofluoric acid, HF, were used to remove oxide. The surface is afterwards terminated by Si-H and Si-F bonds.

All wafers were RCA-1 cleaned using the following recipe:

RCA-1	70°, 10min
DI water	1min
DI water with N_2 bubbles	2min
HF	30s
DI water	2min

They were subsequently dried in a spin drier for 220s at 1400rpm. Long spin drying time were found to be necessary for obtaining successful bonding. Transport of the wafers inside the cleanroom took place in a plastic box.

The wafers were activated in either the RIE or ICP-RIE chamber. Description of recipes and optimization of these are found in chapter four. The thickness of the plasma generated oxide layer was measured by ellipsometry immediately after the activation, and the time between activation and bonding was kept as short as possible.
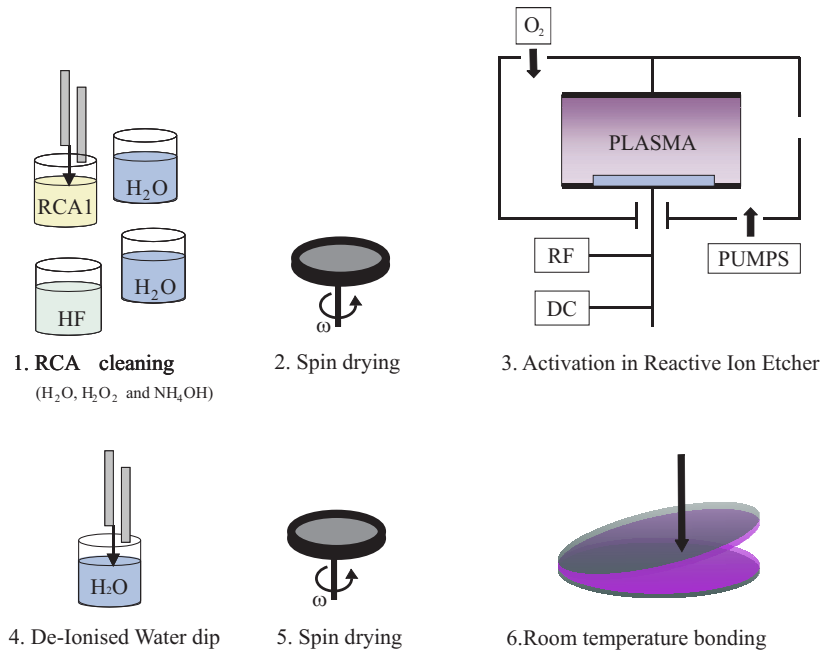
Figure 2.4: Schematic overview of the applied plasma bonding process.

2.2.2   Activation methods

Two different activation systems has been used within this project, an Reactive Ion Etching system (RIE) and a Inductive Coupled Plasma - RIE system, ICP-RIE. For both system oxygen were used for activation.

RIE-system

One of the two systems that has been used in this project to activate the surfaces is the Reactive Ion Etching (RIE) system. Several other plasma assisted dry etching methods are available and have been used for the purpose of low temperature bonding, but will not be described here.

In the RIE system a combination of a physical and chemical processes occurs. The surface is etched in a gas phase by an ion bombardment and reactions with a reactive specie at the surface takes place. The main components in the RIE is schematic illustrated in figure 2.5
The plasma generated in the RIE system is a self-contained part of the electrical discharge in the supplied gases. The plasma has electric and magnetic fields of high energy, whereas any gas will dissociate and, depending on their original composition, form ions, photons, electrons, reactive radicals and molecules loaded with high energy. It is featuring equal concentration of ions and electrons, which means that the plasma contains electrically active species, but as a whole is neutral.

The RIE technique is based on the glow discharge method using a RF-diode. The essential
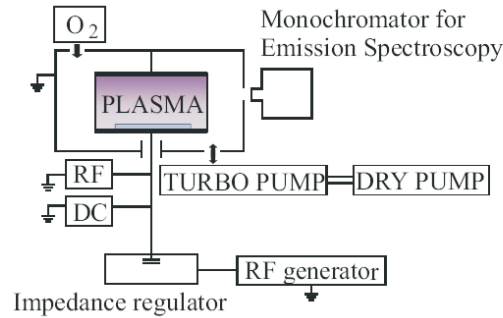
Figure 2.5: Sketch of the RIE system.[21]

part in plasma generation is two opposed and parallel plate electrodes at calibrated distance and a capacitive coupled RF generator. They are encapsulated in a tight chamber, where pressure and temperature are among the adjustable parameters. A gas, i.e. O_2, is filled into the chamber and the electrical potentials established here determine the energy of the ions and electrons colliding with the surface of the sample immersed into the discharge. Electrons are accelerated in an imposed electrical field. By collisions they transfer energy to the O neutrals, when the kinetic energy is greater than the ionization potential of O_2. The collision itself generates a new free electrons and positive ions. Electrons re-energizing and initiates an avalanche of ions and electrons. When the plasma forms, a glow is emitted, which is easily observed on a monitor connected to the chamber. The electrons from the partially ionized gas making up the plasma are mobile and diffuse fast to substrate surface immersed in the discharge, the opposite plate and chamber walls without any striking energy loss. Negative potential is consequently increasing at the sample and the plasma is drained and always turning positive. A current of the positive ions is thus induced and they are accelerated from the anode through the plasma to the cathode and thereby vertically pelting the surface. [21, 41]

Working with plasma assisted etching in place of wet etching methods is favorable in many ways. Only small amount of gasses are used and the process time is short. All chemical processes are performed in a closed chamber, which is cleaned before the wafer is unloaded. Harmful by-products are thereby encapsulated and more easy to control. The RIE etch has a very high precision and stability, making it easy to obtain precise etch results and reproduce the results repeating the process.

Inductive Coupled Plasma - RIE system

The second system that has been used for surface activation is the Inductive Coupled Plasma(ICP) - RIE system. The principles is almost the same as for RIE system, except that the plasma for this system is powered inductively by a power source with RF = 13.56MHz. Even though the systems are quite similar clearly differences can be seen in the x-ray reflectivity from the interfaces, indicating that the generated oxides on the surfaces are different for the two systems.

Figure 2.6 is an illustration of the principles and components in the ICP-RIE. The upper part is the helical resonator generating the plasma. The ion producing electrons are coupled to the field created by the RF generator and the plasma and field is separated by shielding in order to avoid capacitive coupling (used in RIE). A high coupling efficiency between the applied field and electrons in the plasma is obtained by tuning the impedance of the system to match the impedance of the plasma.
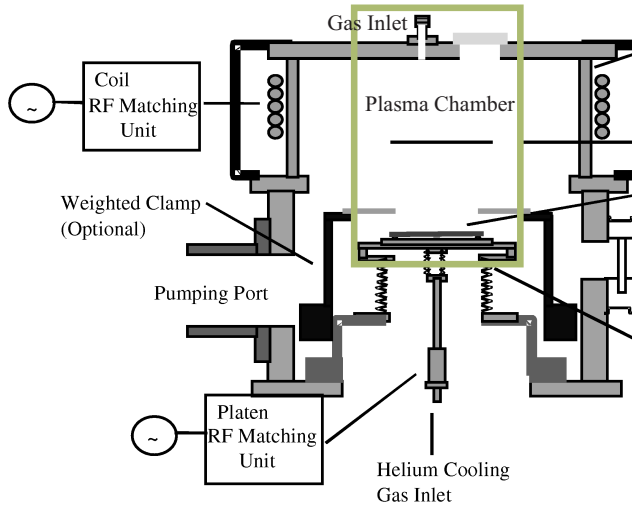
Figure 2.6: Sketch of ICPRIE system[21].

Coil and platen power is varied independently, which means that the amount of ions, neutrals and electrons consisting the etchant species can be controlled without adjusting the radio frequency. A high RF will cause surface damage, as the ion bombardment becomes too massive. The pump is a turbo molecular pump assisted by a dry pump as for the RIE. Helium is used to cool the sample, which alternatively is heated by energy transfer from the plasma. In the ICP-RIE low-energy plasma with a fast etching rate is produced. It is operating at low pressures, resulting in an increased directionality of the ions.

The most striking difference between the two plasma activation systems is the ion density of the plasma , which is very high in the ICP-RIE ($\approx 10^{12} cm^{-2}$) compared to RIE($\approx 10^9 cm^{-2}$). Conventional RIE systems do not have the possibility of operating at low pressures due to the parallel plate setup, which cause low ion density and thereby hinder plasma generation.

Optimization process has been made for both systems, varying the three parameters, temperature, pressure and power. Thickness variations and bond strength measurements as a function of the three parameters has been investigated combined with several other types of investigations. In general the ICP-RIE activated wafers are more hydrophilic than RIE activated wafers, which has been evaluated from contact angle measurements, and the spin drying time necessary before bonding. The results of the tests and the actual difference in the generated oxide layer can be found in the next sections.

Chapter 3

Evaluation of the bonding - quality measurements

Wafer bonding is a widely used technique within many areas of integrated circuit technology and microsystems, and the evaluation of the bonding quality is extremely important. Different techniques can be used for quality evaluation, where the bond strength has been considered as one of the most important characteristics to determine. By measuring the strength of the adhesion, general understanding of the bonding, bonding scheme optimization and quality control can be obtain, which are all important, when the wafer bonding has to be used within complex microelectro-mechanical systems.

In this chapter methods used to depict unbonded areas and to evaluate the bond strength are presented. In the first sections unbonded areas and methods for detecting voids at the interface are described. The inspection of voids are mainly done by shining infrared light through the bonded wafers, but also a short description of the Scanning Acoustic Microscopy(SAM) principle is presented. The next sections contains a description of surface energy measurements, where the crack test method has been used. This is the most common method for measuring the strength of the bonding. In this section details about the set-up are described and general problems of the crack test method are discussed. Due to all the problems related to the set-up and the method, the section also contains an evaluation of the setup used including a model discussion of the dynamics of the system. At the end a few examples of alternative surface energy measurements can be found.

The plasma assisted bonding in this project has also been investigated by TEM(Trans-mission Electron Microscopy) and TOF-SIMS(Time Of Flight Secondary Ion Mass Spectroscopy). These investigation are not described in this thesis, but can be found in [21]. In this thesis also more details about the SAM measurements can be found.

3.1   Unbonded interface areas

In the IR camera setup, infrared light is shined through the wafer pair. This is used for a rough inspection of the bonding after the two surfaces are bonded at room temperature. It easily reveals unbonded areas, voids, which are due to particles or other defects. It is

important to note, that it is a non-destructive inspection, which means, that the sample can be used afterwards. Further, it is a fast inspection technique, taking only a few seconds. The IR camera is also used in the crack test, were the strength of the bonding is measured by separating the bonded wafers by a razor blade (a destructive test).

3.1.1 Voids

Wafer bonding is a very sensitive process and the ambient air and handling of the wafers can affect the success of the bonding. All process steps depicted in figure 2.4 were carried out in a controlled cleanroom environment at Danchip [1], DTU. Unbonded areas, voids are grouped in two categories; voids forming immediately under the direct bonding step and those, which arise later during the storage, heat treatment or thinning procedures[70].

The voids induced throughout the bonding at room temperature can be caused by several reasons:

- particles on the surfaces

- surface protrusions

- insufficient density of activated plasma

- air trapped at the interface, e.g. if more than one bonding wave is induced

As the forces responsible for the room temperature bonding are mainly short-range inter-molecular forces, it is necessary to have smooth, flat and reactive surfaces. Within the semiconductor industry, a chemical-mechanical polishing technique is used as a standard technique to obtain the appropriate smoothness when manufacturing Si wafers (RMS < 5Å) In this polish process, mechanical polishing is used to remove the native oxide layer and a chemical solution of SiO_2, KOH and H_2O is afterwards used as a chemical etch to remove the topmost damaged Si layers from the mechanical polishing. After the wafers have been chemical-mechanical polished, native oxide will grow on top again (2-10Å), and since the oxide may entrap impurities it is important to remove this layer immediately before the bonding. The cleaning method prior to the bonding should be chosen in order to maintain the surface smoothness. In this project the RCA1 cleaning solution was used followed by a HF dip.

The other category of induced voids is not directly related to contaminating particles, but appears later in the process during the annealing. Annealing of the room temperature bonded samples is used to enhance the strength of the bonding, and the choice of temperature and annealing time often depend on the demands for the specific device. Several groups have been investigating the problems with voids formation during the annealing and storage for different types of wafer bonding. It is an important phenomena since it diminishes the bond

---

[1]Danchip is the national cleanroom facilities at DTU. The clean room is classified as a class 100, where the equipment is placed. The air is changed 20 times pr. hour and the temperature and moisture are controlled in order to keep constant experimental conditions.

strength and in certain cases decrease the reliability of the devices made from wafer bonding. Even though it is an important discussion, we will not go in to further details, as our focus has been on room temperature bonding, and no voids were observed as a function of storage time.

The most convenient method to depict the voids depends strongly on the size of the generated voids, time consumption, cost and the materials used. The IR setup fulfills most of the demands, except the limited resolution.

3.1.2 IR pictures

The IR setup for detecting voids is based on optical transmission. The typical set-up is sketched in figure 3.1. It is a fast and cheap way to get an overall estimate of the bonding quality, but the use is restricted due to the limited lateral solution, which means, that smaller voids are not detected.
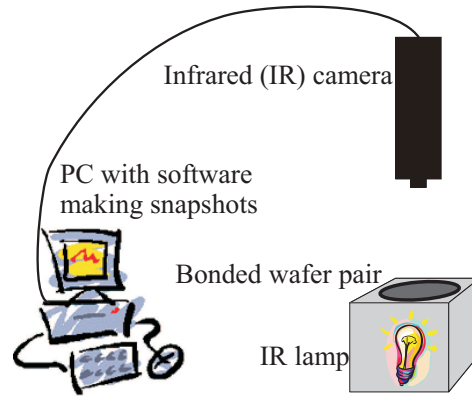
Figure 3.1: IR-setup[21]

Semi conductor materials strongly adsorb light except for frequencies fulfilling

$$\nu < \frac{E_g}{h} \tag{3.1}$$

where E_g is the band gap energy of the irradiated material and h is Planck constant. Using c = $\lambda\nu$, where c is the speed of light and λ the wavelength of the light, the condition can be rewritten

$$\frac{hc}{E_g} < \lambda \tag{3.2}$$

When bonding is carried out using materials non-transparent to visible light an appropriate wavelength of the transmitting light must be employed. As E_g for Silicon is 1.12eV light will pass through if $\lambda > 1.10\mu m$. The lamp used in the IR setup emits light with wavelengths ranging from $0.3\mu m$ to $2.6\mu m$, wherefor a part of the light is transmitted though the bonded silicon wafers. Depiction of voids containing either water or air is based on spectroscopic methods. IR spectroscopy deals with transitions between vibrational energy levels

in molecules and is therefore also called vibrational microscopy. The chemical bonds within molecules are in a state of continuan vibration, with bonds stretching and contracting as well as bending. When an infrared beam interacts with a molecule, waves of specific frequencies are absorbed by the molecule and the molecular vibrations are changed. The vibration frequencies of the waves that are absorbed depend on the types of bonds in the structure of the molecule. A molecule is able to absorb electromagnetic waves according to the selection rules of IR spectroscopy, if the dipole moment changes with the internuclear distance[1].
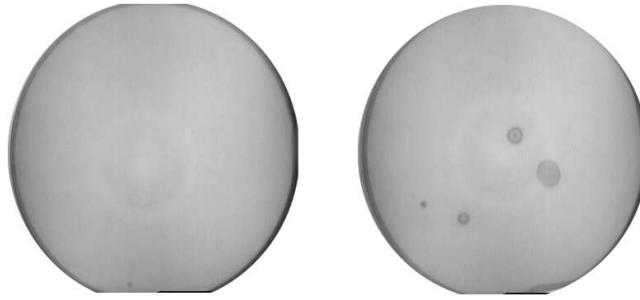
Figure 3.2: IR-pictures illustrating a successful bonded sample and typical voids respectively. Both samples are treated with O_2 plasma.

Figure 3.2 is IR-pictures illustrating a typical successful bonded sample and one with several voids. Both samples are plasma activated room temperature bonding. The white rings that appear on the pictures are artifacts of the system, and are not related to the interface. Voids are visible as dark spots with a number of interference fringes, and if the void is assumed to consists of air, the number of fringes, N, are related to the height, H of the void by [70]

$$H = N\frac{\lambda}{2} \tag{3.3}$$

In the method, voids down to half a fringe can be detected, whereas the minimum detectable void hight is $\frac{\lambda}{4}$. If light with wavelength $\lambda = 0.1~\mu m$ is used this corresponds to a height of $0.275~\mu$[70]. The minimum lateral size that can be observed depends on the resolution of the detector in the camera, and in our set-up, it is realistic to detect voids with a radius r>0.3.

SAM

Another non-destructive method for detecting voids is Scanning Acoustic Microscopy(SAM), where the lateral resolution is much better. The principles of the method are illustrated in the figure 3.3.
It is simply working as a sonar although operating at much higher frequencies (MHz-GHz). The bonded sample is placed in water, which works as a coupling liquid between the sample and the lens. An electric signal is converted to an acoustic plane wave by a piezoelectric transducer and the plane wave travels through a sapphire crystal and is refracted by a spherical lens, which focus the ultra sound. The sample is mechanical scanned, and the reflected signal is monitored by the sample transducer, separated from the input signal. Because the
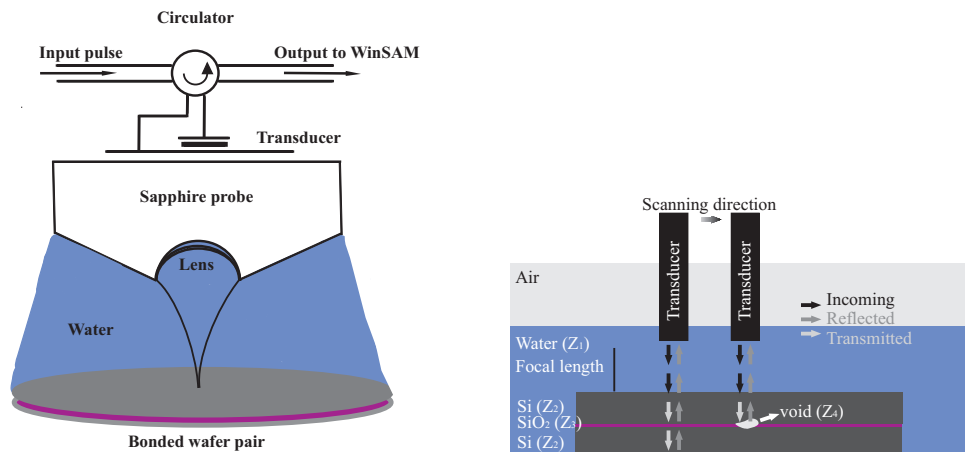
Figure 3.3: Sketch of SAM-setup[21]

scattering of the acoustic beam is focused to the bubbles at the interface of a bonded pair, the reflected signal is enhanced and thus the interface bubbles detected. The spatial resolution is limited by diffraction, thereby depending on the frequency of the acoustic beam. Using a frequency of 160MHz a resolution of $10\mu m$ is reported, which is much better than for the IR system.

Even though the resolution is much better for the SAM compared to the IR camera, the measurements are far more time consuming and the cost of the system relatively high. Further the measurements have to be performed in liquid, which can be a disadvantage for the weakly bonded wafers since the water can penetrate into the bonding during the measurements.

SAM investigation has been performed in this project [34], and compared to IR pictures of the same sample. Clearly more details were seen in the SAM pictures, where voids with a size of $30\mu m$ could be traced. An example of an SAM and IR picture is depicted in figure 3.4
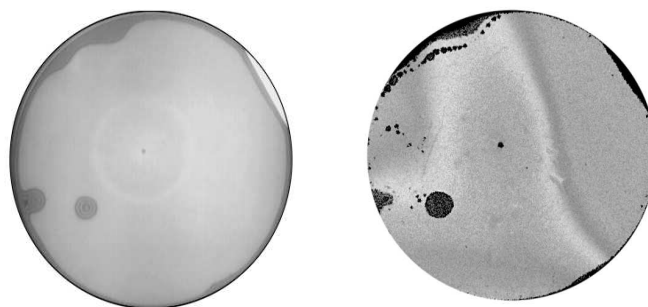
Figure 3.4: Plasma assisted bonded sample investigated with IR(left) and SAM(right)

As can be seen in the figure, the SAM picture is more detailed. The size of the voids are bigger and several smaller features in the left part of the bonded sample are now seen. Despite

the better resolution, the extra information obtained with the SAM system has to be valued against the extra time cost, and the limited access to the set-up. In conclusion we decided mainly to work with the IR-camera since with this system, it was possible to record pictures immediately after bonding for a series of samples and to follow changes on short or long time scale.

3.2   Surface energy measurements

The surface energy, γ is the energy associated with formation of a unit area of an appropriate surface and is used to characterize the strength of bonds formed after bonding of two wafers. Measuring the surface energy is done by separating the surfaces again after the bonding and therefore it is a destructive method.

The work, W, related to the mechanical separation of a bonded pair from an equilibrium distance d_o to infinity is described by [70]:

$$W = \gamma_{w1} + \gamma_{w2} = \int_{d_0}^{\infty} F(d)dx \tag{3.4}$$

where γ_{w1} and γ_{w2} are the surface energies of the two wafers at the moment of separation and F(d) is the attractive force per unit area as a function of the distance between the wafers, d. As the surrounding medium, often air, contains several species, which will be adsorbed by the freshly separated surfaces, the process is irreversible. Several methods for measuring bond strengths and bond strength models have been suggested and investigated, but as will be discussed during the next sections, measuring the bond strength is not straight forward. Still no adequate test system has been developed, and the typical setups used by different groups are not identical.

3.2.1   Crack opening method

Even though the crack opening method is the most common method, it is also one of the most discussed or even controversial methods, since the results are very dependent on the actual setup and the person performing the readout. The first group using the crack test was Maszara et al [40], which was using it in their investigation of silicon-on-insulator (SOI) wafers.

The crack opening method is based on equilibrium consideration of the elastic forces of the bent separated part of the bonded wafers, and bonding forces at the tip of the induced crack. The basic principle is sketched in figure 3.5.

When the bonded wafers are separated with a razor blade of thickness, t_b, the two wafers will bent and generate two different elastic energies, $E_{elastic1}$ and $E_{elastic2}$. Further the inserted blade also creates two new surfaces with area Lw, L being the debond length or the equilibrium crack length and w the width of the bonded sample under investigation. If it is
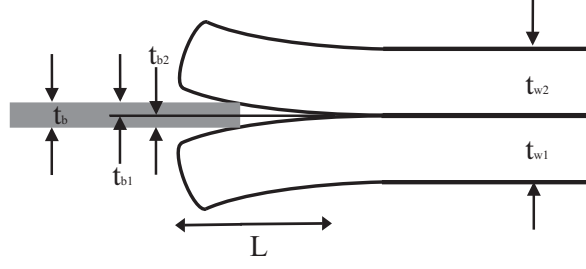
Figure 3.5: Principle of the crack-opening method assuming both wafers will bent.

assumed that no plastic deformations are involved in the separating process, the total energy is the sum of the elastic energies and the two surface energies multiplied by the area[70]:

$$E_{total} = E_{elastic1} + E_{elastic2} + (\gamma_{w1} + \gamma_{w2})Lw \tag{3.5}$$

and the equilibrium is determined by

$$\frac{\partial E_{total}}{\partial L} = 0 \tag{3.6}$$

The elastic energies are functions of Young's modulus, E and wafer thickness, t_w [70]

$$E_{elastic,i} = \frac{F_i^2 L^3}{6 E_i I_i} \tag{3.7}$$

where the bending force, F_i (i = 1,2) and the moment of inertia, I_i are defined as

$$F_i = \frac{E_i w t_{wi}^3 t_{bi}}{4L^3} \tag{3.8}$$

$$I_i = \frac{t_{wi}^3 w}{12} \tag{3.9}$$

t_{bi} is the thickness of blade fraction i, marked on the figure. Substituting these expressions into equation 3.5 and differentiating with respect to L the outcome is an equation for the surface energy:

$$(\gamma_1 + \gamma_2) = \frac{3t_b^2 E_1 t_{w1}^3 E_2 t_{w2}^3}{8L^4(E_1 t_{w1}^3 + E_2 t_{w2}^3)} \tag{3.10}$$

In the case of bonding of identical wafers, which is the situation for the samples investigated in this thesis, $t_{b1} = t_{b2}$ and $E_1 = E_1 = E$, and equation 3.10 becomes

$$\gamma = \frac{3E t_w^3 t_b^2}{32L^4} \tag{3.11}$$

where γ is the total surface energy of the bonded sample. Knowing the thickness of the wafers and of the razor blade used in the set-up, L is the remaining quantity to be determined.

One-wafer bending

Depending on the set-up it might be convenient to consider a system where only one of the wafers is bending during the crack test. This situation is illustrated in figure 3.6.
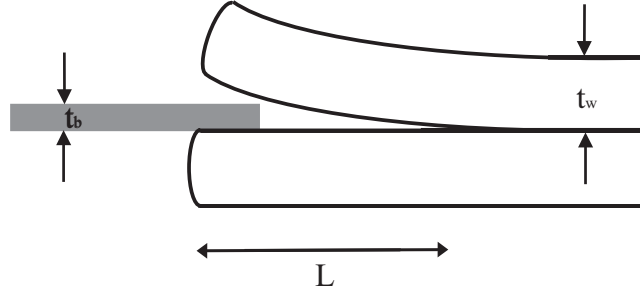
Figure 3.6: Crack-test with one wafer bend[21]

When actually measuring the debond length, a vacuum pump is often used to stick the wafer pair or a piece of it to a solid chuck (see next section for a sketch of the setup). This means when inserting the razor blade just above the edge of the bottommost wafer, only the upper one will bend during the test, and consequently the surface energy can no longer be described by expression 3.10. If we assume an ideal vacuum system and no contributions from the bottom wafer, it is determined by[70]:

$$(\gamma_1 + \gamma_2) = \frac{3Et_w^3 t_b^2}{16L^4} \tag{3.12}$$

The expressions are almost identical, except for a factor of 2 in the nominator, which means an increase of 50% compared to the two wafer bend case. Bending of only one wafer is a theoretical situation and even for systems with vacuum chucks it might be more precise to use an expression in between the two cases.

Comments on the model

The simple formulas stated, developed by Mazara et al., are neglecting shear stress and stress in the non separated part of the wafer specimen, where the latter omission arises from the approximation, that the wafer piece is rigidly clamped. In a recent published report by Vallin et al.[72] concerning the different methods for measuring bond strengths used today, several alternative models are presented including sheer stress and elastic restraint. These models have been compared to the Mazara model, and the result is depicted in figure 3.7.

The results are calculated for a bonded pair of each 525 μm thick silicon with the beam and crack in the $\langle 100 \rangle$ direction and a blade thickness of $50\mu m$. As can be seen in the figure
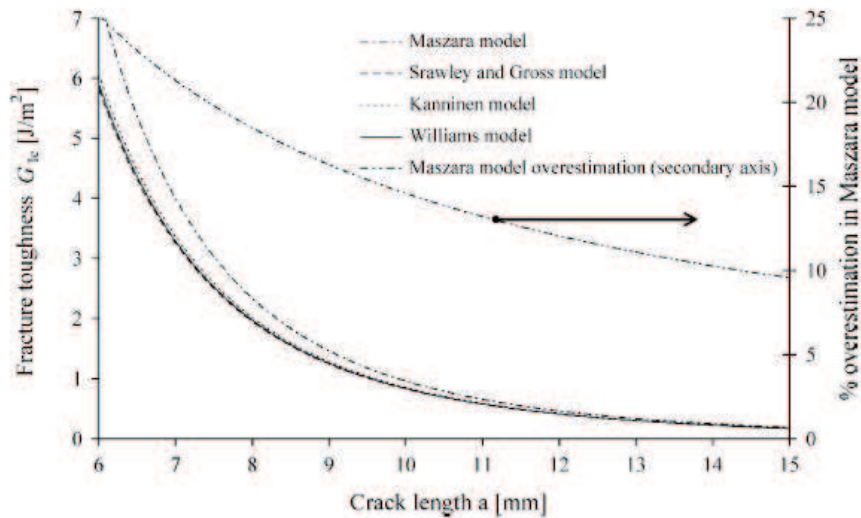
Figure 3.7: Comparison of fracture toughness obtained from four different models under prescribed displacement control. Mazara model, Scrawley and Gross model, Kanninen model and Williams model. The three latter models almost overlap. The percentage of overestimation using the Mazara model is shown by the upper curve and axis to the right[72].

Mazaras model yields an overestimation compared to the other models. The upper curve shows the percent of overestimation and for weakly bonded samples it is ap. 10 % and for stronger bonded samples even higher. The other models almost agree in results.

The results of the report clearly demonstrate, that in order to obtain a more precise description of the strength of the bonded sample, more detailed models are needed. In spite of the obviously inaccuracies Mazaras formula is still widely used. The reasons are, that it is relatively simple and other errors in typically crack test measurements are far more critical making exact strength calculation complicated. In this project, expression 3.11 has been used in the calculations.

3.2.2 Crack opening setup

The set-up used within our optimization process is depicted in figure 3.8.
A 2 cm wide test piece of the bonded wafer was placed on a metal block with vacuum holes. To assure stability, a stop block with a straight cut is placed at the end of the wafer piece. A razor blade made by sharpening a rectangular piece of spring steel was moved in the marked direction. It was controlled by two micrometer-screws mounted to the right, while a third micrometer screw (not drawn) enabled hight adjustment in the vertical direction. The setup is placed in an infrared camera box.

The micrometer screws were used to move the razor blade and debond part of the sample. The movement was done manually, and a series of pictures were recorded for each sample piece. When the blade is stopped a debonded area can be seen within the camera and it is
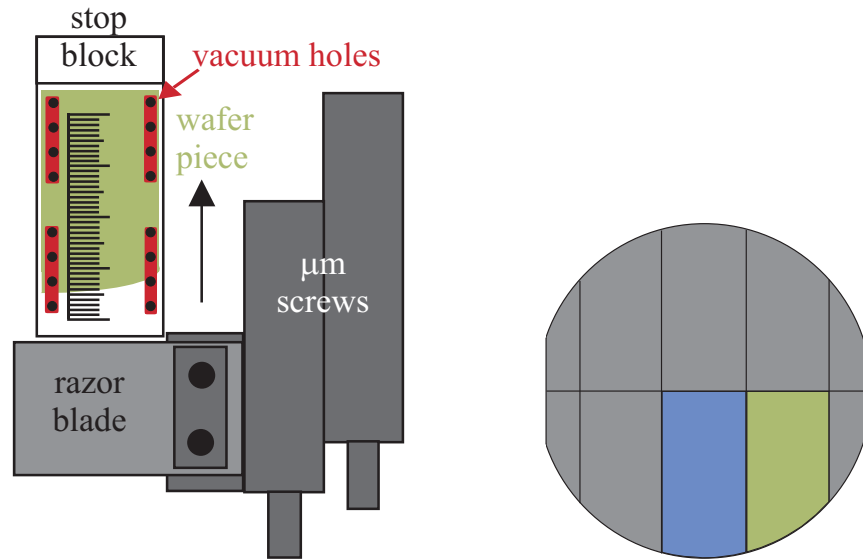
Figure 3.8: Left: Set-up of crack opening test device. Right: Diced wafer sample. Each 2 cm wide piece can be used to test the bond strength in the set-up depicted on the left. The test piece in the middle is colored in blue and the curved test piece in green.

this length needed to calculated the surface energy. An example of a sample series is shown in figure 3.9 below.
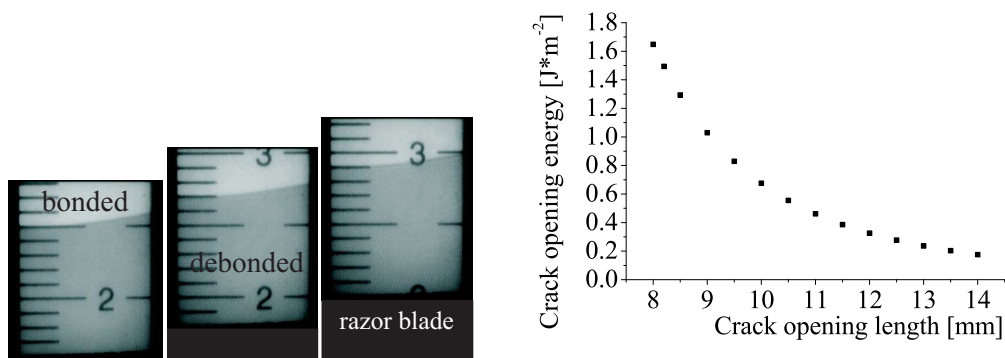
Figure 3.9: Left: Series of crack opening pictures showing the black area of the razor blade, the dark shaded area, where the wafers are debonded and the white area, where the wafers adhere. Right: Energy variations as a function of the crack length, L.

Splitting the wafers apart the razor blade and crack tip ideally move concurrently with each other. However, this requires a constant equilibrium situation between the competing forces described in equation 3.5, which is physically unreachable. The bond strength turns out to be strongly correlated with the surroundings[43, 72]. As soon as the surfaces are apart reactions with the surroundings begin to take place making, and the debond length will change as a function of time, even though the blade is stopped.

Since the debond front is moving, the time from when the blade is stopped to when the

debond length actually is measured is very critical and makes the test very depending of the operator of the system. The debond length L is entering equation 3.10 as L^4, making small changes very important for the resulting surface energy. The right part of figure 3.9 shows the crack opening energy as a function of the crack length.

For each bonded wafer pair, six to eight pieces were cut. For obtaining good statistics, several measurements were done on each piece and often two or more pieces from each wafer pair were measured. The mean value or the series of measurements were used as the debond length for the specific sample. The debond length were read out few seconds after the blade was stopped, where it seemed that the front was reaching a short time equilibrium value. This will be discussed in detail in the next section. The surface energy is calculated from expression 3.11 assuming both wafers to be bend, but due to the only partly fixed lower wafer this value will properly reflect the lower limit of the bond strength.

Although it seems like a lot of work to get the final results, the procedure is easy to overcome even for large amount of samples.

Comments on the crack test method and set-up

The precision of the measurements is determined by the instrument and by the system operator. Identical results can be reached using a less precise method, but this requires averaging over a large number of measurements, which is both time and cost consuming[72]. The precision is the degree of concordance between results obtained from measurements of the same physical quantity and can be dived into repeatability and reproducibility[72]. The repeatability is the precision within one measurement series and is an estimate of random measurements errors. The reproducibility is the precision in measuring the same quantity, but with altered circumstances like e.g. measurement method, another operator or other measurement equipment and describes the errors caused by instrumentation and people. The accuracy is the derivation from the physical quantity looked for. The degree of concordance between the measurement value and the true value is determined by the correctness of the mathematical models used and systematic errors such as those due to non calibrated measurement equipment[72].

The crack test is indeed easy to work with, and properly therefore it is still widely used despite of all its uncertainties. The test method and model were introduced in 1988 by Mazara et al. and has on the whole been used without further improvements since its introduction. Improvements has been suggested, but in spite of that there is still a lack of standardization allowing comparison of different published results. In general bond strength measurements are published without any comments on the exact set-up and in most cases only one single measurement is presented for each sample, making it hard to access the repeatability. Sometimes error bars are given, but without mentioning whether it is an estimate of systematic or relative errors, these are of no value.

For some measurements the repeatability is given and for these experiments a standard derivation in the crack length of less than 5 % is reported. This is in good agreement with

our measurements. More critical is the reproducibility which is mainly due to the dynamics in the measurements introduced by stress corrosion, and that the typically set-up still depends on the operator.

For investigating the reproducibility in the setup, we agreed to collaborate on testing the bond strength with two other groups, A. Sanz-Velasco et al. at Chalmers, Sweden and T. Suni from VTT information Technology in Finland. The test set-ups are all different, but based on the same principles of the two wafer bending methods. Each group prepared nine samples according to their own recipe with different wafer thicknesses and diameters. They were distributed such that each group measured bond strength on nine samples: three copies of each type. The results are plotted in a histogram in figure 3.10. Each color represents a measurements made by one group.
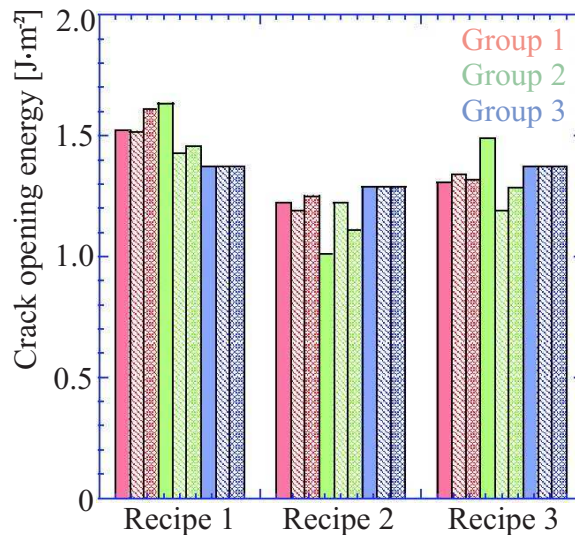
Figure 3.10: Bond strength values from the collaboration with two other laboratories[64], where each group prepared nine identical samples using individual recipes. Three samples of either type were tested in the different laboratory set-ups. The colors discriminates between test set-ups and the different patterns between the three tested sample types.

The blue columns represent two tests of whole bonded wafer samples and one on diced 20mm piece, whereas the green and magenta columns are the mean values of results only from pieces of a sample. The Mazara model used for calculating the bond strength is based on cantilever beams and in principle not valid for whole bonded wafers. This has been investigated by Baghdad et al.[4], who compared measurements on beamlike specimens and whole wafers. In general they found that measurements on whole wafers resulted in shorter crack lengths and thereby higher bond strengths. Our collaboration results are in good agreement with their observations, except for wafers prepared by recipe 1.

The variations within each colored measurements in each recipe are a measure of the repeatability, whereas the comparison of the three different color in each recipe is related to

the reproducibility. The blue measurements are always the same indicating good repeatability, but it has to be taken into account that the precision of their read out is $\pm 500 \mu m$ which is not as precise as our read out(green), where resolution down to 100-200μm was obtained. The situation is the same for the red measurements. Further the two latter are mean values of several measurements on each sample piece, which can explain that these are more fluctuating. For recipe 1, the bond strength values are varying from $1.4 J \cdot m^{-2}$ to $1.6 J \cdot m^{-2}$, which corresponds to a debond length difference of 0.3mm and therefore within the range of the read out uncertainties. In general good agreement is observed.

Another important problem in the measurements is, that solids under mechanical stress exhibit an increased chemical reactivity, also called stress corrosion[72]. It is believed that strained bonds at the crack tips are easily broken by reactions with molecules in the environment, making the time delay from when the blade is inserted to the actual read out crucial. The phenomenon has been investigated by several authors, e.g. Wan et al.[74], who investigated crack velocity versus fracture toughness in crack measurements of mica in different environments. They observed a very strong environmental dependence, and from their experiments it can be evaluated that the atmosphere wherein the measurements are performed indeed affects the results and that the velocity of the wedge/blade is important.

Similar experiments are made for bonded wafers by Bertholet et al.[9]. Their results are depicted in figure 3.11.
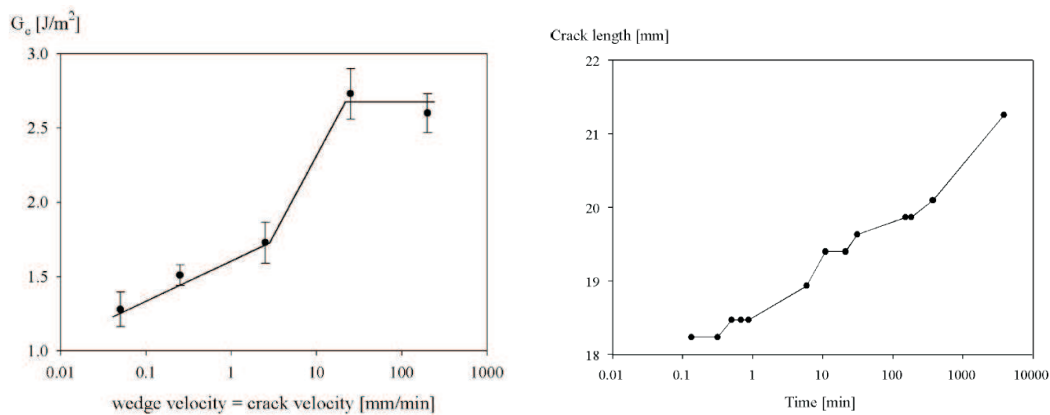
Figure 3.11: Left: Variation of the fracture toughness as a function of crack velocity. Measurements are performed on samples prepared by the same procedure (no specific surface treatment: 150 h annealing at 150 degrees). Right: Evolution of the crack length after stopping the wedge. The wedge is stopped at time t = 0 min [9].

In the left figure is showed a plot of fracture toughness versus wedge/crack velocity, and it can be seen that the fracture toughness depends on the velocity, and that the largest variations are in the velocity range of 0.1-10 mm/s. At high speeds the strength becomes constant. In the right figure is depicted a static measurement, where the wedge/blade is stopped at t=0. Here it can be seen that the crack length is increasing as a function of time, and in conclusion great care must be taken when performing static test for measuring the bond strength.

The collaboration results shown in figure 3.10 are all from static measurements, where the blade is inserted and stopped and the crack length subsequently determined. The waiting time before read out time were different for the three groups, group 1 was waiting two minutes, group two was recording the crack length immediately after separation and group 3 was waiting until the crack length was stabilized. These different waiting times can affect the resulting bond strength as illustrated in figure 3.11 and the different measured values can be explained by the different time delay. All measurements were performed in air, and therefore stress corrosion are indeed affecting the measurements. In the tests it was also observed that the crack lengths were changing with different velocities for the different used recipes, which can be related to different surface properties when changing process parameters and thereby different reaction rates with the surrounding water.

3.2.3   The dynamics of our crack-test setup

For obtaining more information on our own crack test set-up, we decided to investigate the dynamics of the crack length in details.

The used set-up was encapsulated in a plastic box where the humidity could be controlled by a nitrogen flow. The temperature in the box and on the sample were monitored. A series of tests were performed to characterize the behavior of the temperature and humidity within the box as a function of time.
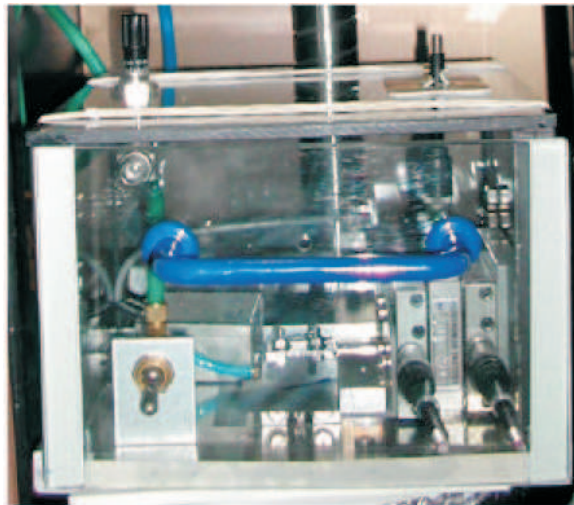
Figure 3.12: Test Box setup

The used set-up is depicted in figure 3.12. The humidity was measured at two points, as close to the sample as possible($\%rHd_{probe}$ in plots) and in the middle of the chamber($\%rHd_{ambient}$ in plots). The temperature was monitored at the same positions, T_{probe} and $T_{ambient}$ and also by a sensor placed directly on the sample, T_{dut}.
In figure 3.13 is a plot of measured humidities and temperatures in the box with and without a nitrogen flow. In the figure the blue curves are related to measurements without any
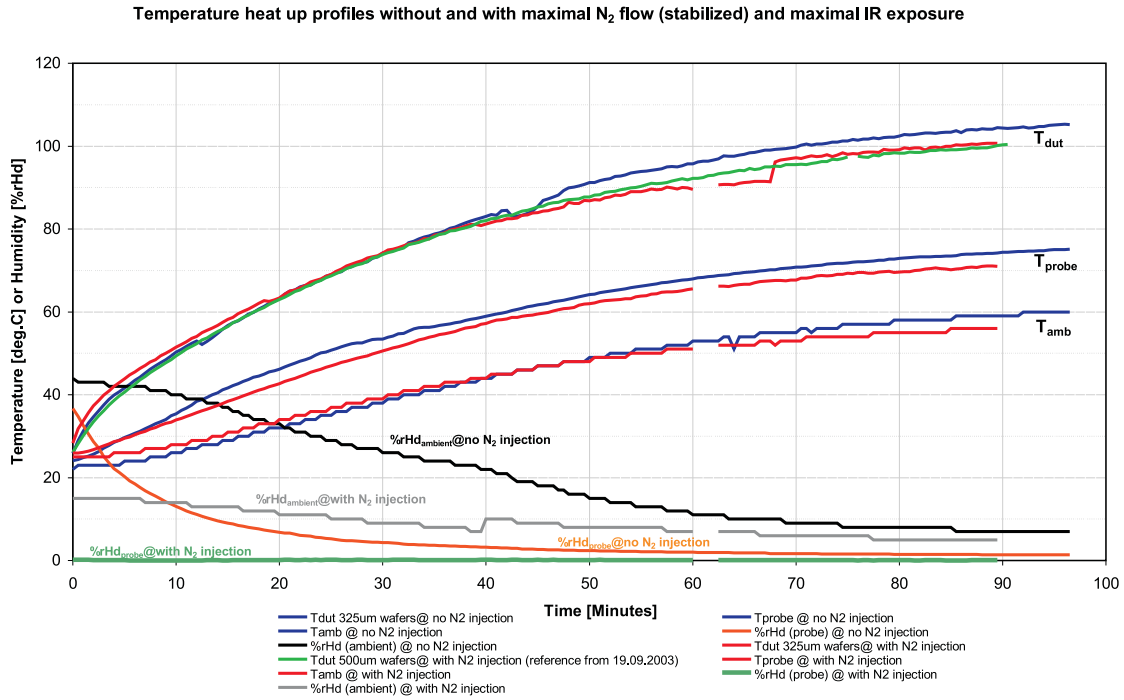
Figure 3.13: Temperature and humidity as a function of time

nitrogen flow and the red ones are with maximum flow. The green curve at T_{dut} is also with N$_2$ flow, but for thicker bonded samples. The IR lamp was in all measurements sat at highest possible intensity. In the bottom of the graph the relative humidities are plotted. The ambient results are the black (no N$_2$) and gray(max N$_2$) and the others are close to the sample, orange (no N$_2$) and dark green (with N$_2$). Based on the measurements the following can be concluded.

- The equilibrium temperature of T_{dut}, T_{probe} and $T_{ambient}$ with maximal IR exposure, tends to be 3-4$°C$ lower with the presence of N$_2$ flow (set to maximum), compared to the temperature without N$_2$ flow. The reason could be due to the cooling effect, arising from the temperature of the injected N$_2$ gas, which is approx 20.7$°C$.

- When the sample was exposed to a maximal IR intensity, the final equilibrium temperature of the wafer sample was found to be approx. 100$°C$, with a heat-up time constant of approx. 2000sec. (or 34 minutes). This means, that within the first 2 minutes, after IR activation, the temperature increases with approx. 10$°C$. If no N$_2$ gas is injected into the system, the relative humidity ($\%rHd$) near the wafer sample will drop 10% within the same period of time (orange curve).

- With maximal N$_2$ injection and no IR exposure, the equilibrium relative humidity ($\%rHd$) measured with the probe (placed near the wafer sample) was found to be

approx. 0-0.1% The ambient equilibrium relative humidity, was found to be approx. 15-20%.

- With the no N_2 injection and a maximal IR exposure, the equilibrium relative humidity, measured with the probe, tends to be approx 1.4%. Also, within the first 2 minutes after activating IR, the relative humidity drops from approx. 36% to 28%.

In the beginning it was assumed that maximal IR intensity should be used, mainly because the picture quality of the AVI movie sequence would increase. However, this approach soon showed to introduce more problem than benefits, due to the heating arising from the IR lamp. For investigating the temperature dependence on the IR intensity the measurements were repeated lowering the IR intensity as much as possible. This indeed changed the heating profile, and it was found that the final equilibrium temperature of the wafer sample would be approx. $43°C$, which is more than 50% heat reduction compared to maximal IR intensity. The temperature increased less than $2°C$ within the first 2 minutes after the IR lamp was activated, and it is believed that if low intensity is used, the time dependent temperature and %rHd variation, due to IR heating, can be neglected if the de-bonding part of the surface energy measurement does not exceed much more than 2 minutes.

After characterizing the chamber several crack tests were performed to investigate the surface energy behavior in different atmospheres. The measurements were static, performed by manually inserting a razor blade separating the bonded sample. After separation the blade position were kept constant, and the movement of the crack length were recorded on a video. The samples were all plasma activated room temperature bonded, using a ICP-RIE system for activation, with a power of 30w, a pressure of 280mTorr and activation times of either 30 or 150s. Due to the known changes in bond strength as a function of storage time, great care was taken that they were measured with same time delay, either 24 hours after bonding, 3 days or 6 days. Each bonded sample were cut in 6-8 pieces and several pieces were measured for each sample and on each piece two-three recordings were done. The humidity was divided into three categories, low humidity (0.5-5%rHd), medium humidity (15-23%rHd) and high humidity (over 30%rHd).

An example of measured samples in high humidity (59% $\pm$ 5%) and in low humidity($<$ 1% $\pm$ 5%) is shown in figure 3.14. As expected the crack length and thereby the surface energy were changing as a function of time and clearly differences for samples measured in different atmospheres were observed. For both measurements the energy is decreasing rapidly within the first 5-10 seconds, and afterwards only slowly decreasing. Long time measurements have been performed, and they indicate that for measurements in high humidity the energy keeps decreasing and no saturation value is reached whereas for the measurements in low humidity the surface energy seems to become stable after a while.

Martini et al.[43] have investigated the decrease in surface energy as a function of time, for bonded wafers annealed at 200-900 degrees, in air and at different ambient pressures. The strong observed decrease in effective surface energy is explained by considering what happens with the silanol bonds that are broken during the crack test after being in contact with the
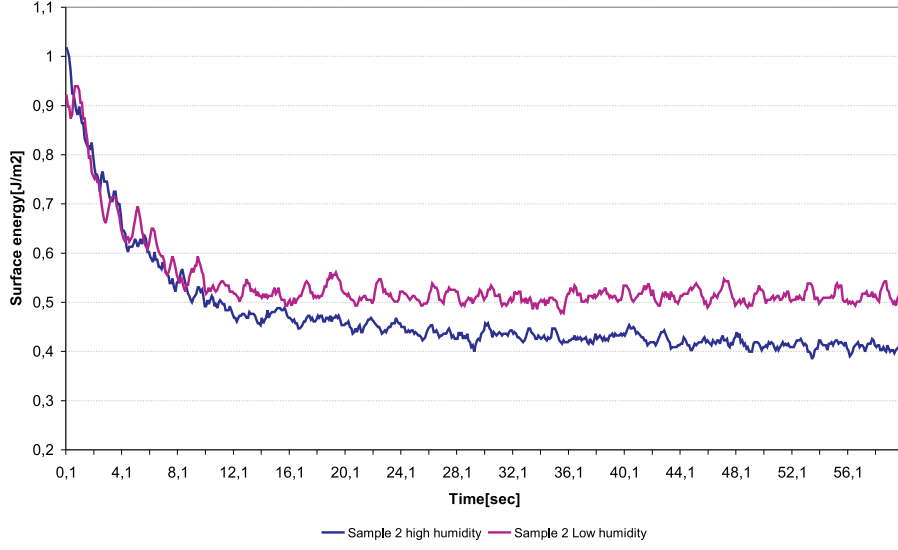
Figure 3.14: Surface energy as a function of time measured in low and high humidity.

water contaminated ambient.

The effective surface energy at t=0 after separation of the interface is defined as the energy difference [43]

$$\gamma = E_s(0) - E_I(0) \tag{3.13}$$

where $E_s(0)$ is the energy of the cracked surface at t=0 and $E_I(0)$ is the energy of the bonded interface. When separating the bonded wafers, the Si-O-Si bonds will mechanically crack and immediately after the opening there exist two surfaces with newly generated Si-O groups and dangling bonds, which are not covered with water. After insertion, water adsorption begins and decreases the energy of the Si-O groups and dangling silicon bonds. Due to this process the effective surface energy γ changes to [43]

$$\gamma = \gamma_0 + \Delta\gamma(t) = E_s(0) + \Delta E_s - E_I \tag{3.14}$$

where γ_0 is the surface energy at t=0 and ΔE_s is the energy difference between the water covered surface and the uncovered surface. The energy difference, $\Delta\gamma(t)$ is depending both on how many Si-O-Si bonds are present and afterwards have to be broken and on the adsorption process. The time dependence of this adsorption process for a constant concentration of water vapor is given by

$$-\frac{dc_{SiO}}{dt} = kc_{SiO} \tag{3.15}$$

where c_{SiO} is the concentration of Si-O groups and dangling bonds and k the rate constant. The solution to 3.15 is an exponential function, and by now assuming that the additional surface energy is proportional to the number of created Si-O groups per surface area, the time dependence of the surface energy can be written as:

$$\gamma(t) = (\gamma_0 - \gamma_\infty)e^{-kt} + \gamma_\infty \qquad (3.16)$$

where γ_0 is the surface energy at t=0, γ_∞ is the surface energy at t=∞ and k is the rate constant of the chemical reaction between water and the surface and stated to be in between $0.059\text{-}0.061 s^{-1}$ under ambient conditions and below 0.005 s^{-1} measuring at 10Pa pressure. The model by Martini et al. has been tested on our measurements and it was found that the model was in good agreement with the measurements when measuring in the lower humidity range. An example is depicted in figure 3.15.
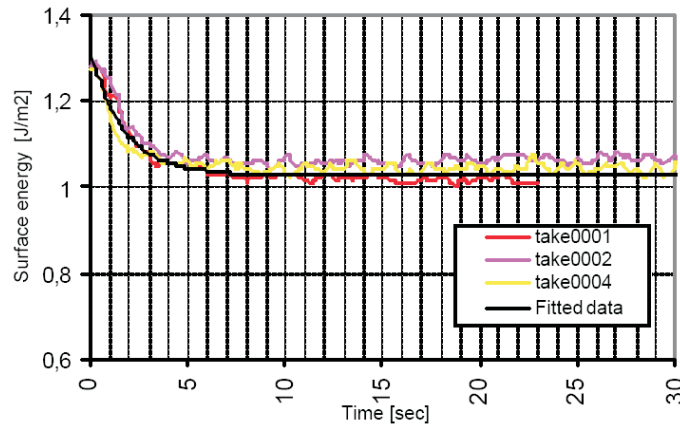
Figure 3.15: Martini's model fitted to the surface energy for sample measured in low humidity, day 3. $\gamma_0 = 1.32 J/m^2$, $\gamma_\infty = 1.03 J/m^2$ and $k = 0.6 s^{-1}$

The k value was found to be $0.6 s^{-1}$, which is higher than the typically stated values by Martini. For the results from the measurements performed in the higher humidity range it was not possible to obtain good fits. This is illustrated in the figures below where fits using three different k values are presented.

The sample is measured in a humidity of 35%, and as can be seen the fit is bad for all three different k values. The samples are all prepared and measured the same way , so the only difference for the two measurements is the ambient atmosphere. Depending on the humidity the decrease in surface energy behaves differently and as illustrated in figure 3.14, the surface energy measured in the low humidity range in general stabilizes after a while, whereas the surface energy measured at higher humidity continues decreasing indicating an extra long term effect.
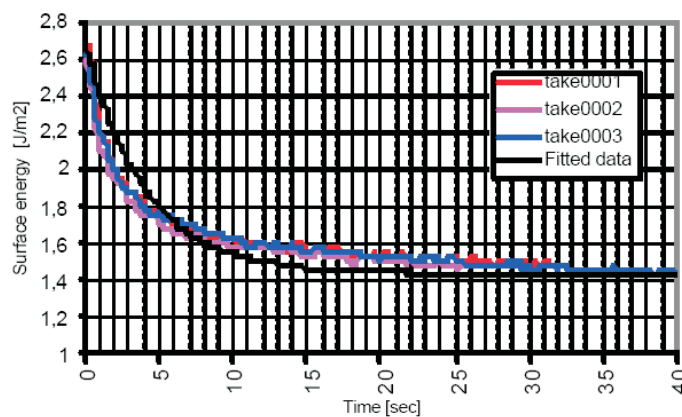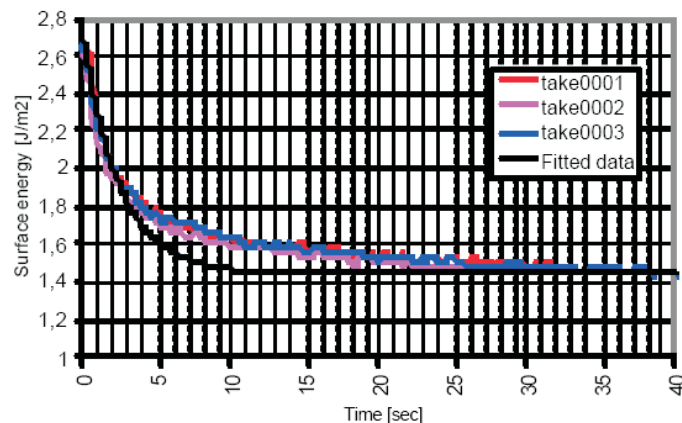
For solving the problems with the model for the samples in high humidity, expression 3.16 was extended. The extra effect is included by assuming that γ_∞ is time dependent and it is speculated that the long time decrease is due to the earlier mentioned effect of stress corrosion, where stressed siloxane bonds tend to be more reactive. The strained Si-O-Si bonds will be ruptured by an adsorbed water molecule and two hydroxyl groups are formed [45]. The new description is then assumed to consist of two contributions. One contribution to the surface energy is due to reactions on the newly generated surfaces , which immediately after separation react with the surrounding and are covered with water. The second contribution is due to stress corrosion and is a much slower process and is closely connected to the available surrounding water molecules and thereby the humidity . If it is assumed that the second process can be described with a similar expression as process one, with an expected lower reaction rate constant, the model is written

$$\gamma(t) = (\gamma_0 - \gamma_x(t))e^{-k_2 t} + \gamma_x(t) \qquad where \ \gamma_x(t) = (\gamma_{x1} - \gamma_{x2})e^{-k_1 t} + \gamma_{x2} \qquad (3.17)$$
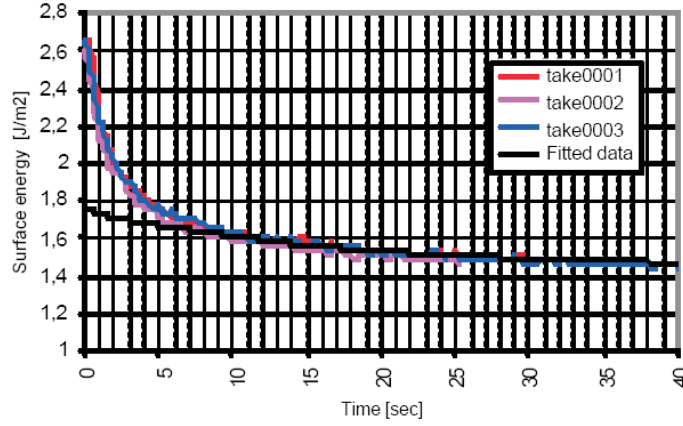
Figure 3.16: Martini's model fitted to the surface energy for sample measured in high humidity, day 3. $\gamma_0 = 2.7 J/m^2$, $\gamma_\infty = 1.44 J/m^2$ and k $= 0.4 s^{-1}$, $0.25 s^{-1}$ and $0.06 s^{-1}$ respectively.

The difference $\gamma_{x1} - \gamma_{x2}$ determines how strong the effect of the de-bonding is due to reactions with the surroundings and depends upon the humidity. k_1 is the rate constant related to process two and k_2 is related to process one. The assumed relationship between γ_{x1} and γ_{x2} and the humidity is calculated from the experimental results and shown in figure 3.17.
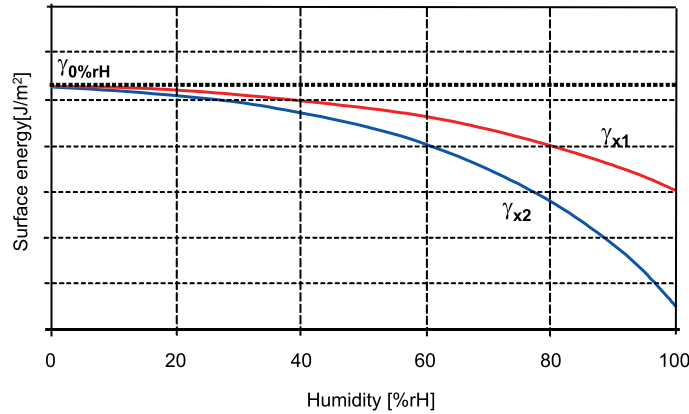
Figure 3.17: The assumed relationship between γ_{x1} and γ_{x2}

It should be noted that the displayed relationships are found from our measurements and can be different if other types than plasma activated bonded sample is considered. For 0% humidity, $\gamma_{x1} = \gamma_{x2}$ and expression 3.17 reduces to $\gamma(t) = (\gamma_0 - \gamma_{x2})e^{-k_2 t} + \gamma_{x2}$ and in this case the time depended surface energy will only depend on the reaction rate k_2. A plot of data fitted to the modified model is illustrated below.
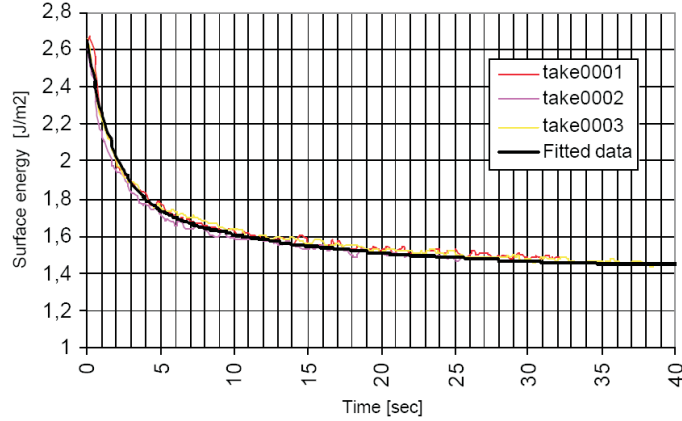
Figure 3.18: The modified model fitted to the surface energy for sample measured in high humidity, day 3. $\gamma_0 = 2.65 J/m^2$, $\gamma_{x1} = 1.82 J/m^2$, $\gamma_{x2} = 1.43 J/m^2$, $k_1 = 0.06 s^{-1}$ and $k_2 = 0.8 s^{-1}$

The model has been fitted to all measured surface energies and fits well for all of the results. Typically values of the fitting parameters listed from high to low humidity were found to be in the range of 0.03 to 0.08 for k_1, between 0.4 to 0.6 for k_2 and between 0.02 to 0.53 for the γ difference. The rate constants, (k_1, k_2) and γ_{x1} were found iterative, while γ_0 and γ_{x2} were extracted from the data. The reaction rate k_1 was obviously decreasing when measuring in the low range, which was to be expected since less water in the surroundings is present. The same tendency was observed for the k_2 values, even though it was not as clear, and for some of the fits it was almost constant and independent of the measurement surroundings. Further the k_1 values were always a factor of 10 smaller. The γ difference was as expected low, when measuring in low humidity.

3.2.4 Summary and conclusion

In conclusion we have been investigating our crack test set-up, and as expected a strong dependency on the delay time was observed. An expression describing the changes was found and it is speculated that an extra long term contribution from stress corrosion is affecting the observed increase in the crack length. The model was made from experiments on plasma activated bonded samples and is not necessary valid for other types of bonding. No differences were found between the sample made with exposure times of 30 and 150 s, but it could be interesting to test the other recipe parameters and see if any effects could be seen. In the model contributions from capillary forces have not been discussed, but it is believed that these can play some kind of role. Further it was observed during the investigations of the box that there is a possibility of sample heating, and thereby changes in the crack length, when exposed to the IR-light.

There are many other problems related to the crack test, than we have discussed in our test of the system and all of them are each contributing to make the test very uncertain. The

major problems are listed below

- **The Mazara model**
  As discussed earlier the use of Mazara's model yields an overestimation of the fracture toughness compared to more advanced models. For weakly bonded wafers an overestimation of 10% is found. Further, the models are based on cantilever beams while most measurements are performed on whole bonded wafer pairs. It is found that measurements on whole wafers will result in shorter crack lengths and thereby higher surface energies and errors between 10% and 25% in crack length are reported[72].

- **Stress corrosion**
  It is believed that strained bonds at crack tips are broken with molecules in the environments resulting in an increase in crack length. The effect is depending on the number of bonds that can be broken and the surrounding number of molecules.

- **Optical inspection of the crack length**
  The crack length is determined by optical inspection, and as discussed within the section of IR resolution voids with small gab heights can not be seen. This will affect the precision of the debond length. Several authors have used analytic expressions from simple beam theory to determine the actual crack length[72]. The optical inspection errors are found to be on the order of 10%.

- **Velocity**
  It is found that for the non static measurements where the blade is moved at a constant speed, the crack fracture toughness is changing as a function of blade velocity[9]. It was observed that in the low speed range the bond strength was increasing more as a function of velocity, whereas at high velocities it became stable. This has also been observed within our set-up where the crack length was inspected by video when stopping the blade and after some seconds moved again.

Despite all the problems related to the method it has been and is still used by many groups for evaluating on the strength of the bonding. Many of the problems have been investigated in details and by relative small improvements of the set-up more reliable measurements can be obtained.

The measurements should be automated for avoiding the operator dependence and raising the reproducibility of the measurements. The measurements should be performed on beams rather than whole wafers and the models used for calculating the bond strength should be more advanced than the model suggested by Mazara. In order to avoid or minimize contributions from stress corrosion the measurements should be performed within an controled atmosphere.

Many attempts have been made within the wafer bonding society to setup a standard way of performing the crack test, but without much success. The reasons for still using simple incomparable systems can be many, but it is believed that one main reason is that the system

and the corresponding calculations should be quick and easy to work with. Using different set-ups only allows for comparison between different types and prepared bonded samples in each individual laboratory and this makes it hard to compare results among work done by different groups. As a minimum it would be an improvement if published papers about bond strength measurements contained more details about the specific crack test set-up and the circumstances under which the measurements are performed. Further it has to be specified how many measurements are included making it possible to judge if the stated value is a good representative for the strength.

The bond strength measurements within this project have been performed using the earlier described set-up. They were typically made in air in the cleanroom unless other is specified. The read out of the crack length was done as quick as possible after blade insertion to minimize stress corrosion contributions, and in general for each bonded wafer pair measurements on several pieces have been made and for each piece two-three blade positions were inspected. In this way good statistics were observed. Due to the results from the detailed investigation of our set-up we were aware of the errors related to the measurements and the limitation of comparing measurements within the published papers. Great care was taken, that the same procedure was followed each time and many measurements were performed on each bonded wafer pair, and it is believed that the test optimizing work presented in the next chapter is indeed valid despite the problems related to the set-up.

3.2.5   Alternative methods for measuring the bond strength

Several alternative methods have been tested within the research of wafer bonding to overcome the difficulty using the crack test. A striking improvement would be an easily applicable method that does not rely on the ability of individuals of performing identical measurements.

Blister test

An alternative example of a method, which hinges on measurements of the surface energy is the blister test. In this test, two bonded wafers, where the bottom one has a hole reaching the interface are split by applying a hydrostatic oil pressure through the hole and thereby pushing the wafers apart[70]. If keeping the bottom wafer fixed and assuming no elasticity the critical pressure where debonding occurs can be measured by means of the surface energy given by[78]

$$\gamma = \frac{0.088 p_f^2 a^4}{E t_w^3} \tag{3.18}$$

where a being the radius of the hole, p_f the critical pressure for debonding, E Young's modulus of the top wafer and t_w the wafer thickness. The method can be used for testing both weak and strong bonds, but requires test structures made prior to the bonding and cannot be used for bond containing large unbonded areas. In advantage it does not require any gluing and both good repeatability and reproducibility is reported for the method[72].

However, model description and experimental verification are still not very well documented. Only very few papers have been published where this method has been used.

Tensile methods

Another method is the tensile strength measurements. A tensile test machine is used to measure the tensile strength of bonded wafers by pulling the wafers apart from opposite directions perpendicular to the interface plane of the wafers. The bonded sample cut into small pieces and typically glued with two-component glue to steels blocks with a smaller surface area. A force is applied to the blocks and calculations of the force applied per area is then assigned to the bond strength.

As the other methods tensile tests have their advantages and limitations. The quality of the adhesive used is of decisive relevance. Overcoming this limitation enables testing of bonded wafers with a very high strength, which would not be possible using the razor blade method. It is the second most used test for evaluating the strength of wafer bonding. However great care must be taken since large scatter in the measurements often is the result due to the brittleness of the typical materials used in wafer bonding. For making geometric independent measurements notches of known form must be introduced at the bond and an accurate stress analysis performed to obtain high accuracy.[72]

Chevron test method

The last method to be mentioned here is the chevron test, which is a further development of the tensile test. In this method, load is applied perpendicular to a specimen with a chevron shaped notch and fracture is initiated at the well defined tip of the chevron and propagates with increased load as a sharp crack. The method has been used with successful results by several groups and it can be used both for low and high strengths. The only drawback is the gluing, which is time consuming and may introduce small errors. It has not been used by so many groups so far, but it is believed to be one of the most promising methods for future evaluation.

Chapter 4

Process development and optimization

Wafer bonding is a sensitive process and the parameter space which influence the quality of the plasma bonded samples is huge. By changing the three variable parameters (power, pressure and activation time) in the activation process a series of measurements has been performed in order to investigate the changes in the bonding properties. Bond strength measurements have been used as a tool to determine the parameter combination resulting in the highest bond strength.

Other parameters, like e.g wafer type, wafer thickness, choice of cleaning process prior to activation and ect. can affect the measured bonding, but in order to narrow down the parameter space, they were kept constant. The wafers were, if possible, taken from the same batch or at least always chosen to be of same type, and the cleaning of the wafers before activation were always done in a RCA 1 solution. Further it can be discussed if a water rinse of the activated samples prior to the bonding affects the quality, and in this work both bonding with and without the water rinse step were possible. A few x-ray measurements have been made for investigating the influence, and the results indicate that the water definitely plays some kind of role. Other groups are in general using water to rinse the activated wafers and argue that this is necessary for obtaining good results. In spite of that and due to the already large parameter space we decided to continue the work always using a waterdip after the activation.

The bond strength measurements are used to determine the best recipe resulting in the strongest surface energies. This is an optimization process only concerning the strengths, and other variables such as processing time and cost are not included. Detailed understanding of the bonding mechanism is not necessary for performing the tests, but the response in bond strength when varying one parameter can be used in combination with other techniques to obtain general understanding of the mechanism.

4.1   Process optimization

The optimization included test series on both RIE and ICP-RIE plasma activation machines. Three parameters, power, pressure and activation time were varied in both systems in order to test their influence on the bond strength. In parallel oxide thickness measurements were done by ellipsometry to see how the thickness changed as a function of the different variables.

The wafer bonding is very sensitive to particles and all processes were carried out in the cleanroom facilities at DTU. As the test covered a long period, it was not possible to use wafers from only one batch, but the different wafers were all received from Okmetic[49] and were double side polished with the following specifications :

Diameter	100 ± 0.5 mm
Type	P/Boron/(100)
Thickness	$350 \pm 15 \ \mu m$
Resistivity	1-20 $\Omega \cdot$ cm

The double side polishing allows plasma activation on both sides. This turned out to be an advantage since otherwise void formation caused by bent wafers were observed. Assuming that wafers from the same box have identical bending properties, undesired voids were evaded by bonding wafer activated on opposite sides.

4.1.1   Cleaning

The cleaning procedure prior to activation differs from group to group depending on standard solutions available. Several groups [64, 69] have reported successful bonding using a RCA-1 clean, described below, and since a standard was necessary to eliminate further parameters in the process optimization all plasma activated samples in this project were cleaned using this solution.

RCA1	Ratio
DI-water	5
H_2O_2,31%	1
NH_4OH,25%	1

4.1.2   Activation

Two systems were used for activation, the RIE and ICP-RIE system. In both system only oxygen gas was used in the process, but other combinations are indeed possible. In both systems, activation time, power and pressure have been varied and for each parameter a test

series is performed in an appropriate interval. Following intervals were tested for the two
systems:

	RIE	ICP-RIE
RF Power/platen Power	10-200W	20-180W
Chamber Pressure	40-280mTorr	5-60mTorr
Activation time	15-240s	10-200s

Table 4.1: Test intervals for process optimization

4.1.3   Water rinse

There has been a big discussion among the groups working with wafer bonding technologies,
whether the wafers should be rinsed in water or another chemical solution after the activa-
tion. Some groups report strengthening of the bonds if they include a water dip subsequent
to the plasma treatment [77, 65, 73, 75], whereas others claim the opposite, reporting surface
energy measurements about a factor of two lower, when using a DI water rinse[75]. Many
process parameters possibly influence the quality of the bonding, and it is difficult to be
sure of the pure effect of rinsing the surfaces after activation. Pasquarillo et al.[51, 40, 50]
were using in situ bonding systems and reports successful bonding without water treatment.
Comparison of ex situ and in situ experiments indicate, that contaminant particles are rinsed
off by the DI-water treatment, which may not be necessary if handling the wafer in a vacuum
system. Further, Sanz-Velasco et al.[65] observed changes in surface roughness over time
for samples not dipped in water and they proposed that the DI water dip is important and
removes contaminations coming from the ICP-RIE chamber. AFM measurements performed
in our study disagree compared to what is observed by [65]. and in conclusion it was in
general found that both activated wafers that were rinsed in water and those not dipped in
water were changing surface properties as a function of time, attributed to the high reactive
surfaces reacting with the surroundings. The storing of the wafers after activation were found
to be important and also the time before performing the AFM measurements affected the
results.

In order to limit the already huge parameter space affecting the bonding, it was decided
always to use a water rinse for tree minutes followed by spin drying the wafers.

4.1.4   spin drying

After the DI Water dip, the wafers are spin-dried. Without properly drying, wafers would
float on each other resulting in an unbonded sample, and it is therefore very important to
assure that wafers are spin dried long enough and at least until water is no longer visible as
colored rings spreading from the center. Experience with the spin dryer reflected a remarkable
difference between activated wafers from RIE and ICP-RIE chambers. Using the standard
spin time adapted for RIE activated wafers caused problems bonding ICP-RIE activated

wafers. The ICP-RIE surface is far more hydrophilic and consequently longer spin time for obtaining spontaneously bonding was needed. The extent of hydrophilic or -phobic surfaces was determined using a contact angle measurement equipment available in the cleanroom[56].

It is not clear which role the water dip actually plays, but it is speculated that as long as water is observed at the interface, the bond strength will somehow be limited by the strength of hydrogen bonds [40]. Amirfeiz and Sanz-Velasco et al. suggested that water present in the samples is diffusing through porous channels within the plasma generated oxide [65, 3]. This idea was investigated in details by Egebjerg[21] performing TOF-SIMS experiments with D_2O treated samples as well as TEM imaging and SAM experiments. In conclusion, the existence of pores was disproved.

4.2   Bond strength tests

The bond strength tests were used for optimization of the plasma recipes in the two chambers. The idea was to find the parameter combination resulting in the highest bond strength and in parallel follow, how the thickness on the generated oxide is affected when changing the process parameters. Several of the tested samples were afterwards characterized by x-ray reflectivity for obtaining changes on microscopic scale as a function of the different systems and recipe parameters. These measurements are described in chapter 5.

Before optimization a start recipe was needed. For the RIE system we used a recipe earlier described by [65, 64, 75] and for the ICP-RIE a recipe developed by [76, 64].

	RIE	ICP-RIE
RF Power/platen Power	200W	15W
Chamber Pressure	300mTorr	40mTorr
Activation time	60s	30s

Table 4.2: start recipes

4.2.1   RIE-system

Power variations

First parameter to test was power variations of the system. For the RIE system, the power was first varied using relatively broad intervals, finding the region which results in the highes bond strength (named standard in the figures). Setting the power to the best value in this region, the other parameters were tuned. Now using the optimized pressure and time values the power variation was then repeated(named optimized in the figures). The results are depicted in figure 4.1 below.
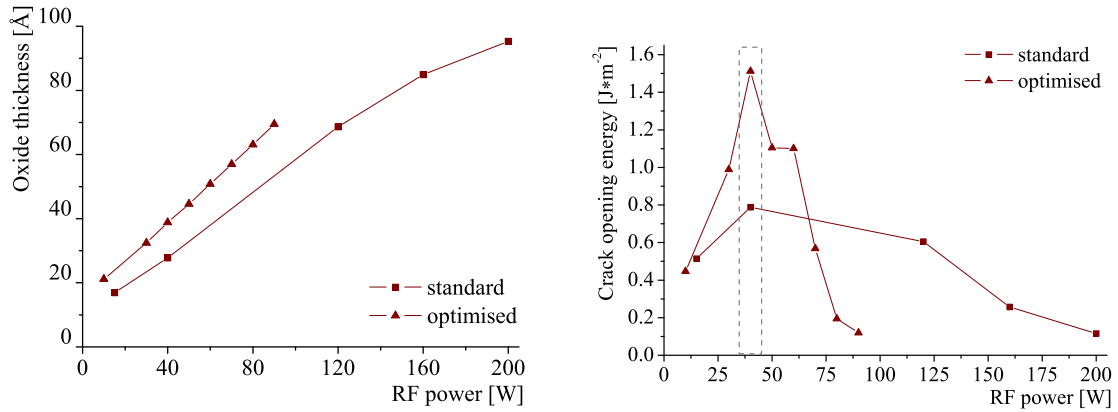
Figure 4.1: Left: Oxide thickness measured by ellipsometry plotted as a function of RIE power variation. The oxide thickness increased linearly with power. Test results using the standard recipe with 60s activation time and 300mTorr chamber pressure as well as the optimized recipe (160s activation time and 280mTorr chamber pressure) are depicted. Right: Crack opening energies as a function of RIE power variation are plotted for the standard recipe and the optimized recipe. After optimization, the interesting interval is narrow and peaks around 40W.

Variations in RF power showed a higher bond strength value using low powers. The highest value was obtained at 40W, which is marked with a dotted line in the figure. The tendency was the same for both tests, using either the standard or the optimized values for the other two parameters. For the optimized test, the bond strength was very high at exact 40W, whereas at the interval around 40W remarkably lower values were observed. It should also be remarked that the bond strength values were found to be very sensitive to changes in the parameter space, since after the optimization, twice as high bond strength is observed at 40W.

In parallel the oxide thickness as a function of the power variation was measured. Again both values for the standard and optimized process are plotted, and as can be seen in the figure, there was a linear relation between the RF power values and the oxide thickness in the lower RF region. Using linear regression the best fit for the optimized series was found as [21]

$$y = A + B{\cdot}x, \qquad \text{where} \quad \begin{aligned} A &= \quad 14.6 \pm 0.3\text{Å} \\ B &= \quad 0.605 \pm 0.005\text{Å}{\cdot}\text{W}^{-1} \end{aligned}$$

The thickness for the optimized series is in general 10Å thicker, and it is clear that increasing the power of the system also increases the generated oxide thickness. It is not clear, if there is a saturation thickness value. No saturation level was observed as the limit of the RIE was reached when trying to activate wafers at 300W. The thickness at 40W is 40Å.

Pressure variations

Next to be considered is the pressure dependence. The pressure was varied from 40- 280 mTorr, and the corresponding thickness variations are depicted in figure 4.2
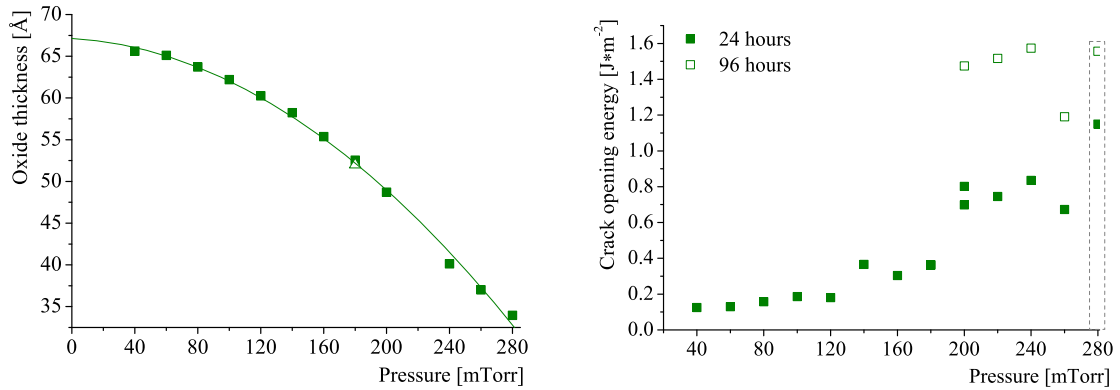
Figure 4.2: Left: Influence of pressure variation on the thickness of the generated oxide layer. A second order polynomial fit matched the relationship between these two parameters. The oxide thickness was decreased when the RF power was increased. Two samples with identical process parameters were produced in order to test reproducibility. They were almost overlapping and had a difference of only 0.6Å. Right: Investigation of the influence of pressure variation on crack opening energy. Values were measured 24 hours after bonding and 96 hours after bonding for some of the samples. Samples with identical process parameters were produced in order to test reproducibility. The bond strength of the samples increased with pressure, and a remarkably stronger bond was obtained during storage (24 compared to 96 hours).[21]

It was observed, that the thickness decreases for high pressure values, and the best fit is now found using polynomial regression[21]

$$y = A + B_1 \cdot x + B_2 \cdot x^2, \qquad \text{where} \quad \begin{aligned} A \;\; &= 65.9 \pm 0.4 \text{Å} \\ B_1 \;\; &= 0.013 \pm 0.007 \text{Å} \cdot \text{mTorr}^{-1} \\ B_2 \;\; &= \text{-}0.00049 \pm 0.00003 \text{Å} \cdot \text{mTorr}^{-2} \end{aligned}$$

To test the reproducibility two identical samples with the same recipe parameters were measured. The result can be seen as the white triangle at 170mTorr in the figure. The results were very similar both regarding thickness and surface energy indicating that reproducibility is possible.

In the right figure the filled squares are the crack opening energy as a function of pressure and it was found to increase with increasing pressure. Very low energies were found using low pressure values and the result is very convenient, that the optimal pressure value should indeed be in the high pressure region. The best value is again marked with a dotted line and a value of 280mTorr was chosen for further optimization.

As the bond strength energies found in this test were remarkably lower than what was measured in the previous tests, effort was put on investigations of the bond strength as a function of time. Wafers were prepared using the exact same process parameter, but instead of measuring the bond strength immediately after the bonding, the wafers were now stored for three days in the cleanroom and then measured. The results are shown as the unfilled squares in the figure and it was clear that the bond strength was raised and approximately doubled.

This is in good agreement with experience with other types of bonding[70] and can explain the observed difference within the two tests.

Exposure time variations

Last parameter to work with was the activation time. For these tests, the oxide thickness were found to reach a saturation level at 40 Å, using a power value of 40W and a pressure of 280mTorr. This observation is in good agreement with results from Pasquariello et al.[51] in which high initial grow rates and a saturation level of 57Å after 200s are reported. The difference in thickness is attributed to the use of different power values.
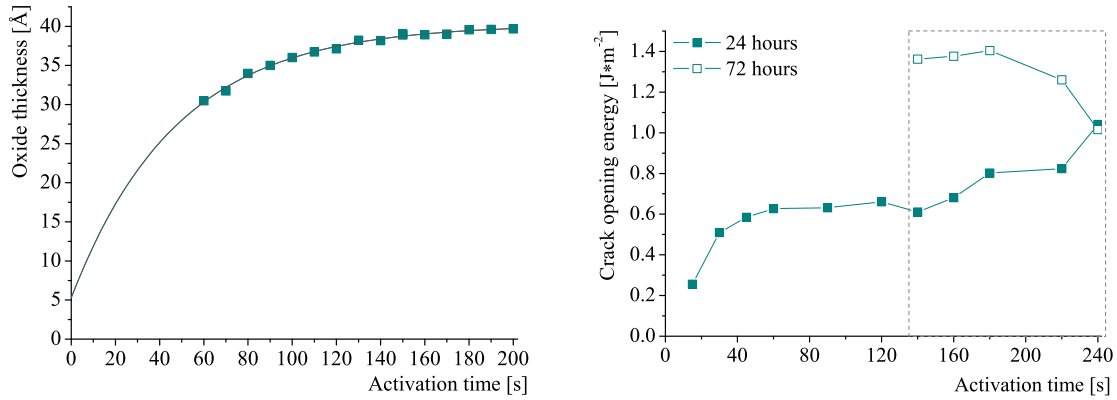
Figure 4.3: Left: Oxide thickness variations due to changes in the exposure time. The oxide thickness reached saturation at t=200s and 40Å. Right: crack opening energy variations due to changes in the exposure time. High bond strength values are obtained for long activation times and after three days storage this value was doubled for several test samples.

The oxide thickness is plotted versus activation time in figure 4.3, where the line shows the best fit[21]:

$$y = A_1 - A_2 \cdot \exp(-kx), \qquad \text{where} \quad \begin{aligned} A_1 &= 40.25 \pm 0.21 \text{Å} \\ A_2 &= 34.96 \pm 2.73 \text{Å} \\ k &= 0.021 \pm 0.001 \text{s}^{-1} \end{aligned}$$

The exposure time dependence in the crack energy measurements are not as convincing as in the earlier test, but a small tendency can be found, that the energy is higher for longer exposure times. The upper time region is marked on the figure and to conclude from the test, activation times within this interval are resulting in the highest bond strength. An activation time of 180s was chosen to give the best results.

4.2.2   ICP-RIE system

Although the plasma is coupled differently in this system, the plasma was expected to behave similar when the three parameters were varied. The ICP-RIE has a faster etch rate at lower

pressures and the test series were started using a low power and varying exposure time and pressure.

Exposure time variations

The exposure time was tested in the time interval from 10 - 200 seconds. The other parameters were kept at 15W RF platen power and 40mTorr chamber pressure. The results are depicted in figure 4.4
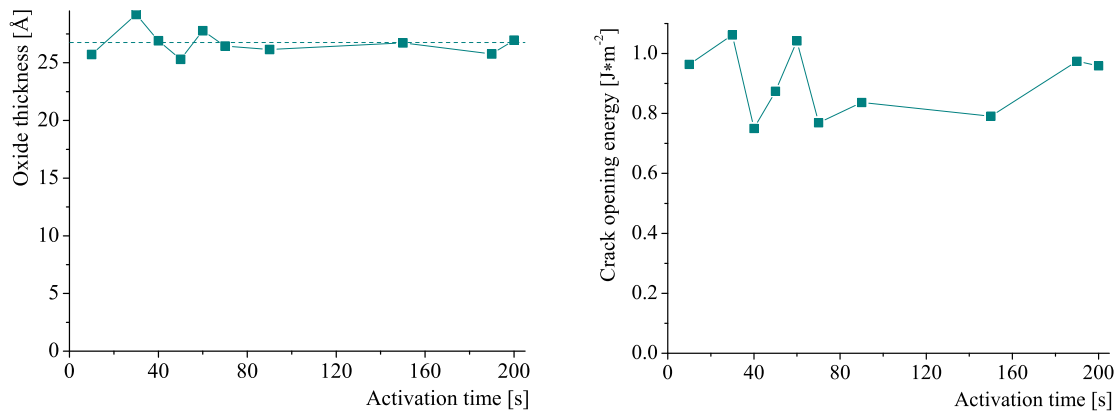
Figure 4.4: Left: The oxide thickness did not have any correlation to activation time in the ICP-RIE samples tested here. Instead a tendency to fluctuate around the mean value of 26.7 Å was observed. The standard deviation was 1.1 Å with an error of 0.4Å. Right: Bond strength plotted vs. variation of ICP-RIE activation time.

As can be seen in the figure no correlation between oxide thickness and activation time was found. Rather it seems to fluctuate around 26.7Å, which is clearly different compared to the observations from the RIE system. The mean value is marked with a line and the standard derivation is found to be 1.1Å[21]. The fluctuations can either be explained by uncertainty in the elliposometre thickness measurements or by a varying quality of the generated oxide layer. In general the ellipsometer measurements have an uncertainty of a couple of angstrom.

The results of the crack test measurements were also very fluctuating and due to the rather random distribution it was not possible to conclude that values within a special area were better than others. For the further tests a value of 30 s was used. A comparison of the two figures showed that the variations are comparable, and it is speculated that the results probably are to be interpreted as a measure of reproducibility rather than uncertainties in ellipsometry measurements[21].

Power variations

The power was varied in the range from 20W - 180W, but neither in these tests, significant changes in layer thickness were observed. There was a slight tendency that the layer is thicker for higher powers.
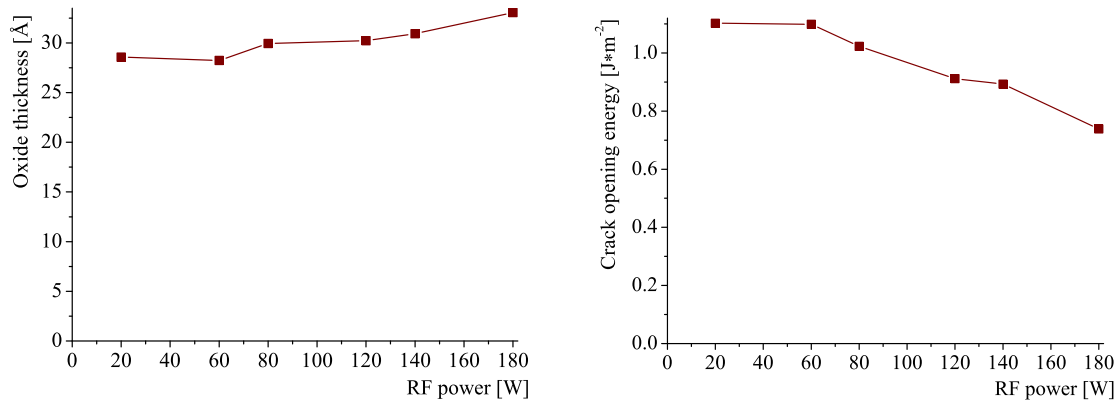
Figure 4.5: Left: Oxide thickness variations due to changes in the activation time. The oxide thickness slightly increased with RF power. Right: Crack opening energy variations due to changes in the activation time. The highest bond strength values were obtained for low values of RF power.

For the crack test the same tendency as observed for RIE plasma oxide appeared: low power settings caused the highest crack opening energy. The crack opening values ranged from 0.7 - 1.1 J· m^{-2} in the same RF-interval where RIE values are ranged from 0.1 - 1.5 J · m^{-2} and a value of 20W platen power was chosen to give the best result.

Pressure variations

The last to test is the pressure dependence. The pressure limit of ICP-RIE was reached at 60mTorr using settings 20W and 30s, whereas the RIE was able to operate at 200-300mTorr. This is in agreement with the basic features of both types of activation machines presented.

For the thickness measurements again no remarkable changes were observed, except a small tendency that the thickness is approximately 5Å thicker for the high pressure values. The crack test results were very fluctuating, with no indication that a special range is preferable. In general the optimization procedure of ICP-RIE treatment did not show any significant trends, and it was therefore decided to investigate recipes representing a broad range of the activation parameters for use in the X-ray measurements. The purpose of this was to investigate whether any differences were possible to detect in reflectivity curves or their corresponding density profiles.
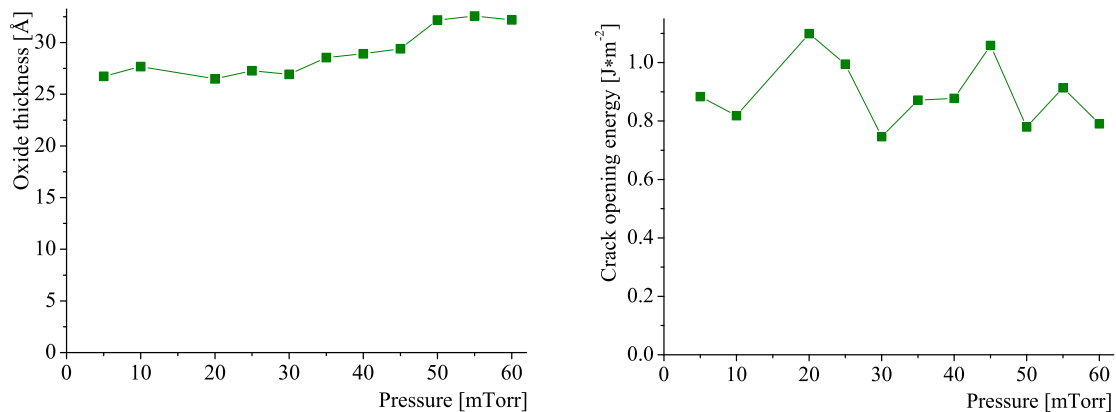
Figure 4.6: Left: The oxide thickness increased with the ICP-RIE chamber pressure, but there was no clear correlation as observed in the RIE chamber. Right: Crack opening energy variations due to changes in chamber pressure. The test did not show any correlation between these two parameters. All values seemed to be randomly distributed.

4.2.3   Test results discussion

It was clear from the tests, that the RIE system is far more sensitive regarding oxide thickness and surface energy measurements when changing recipe parameters, than the ICP-RIE system. Thickness results from the ICP-RIE are very alike and the surface energies are fluctuating, whereas no optimized parameters can be found.

The coherence between oxide thickness and RF power, pressure and activation time was speculated to be closely related to the density as well as roughness of the oxide layer. The bond quality declines with increasing surface roughness and if changing the parameters affects the density and roughness, it will affect the ability to obtain good bonding. However, this relationship has not been quantified during the optimization process.

Due to the large observed fluctuations in some of the measurements it was decided to test the reliability both for the oxide thickness measurements and the surface energy measurements further. Nine bonded samples were prepared with identical process parameters and for either bonded sample, two wafer pieces were tested. The results are shown in figure 4.7
As can be seen in the figure some fluctuations were observed, but in general the repeatability is good. Each column in the right histogram represents the mean value of crack opening energy resulting from six to ten pictures of each wafer piece. The mean value is 1.019 ± 0.095 J·m^{-2}. The deviation in the crack opening length was introduced either during sample preparation in the cleanroom environment or by differences in the bond strength measurement procedure. However, it was not possible to distinguish between these contributions beyond a qualitative evaluation by IR or eventually SAM pictures. The observed crack opening lengths were compared with IR-pictures of the samples for investigating if any correlation between voids at the interface and surface energies could be found, but no such could be proven.
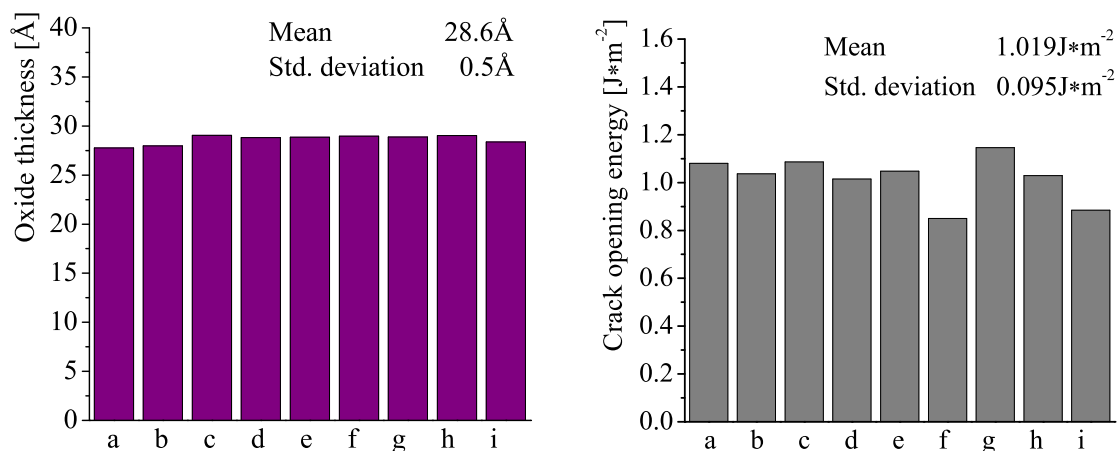
Figure 4.7: Bond strength measurements immediately after bonding on nine samples prepared with identical process parameters. The oxide thicknesses measured by ellipsometry is depicted to the left. To the right, bond strength measurements are presented. Each column represents the mean value of six to nine pictures of two test pieces from either bonded sample[21].

The oxide thicknesses of the identical samples were also measured and are depicted by the purple columns to the left in figure 4.7 with a mean value of 28.6 ± 0.5Å. The deviations may be from small variations in any recipe parameter, which has directly influence on the oxide thickness during plasma activation as well as uncertainties from the ellipsometer thickness measurements. Considering the parameter space that influence the oxide formed by plasma activation, a thickness variation of 1.7% is considered rather low, and a scattering of 9.3% around the mean crack opening energy is also acceptable for application in the optimization procedure.

The structure of the oxide, which forms when ions are bombarding the surface during the oxygen plasma treatment, determines the final character of the surface. The chamber pressure is closely related to the directionality of the ions and a low pressure is synonymous with a high directionality of the ions. Pressure also influences the ratio between ions and neutrals and thereby the amount of ions which hits the surface.

Changing the RF power directly changes the RF-voltage applied to the system and thereby the energy of the ions striking the surface. An increased energy causes an increased oxidation rate, but this is not necessary of advantage since high ion energies may cause surface damage. The exact relation between the energy and flux of particles pelting the surface and the actual oxidation rate is not well known. Further, it is rather difficult to survey this relationship because no equilibrium is attained in the plasma chamber and the kinetics of many contributing reactions are unknown.

It is speculated that a high pressure can cause ions to repel from the surface leaving holes in the structure within the upper layer of atoms. Further the ion bombardment, which takes

place in the plasma chamber, changes the chemical state of the oxide and consequently increases the reactivity of the surfaces. The conditions under which an increased surface energy is achieved is probably balanced between the increased reactivity and the degradation of the surface, when the ions are too energetic at high self-bias voltages.

4.2.4   Summary

In this work the bond strength was used as optimization value for developing a recipe with appropriate parameters resulting in the good bonds. A low RF-power value resulted obviously in the highest bond strength for both the RIE as well as the ICP-RIE tests, and in the RIE tests, the highest bond strength values appeared using a relative high pressure, while for ICP-RIE tests, there was no striking tendencies concerning the pressure. For the activation time no tendency was observed for the ICP-RIE and for the RIE samples it seems that using longer activation times gave the best results.

As already discussed in the previous chapter about the crack test set-up, it was observed that a standard for recording IR pictures is necessary in order to minimize the errors, and by using same procedure a good repeatability was observed.

Successful recipes were developed resulting in a high yield of samples with few and very small voids, and for the X-ray experiments, a selection of the recipes that resulted in high measurable bond strengths was used for further investigations.

Chapter 5

X-ray investigations of the interface

X-ray reflectivity measurements were performed to investigate the interface between the two plasma assisted bonded wafers. Density profiles, fitted to the reflectivity curves, were found in order to obtain more detailed information of the bonding process, and to attribute the physics and chemistry behind the plasma bonding.

The experiments that motivated the x-ray studies were first carried out by Buttard et al. [14]. They were investigating twist bonded Si/Si and Si/SiO$_2$ interfaces using x-ray reflectivity with transmission geometry. Instead of measuring on whole bonded wafers, the bonded wafer pair were cleaved in narrow stripes. The x-ray beam was directed by transmission though the cut edges, using a grazing incidence angle relative to the bonded interface. Due to absorption relatively high photon energies are needed and the width of the stripes have to be relatively narrow(100-500μm).

Measuring a buried interface is not straight forward and if measuring by conventional x-ray reflectivity, the signal coming from the interface will be mixed with reflections from the outer surfaces and moreover intensity are lost due to absorbtion effects. These problems can be avoided in the transmission geometry, whereas the set-up is very suited for measuring buried interfaces.

Rieutord et al. [62] were also using the geometry, and in their paper they have investigated the bonding interface of two silicon wafers as a function of in situ annealing from zero to above 1000 degrees. The reflectivity data were modelled quantitative using a kinematic approach, where the reflectivity was the fourier transformation of the index gradient profile. The electron density profile was described by a box model including roughness and a dip at the interface which was represented by a "Gaussian well" with width σ and depth $\Delta\rho_{dip}$. In their experiments they successfully followed the changes of the gab at the bonding interface and the changes in the oxide layers as a function of temperature, and their results are in good agreement with results from other techniques used for investigating the bonding.

Model fitting of the reflectivity data is a complicated and time consuming process. Modelling the data is often done by describing the searched profile as a multilayered stack, where the parameters are adjusted to minimize the difference between the calculated and observed

reflectivity. Extracting a density profile in this way is of the trial and error type, and it is indirect, so the results may depend on the used description or on the input values of the parameters.

Bataillou et al. [5] were presenting a method for analyzing data, by direct fourier inversion of interfacial reflectivity data by using the Patterson function. This technique provides directly the interfacial profile, it does not necessarily provide the best accuracy of the profile parameters. Nevertheless it is useful, since it reveals a rough profile not relying on a prior knowledge of the profile shape, and the resulting profile can later be used as input for a refinement procedure making the analysis easier.

For our data analysis an analyze program has been made. In the program, an input profile and several restrictions on the fitting procedure was necessary to avoid physical unrealistic solutions. Using our program, it was possible to find good matching density profiles, which were fitting the densities in detail.

Several other papers are published using the geometry for investigating silicon bonded interfaces [24, 15, 57], and also other bonded materials like SiN, InP and GaAs have been investigated using the method [31, 32].

5.1   X-ray reflectivity from buried interfaces

The experiments in this project were carried out at the Hamburger Synchrotronstrahlungslabor (HASYLAB) with the wiggler beamline BW2 [11, 30]. A range of different RIE and ICP-RIE processed samples were investigated. Both specular reflectivity of single wafers treated with oxygen plasma and specular reflectivity from the interface in transmission geometry were done. The results from single wafers are much easier to analyze compared to the data from the buried interface, and the results were used as input model parameters in the analyze of the reflectivity from the bonded interface.

The experimental set-up used is described in the first section of this chapter. Next model simulations of the system are presented, followed by a selection of collected data. The results of the data fitting are then discussed, and at the end of the chapter is a general discussion of the results and a summary of the conclusions.

5.1.1   X-ray reflectivity measurements

The samples investigated in this study, consist of two silicon wafers surrounding a silicon oxide interface-layer. The samples prepared for data collection are cut in narrow stripes. They are referred to as 'strips' and are illustrated in figure 5.1.

Samples for data collection were prepared according to the cleanroom procedures described in the previous chapter. The process parameters of RIE and ICP-RIE methods were varied in order to investigate the relationship between activation methods, reflectivity curve

A) strip sample for X-ray measurements

~140μm

B) bonded sample, 4" diameter
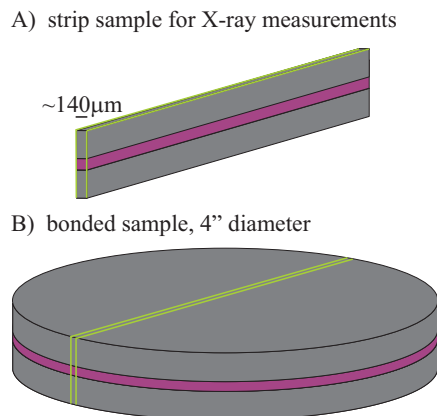
Figure 5.1: Illustration of a Si-SiO$_2$-Si strip sample used for data collection at BW2, HASYLAB.

and density profile of the interfacial oxide. To inspect the quality of the samples, IR pictures were used. It was always possible to find an appropriate position, where wafers were perfectly bonded as long as the main part of the sample was bonded. In the set-up, the samples could easily be translated parallel to the interface plane, and thus measurements could be carried out at a different spot, testing the reproducibility within each sample. All samples were cut out within 12 hours before departure to BW2. Half of them were bonded 7 days before, and half of them stored for less than 24 hours. As mentioned earlier the bond strength is increasing with storage time, and it should be detectable in the reflectivity curves.

5.1.2 Experimential set-up

In the x-ray experiment, a well collimated beam is transmitted through a thin strip of a plasma-bonded wafer and reflected by the interfaces. A translation scan perpendicular to the interface plane with three peaks is depicted in figure 5.2[21]. In the figure three peaks can be seen, which are reflectivity from the top wafer, the interface and from the bottom.
A closeup sketch of the interfacial reflection is illustrated in figure 5.3. The x-ray measurements were performed with a monochromatic beam of 10keV or 20keV and at this energies the attenuation lengths are 134μm and 1038μm respectively [21]. The sample widths were consequently aimed to these sizes.
The vertical size of the incoming beam hitting the sample is approximately 30μm. Each wafer is 350μm thick, and the interfacial oxide layer is in the range of 60-250Å. With a distance of approximately 350μm between the internal and the external interfaces, the sample can be aligned in a low-angle geometry, where the beam never hits the external interfaces of air and silicon. Reflections that cause intensity are therefore primarily due to changes in the density of the materials in the interface zones, and strong contributions from the Si-air interface are excluded[21]. Further the direction of the incident x-ray beam is almost normal to the sample edge, and therefore refraction effects are reasonable to ignore.

In figure 5.4, pictures of sample set-up and the used diffractometer at BW2 at HASYLAB
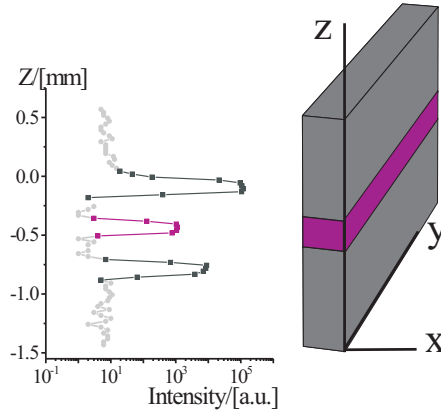
Figure 5.2: Coordinate system of the strip samples used in the X-ray reflectivity set-up[21].
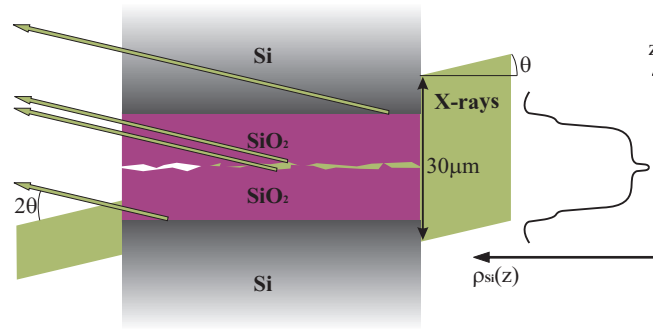
Figure 5.3: To the left, a sketch of the interfacial reflection from a plasma-bonded sample in the set-up at BW2, HASYLAB. Right: An example of a possible density profile.[21]

in Hamburg are shown. The strip samples were glued at a bend wire, see figure 5.4. This caused some problems in the beginning due to stress and moving samples, but by appropriate choice of glue these problems were solved.

5.2 Model simulations of the systems

In order to obtain better understanding of the reflectivity data, model simulations for several different simple systems were considered. The simulations were made by Egebjerg et al. using the program Parratt32, which is a freeware programme well suited for this purpose [71]. Input values for Parratt32 at 10keV were calculated with the MatLab programme, Reflectivity Database, for a range of densities [48].

First we start by considering a single wafer covered with a thin single layer of oxide. This system corresponds to the activated wafers prior to the bonding. Standard density values of Si and SiO_2 are $2.33 \text{g} \cdot \text{cm}^{-3}$ and $2.196 \text{g} \cdot \text{cm}^{-3}$ respectively and they are used, unless other densities are specified.
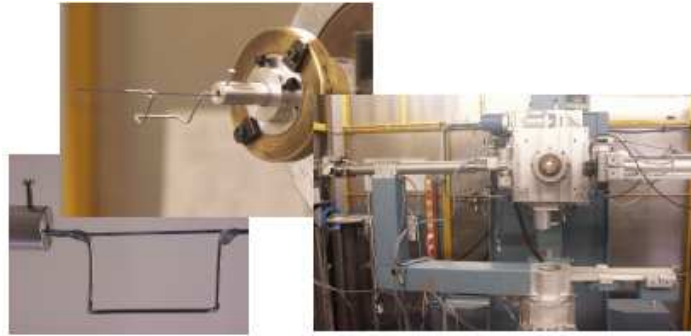
Figure 5.4: Sample setup and instrument in the beam hut at BW2, HASYLAB.
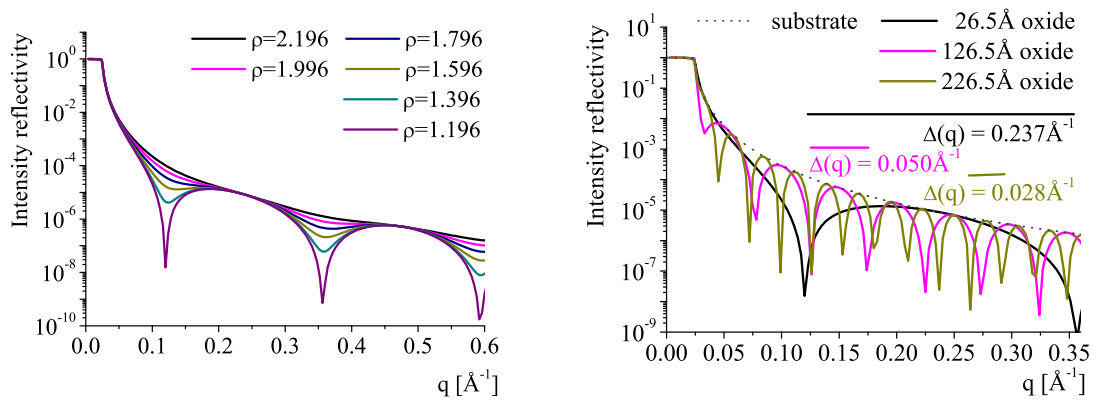
Figure 5.5: Model simulations of a single wafer covered with oxides of different densities(left) and different thicknesses(right).

The left figure illustrates how the resulting reflectivity curves are changing in shape, when assuming different densities of a 26.5Å oxide layer on a silicon wafer. As can be seen, at large difference between oxide and silicon densities results in more pronounced dips in the reflectivity curve. In the figure on the right the reflectivity curves from oxide layers of different thickness with constant density are depicted. The period is related to the layer thickness and is now different for the considered layers, but the intensity level was the same independent of the oxide thickness.

The effect on the reflectivity curves when varying the roughness is illustrated in figure 5.6[21]. Different roughness values of the air-Si and Si-SiO$_2$ interfaces are chosen and the resulting intensity curves plotted. The illustrated curves are all for a 26.5Å oxide layer covering a silicon wafer. Standard density value of silicon was used, but in order to have clear amplitudes, 1.196g·cm^{-3} was used for the oxide layer. The model intensities reached values, which were far below what was observed in the experimental measured data, whereas roughness values higher than 5Å were not expected in the bonded samples. This is in agreement what
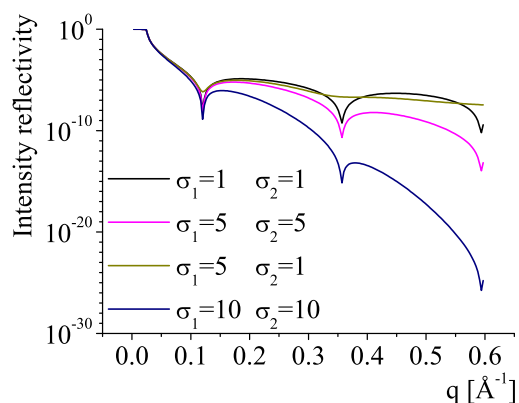
Figure 5.6: Illustration of roughness variations of an oxide layer that covers a single Si wafer. The oxide layer measured 26.5Å[21]

to expect for standard polished wafers, where the typically roughness is stated to be below 5Å.

Further, it was investigated what happens when a single wafer is covered by an oxide layer, consisting of two regions of different densities. This was interesting, since it was speculated that the oxide layer created during activation would consist of a thin less dense 'linking' layer of a few angstrom close to the silicon surface, and on top on that, a thicker more dense layer. Second also information about reflectivity from two regions of equal thickness was of interest since this corresponds to the situation of bonding two activated surfaces.

When regions of different densities are combined in a layer, a reflectivity curve with multiple peaks appears. It was found that the valleys between peak pairs are deeper if the difference in the thickness is large, but the dip between peaks in a pair is obviously amplified, when the thicknesses approaches each other[21]. It was clear that, when the densities of neighboring regions did not vary sufficient, or the thickness of a region was negligible compared to the total thickness, the reflectivity curve simply approached the situation of a simple box with a period of one peak[21].

Modelling the bonded system

The samples to be investigated consist of two silicon wafers with an in between unknown number of oxide layers with unknown densities.

The most simple model to consider corresponds to the ideal case, where two oxide layers are equal in thickness, completely homogeneous and not separated by a bonding interface. For this system the density profile consists of three boxes flattened out by adding interfacial roughness. The situation is illustrated in figure 5.7[21].

The oxide thickness was assumed to be 2 x 27.1Å, which corresponds to a thickness value
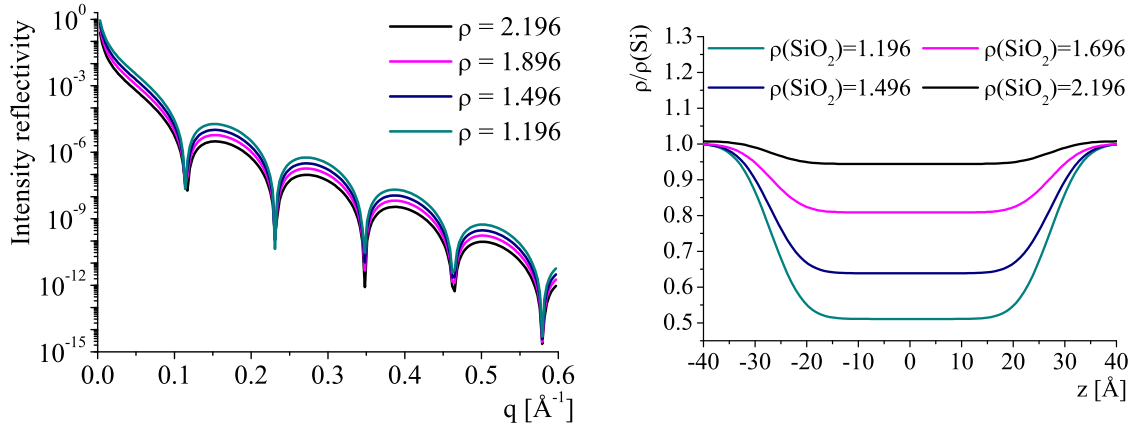
Figure 5.7: Reflectivity model simulation for a simple three box bonded system with different oxide density values.

from one of the samples to be investigated. In the figure reflectivity curves for different oxide densities are plotted. When changing the oxide density no changes regarding periods and amplitudes are observed, but it was clear that the overall intensity increases with $\Delta\rho$, and that the changes are independent of q. This is different from the case of a single wafer covered with oxide film illustrated in figure 5.5, where the maximum intensity of the peaks matched, but the oscillations were damped.

For the real samples where wafers that are covered with SiO_2 adhere, a new interface at the center of the SiO_2 layer is created, and it is very likely that the density of the oxide in the middle of the sample differs from the oxide density in general. Surfaces are never perfectly terminated and bond lengths, angles and coordination number of Si and O may differ from the plasma activated oxide layer in order to comply with the most stable conformation. In figure 5.8 the situation for a symmetric layer model with an interface range that differs in density is illustrated.

The labels in the figure refer to the thickness, t and density, ρ of the layer used in the models. In the two figures, four simple profiles and corresponding reflectivity curves are depicted. Very different oscillation patterns result from small variations in thickness and density of the central oxide layer. The curves in magenta and blue swap succession of small and large peaks as the density of the oxide layer in the middle is increased and decreased compared to the surrounding oxide layers, respectively.

Comparing the blue and the black curve, it can be seen that increasing the densities in all three regions with the same amount, while shrinking the thickness of middle layer from 5 to 1Å, does not change the reflectivity curve remarkably, even though the density profiles look very different. The effect of shrinking the middle from 15 to 5 Å keeping identical densities can be seen by comparing the blue and green curve. The differences in these reflectivity curves are larger, which can be attributed to the larger thickness difference for all three layers.

The models are assumed to be symmetric. This is also in general to be expected from the real
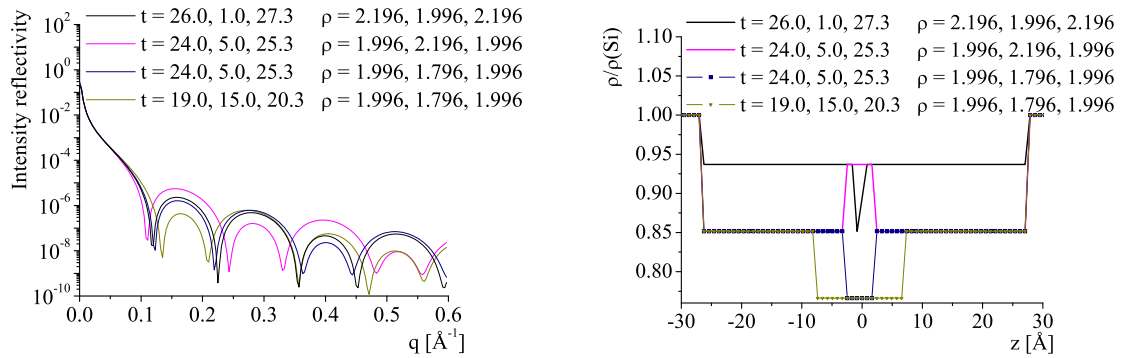
Figure 5.8: Reflectivity models for bonded systems with different interfacial thickness and density layer.

samples, but even though plasma activation of the two wafers was carried out with exactly the same process parameters, small differences were detected, and even small variations in the oxide density and thickness can cause the corresponding reflectivity curve to assume very distinct shapes.

5.3 Reflectivity curves from bonded samples

The samples are symmetric and can be measured for both negative and positive incidence angles. This has been done for several samples and as expected symmetric reflectivity curves were found, but for simplicity only those with positive incidences will be presented here. All results were normalized and background subtracted before the data were analyzed. Details about these produces can be found in the thesis by Egebjerg [21].

Many different samples were prepared during this project, but not all of them were successfully measured by x-rays. Some of them were found to contain voids and other were damaged in the cutting process. The samples were often cut immediately after the bonding, where the bond strength often is relatively low and this can be a problem since the cutting is a rough process. To ensure high success rate for the samples to be measured, IR picture were taken after the cutting.

A selected amount of reflectivity curves for the successfully bonded samples are presented here. The samples and corresponding process parameters are listed in table 5.1 below. All the samples were treated in DI-water before bonding.
Twelve samples have been measured and presented here, three made in the ICP-RIE system and nine in the RIE system. It was clear, that the reflectivity curves were sorted by the type of plasma activation used to generate the reactive surface of the two wafers(figure 5.9 and 5.10). Furthermore, the samples from the RIE chamber were split up in two groups. One

Technique	Sample	t [s]	$P_{RF\ platen/coil}$ [W]	p [mTorr]	d_{oxide} [Å]
	A	110	15/800	10	26.5 and 27.8
ICP-RIE	C	110	40/800	20	29.2 and 30.0
	A	190	40	280	39.1 and 38.1
	B	150	40	280	38.3 and 38.7
	C	110	40	280	36.4 and 36.6
	D	60	40	280	33.1 and 33.2
RIE	E	60	200	300	$\approx 95^a$
	F	60	200	300	$\approx 90^b$
	G	150	40	280	37.7 and 36.1
	H	60	40	280	30.7 and 31.5
	I	60	60	300	37 and 39

[a]The ellipsometer did not work; the thickness is an estimate based on experience with this recipe.

Table 5.1: Table of selected samples for x-ray reflectivity measurements[21].

group had curves that were characterized by having double peaks, with altering peak size and a another group had curves that were displaying multiple peaks of similar size.

The reflectivity curves of the ICP-RIE system are depicted in figure 5.9.
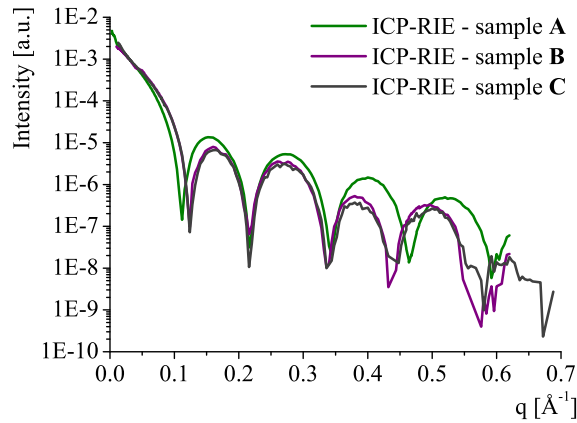
Figure 5.9: Xray reflectivity curves for three ICP-RIE treated samples.

The reflectivity curves of the ICP-RIE activated samples are very similar and have regular oscillation periods. The oxide thicknesses are nearly the same for all three samples, and this is in good agreement with the results from the optimization chapter, where it was found that the oxide thickness was not sensitive for recipe parameter changes. The width of the peaks can be related to a thickness value, and in table 5.2 is listed the found values considering each peak separately, the thickness found from the period of the sum of peaks and the

mean thickness by considering the mean oscillation period found for all observed peaks. For comparison is listed the oxide thickness values measured by ellipsometry.

peak nr.	1	2	1+2	3	4	3+4	mean(peak 1-4)	t_{meas}
ICP Sample A	60	49	27	52	49	25	53 ± 11	54
ICP Sample B	68	52	29	65	44	26	57 ± 5	59
ICP Sample C	68	52	29	56	68	31	61 ± 8	59

Table 5.2: Mean peak widths for ICP-RIE samples. t_{meas} is measured by ellipsometry[21].

The percentage deviations are rather high, but the total oxide thickness measured by ellipsometry before bonding is close to the mean value for all three samples, and as expected the lowest values are observed for sample A, where a lower power value was used, during activating the surfaces.

In the simulations it was found, that a regular oscillation pattern with one peak per period arose, e.g., for samples where the densities of neighboring layers in the oxide grown do not vary much and are close to be a simple box form. This will be further discussed later when fitting the data searching for the density profiles of the bonded samples.

In the reflectivity curves of RIE sample A-F, periods with double peaks are clearly present in different shapes and sharpnesses. This pattern is *not* observed for any ICP-RIE activated samples. Reflectivity curves for the RIE sample A-F are depicted in figure 5.10, and the thickness found from the peak widths are listed in table 5.3.
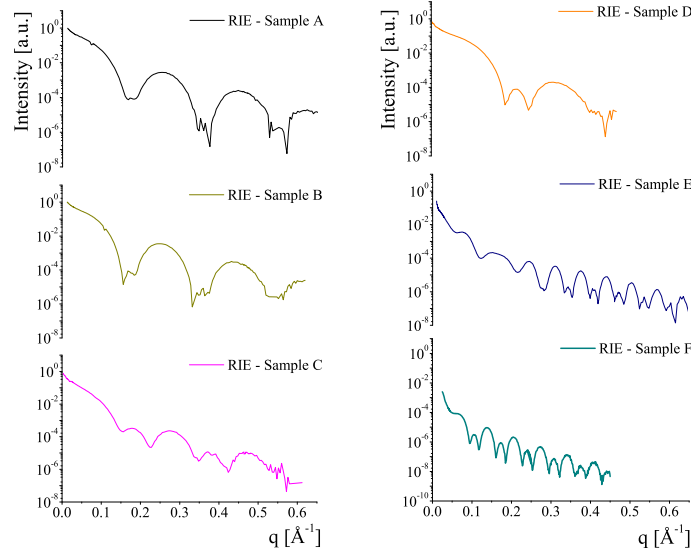
Figure 5.10: X-ray reflectivity curves for RIE sample A-F.

peak nr.	1	2	1+2	3	4	3+4	t_{meas}
RIE Sample A	524	38	36	196	41	34	77
RIE Sample B	196	44	36	196	40	33	77
RIE Sample C	87	52	33	87	49	31	73
RIE Sample D	105	40	29	-	-	-	66
RIE Sample E	314	137	95	314	150	101	≈190
RIE Sample F	273	143	94	262	146	94	≈180

Table 5.3: Peak widths and total oxide thicknesses for RIE samples with double oscillations. t_{meas} is measured by ellipsometry, and all values are given in [Å][21].

For all the samples listed in table 5.3, the thickness found from the widths of peak 1+2 and peak 3+4 are roughly equal to the measured thickness on one of the wafers used for the symmetrically bonded sample. Models with a repetition of a stack having adequate density variations between neighboring layers have been simulated by Egebjerg and it is speculated that the observed periods of peak 1+2 and peak 3+4 match the thickness of the stack, which is repeated.

Sample E and F are made with identical recipe and therefore identical reflectivity curves were expected. This is not exactly the case, but they behave relatively similar, which will be further discussed later. Compared to the rest of the samples in the group they are made with a recipe using a much higher power and therefore also the period in their curves are different. Sample A, B, C and D are made with same power and pressure but with different activation times. Using longer activation times affects the thickness and this was observed both by ellipsometry and in the reflectivity as oscillations of different periods.

The third group to be considered is sample G, H and I. Their curves and periods are shown in figure 5.11 and table 5.3.

peak nr.	1	2	1+2	3	4	3+4	5	6	5+6	t_{meas}
RIE Sample G	92	105	49	79	60	34	-	-	-	74
RIE Sample H	97	126	54	105	63	39	-	-	-	62
RIE Sample I	98	108	51	95	63	38	83	63	36	76

Table 5.4: Peak widths and total oxide thicknesses for data of RIE samples. t_{meas} is measured by ellipsometry, and all values are given in [Å][21].

The reflectivity curves for these samples display a different behavior than the ones described before the background became to high. Data for RIE sample G and H only contain four peaks, whereas six peaks are available for RIE Sample I. Some lengths show up twice when peak 1-4 are studied in all three samples, but in general there are no systematic values, which surely are to link with the measured oxide thicknesses. However, the two additional peaks,
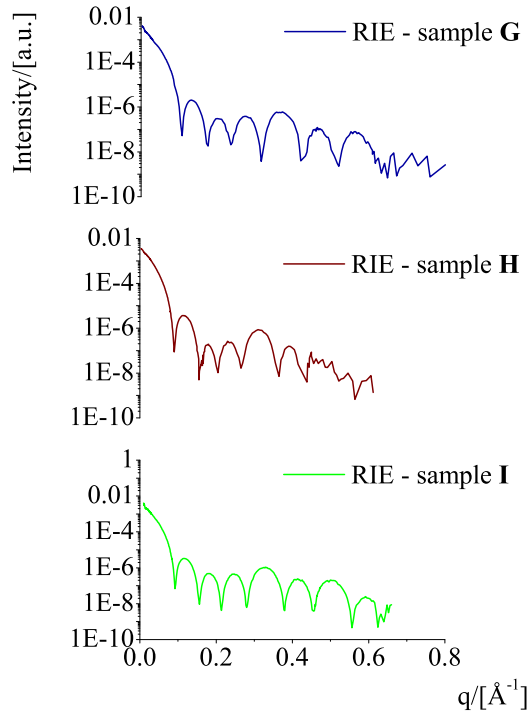
Figure 5.11: X-ray reflectivity curves for three RIE treated samples, G, H and I.

peak 5 and peak 6, in data for RIE sample I indicate a period consisting of peak 3+4, which is repeated in peak 5+6 and the widths of peak 3+4 and peak 5+6 can be related to the oxide thickness measured by ellipsometry before bonding.

Sample G and H are made with identical recipe parameters as sample B and D respectively, but despite of that, quite different reflectivity patterns are observed and the reproducibility of the samples can be questionable, which will be further discussed later, after discussing the result of the fitting.

5.4   Reflectivity fits

To develop a fundamental description of the bonded interfaces, two different analysis programs were considered, in order to find an optimized solution of the density profile. The box models described earlier, consisting of a few oxide layers of different densities are found to be too simple for describing the samples, but they were still of great advantage in the data fitting process, where reasonable input parameters has to be given.

Electron density profiles are determined by the inversion of reflectivity data. The reflectivity data do not contain information on the phase, and inverted phaseless data are inherently non-unique, because information is lost. Determination of the electron density profile there-

fore relies on the correct application of additional constraints, that eliminate non-physical solutions. A priori knowledge of the physical facts for the plasma bonded samples and other methods to analyze the samples was used to omit non-physical results.

The two programs used within the analyze are 1) The freeware programme Parratt32 [71], which was developed to calculate the optical reflectivity of x-rays from a flat surface and is based on Parratt's formalism. 2) The program, Reflectivity Fit developed by Martin M. Nielsen, Risø National Laboratory. For both programs the starting point is a set of reflectivity data as a given input, together with a initial guess of density profile. The generated reflectivity from the initially guessed density profile is then compared to the measured reflectivity data, and the best fit is found by minimization of the difference. The programs use the same reflectivity theory to treat the minimization problem, but the strategies for minimization are completely different.

It was experienced that using the fitting routine in Parratt32 resulted in reflectivity curves that were very similar to the data, but that the corresponding density profiles often were non-symmetric, very oscillating in nature and did not make physical sense. In the program it was not possible to add user-defined constraints to the input density profiles, but only functions to fit and even with functions as input model, the fit always converges in a local minimum with a non-symmetrical solution as the best estimate. The user interface indeed makes the programme simple to use, but there are too many limitations in the programme. The resulting density profiles are not interpretable, and the fitting process is rather time consuming compared to the actual outcome, and it was decided to primarily use the other program.

The programme Reflectivity Fit 0.45 was developed to handle the more specific features causing problems in the analysis of the reflectivity curves. It is implemented in MatLab, from where it is possible to adjust the thickness and roughness of a number of layers specified by the user. Contrary to Parratt32, extra constraints can be added according to the objective system. The fit routines are tailored to the systems and density profiles for each of the presented families of reflectivity curves are analyzed.

5.4.1   Comments on the program Reflectivity Fit

The starting point of this approach is a set of reflectivity data given as input value together with an initial guess of the density profile. The minimization problem then has to be solved in order to find the density profile that best matches the reflectivity curve. In this section some short comments on the program are given and more details can be found in [21]

The fitting programme is based on a box model with thickness, densities and roughness for each layer as input values. As a limitation each parameter is specified by a minimum and a maximum value, according to the physical limitations of the appropriate sample. The number of boxes is based on the physical properties given by plasma activation and bonding, i.e., the existence of three interfaces: Si-SiO_2, SiO_2-SiO_2 and SiO_2-Si. From the earlier simula-

tions, it is known that a simple box model is insufficient for describing the plasma-bonded system, and therefore a histogram model, which further split up the oxide regions in narrow profile bins, is employed, allowing small variations in the density through silicon oxide layer. In the program it is possible to choose between three different types of algorithms once the fit routine is started. Each one has its benefits and limitations. A description of the three algorithms used for fitting the reflectivity data in this work can be found in the appendix in the thesis by Egebjerg.

For describing the agreement between data and model fit either the quadratic derivation, the logarithmic derivation or the absolute derivation are used. The derivation is denoted as the R factor and the best choice of calculation method depends on the individual data set to be fitted.

To assure that the resulting density profiles actual make physical sense, weight functions are added in order to control the fitted density and omit solutions that are not reasonable. A weight factor, w, is assigned to the curve length to penalize solutions that oscillate rapidly, since it is not realistic and energetically favorable to form an oxide structure with very fluctuating densities on the Ångström scale. The weight function is entered by ensuring that the length of the unfolded density string does not exceed a value specified by the user. Further a weight factor, w_1, is assigned to ensure a symmetric solution with the purpose of omitting non-interpretable profiles, which do not match the preparation conditions. To optimize the function of applied weights, w and w_1, a Lagrange multiplier, L, is introduced, which has to be optimized regarding to both curve length and symmetry constraints. For more details about the Lagrange multiplier, see [21].

After optimization of the Lagrange multiplier, the histogram optimization is repeated in order to investigate the distribution of solutions and to get an overview of the reliability of reflectivity fits. For each sample presented is plotted a 90% confidence interval for the density, which means that there is a 90% probability that the true density solution falls within this given interval. Further a mean density is plotted for a large number of optimizations together with the density corresponding to the best optimization.

5.4.2   Fitting results

The first sample to be examined is sample A from the ICP-RIE group. The reflectivity curve for the sample clearly displays regular oscillations. In figure 5.12 the fitted reflectivity curve and the corresponding density profile is depicted.

In the reflectivity plot, both the calculated reflectivity from the mean density profile of 101 optimization runs and the best fit are showed, and as can be seen, they are both in good agreement with the measured data. For the reflectivity from the mean profile a slightly deeper curve is observed. The mean density profile and the previous mentioned 90% confidence interval are found in the left part of the figure. The confidence interval is very narrow, and the solutions are very consistent. This is supported by the distribution of R values,
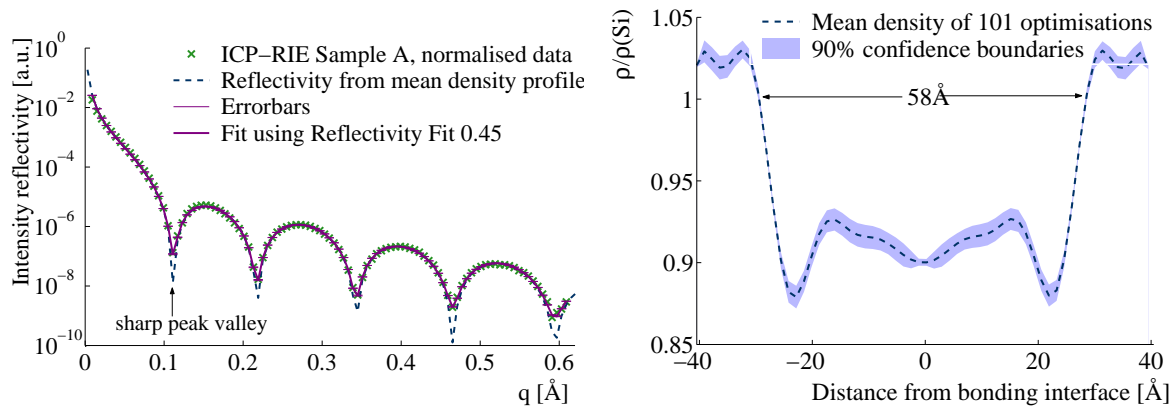
Figure 5.12: Fit of reflectivity curve, ICP-RIE sample A. Normalised data and the best fit of the reflectivity curve resulting from 101 optimizations with symmetry and curve length constraints. The reflectivity curve corresponding to the mean value of 101 density profiles is included as a blue dashed curve.

which were found to be grouped and have no sign of deviating solutions[21].

The density profile was optimized with constraints on symmetry and curve length, and the solution is perfectly symmetric with physically interpretable density values. The total width measured from each of the converging ends is 80Å, whereas it measures 58Å when the ends at almost constant level are omitted, which is close to 54Å as measured by ellipsometry.

The density values range from 2.41g·cm^{-3} to 2.03g·cm^{-3}. The standard density value for silicon is 2.33g·cm^{-3} which is slightly lower than the found value of 2.41g·cm^{-3} close to the silicon interface. At the bonding interface, z = 0Å, the fitted density is 2.10g·cm^{-3} and at the surrounding plateau, it is 2.16g·cm^{-3}. The total width of the plateau is approximately 35Å and the width of each density dip between the plateau and the silicon substrate is approximately 10-12Å.

The next sample that has been investigated is RIE sample A from the group of reflectivity curves having double oscillations, with different periods. The results of the fits are illustrated in figure 5.13
In the left part of figure 5.13 the measured reflectivity data, the best fit of the data and the reflectivity calculated from the mean density profile of all the symmetric optimization results are plotted. The best fit result is in good agreement with the reflectivity data, while the reflectivity curve corresponding to the mean density profile is slightly off indicating that the small peaks (peak 1 and 3) in the double peak period are difficult to reproduce. The peak valleys for the mean fit are sharper and deeper than the collected data.
In the right figure is depicted the corresponding density profiles. The mean profile is found from running 75 optimizations. Further is depicted the confidence interval and it can be observed, that the interval here is broader than the one found for the previous sample, and that the largest variation between the optimized solutions is observed around the bonding interface.
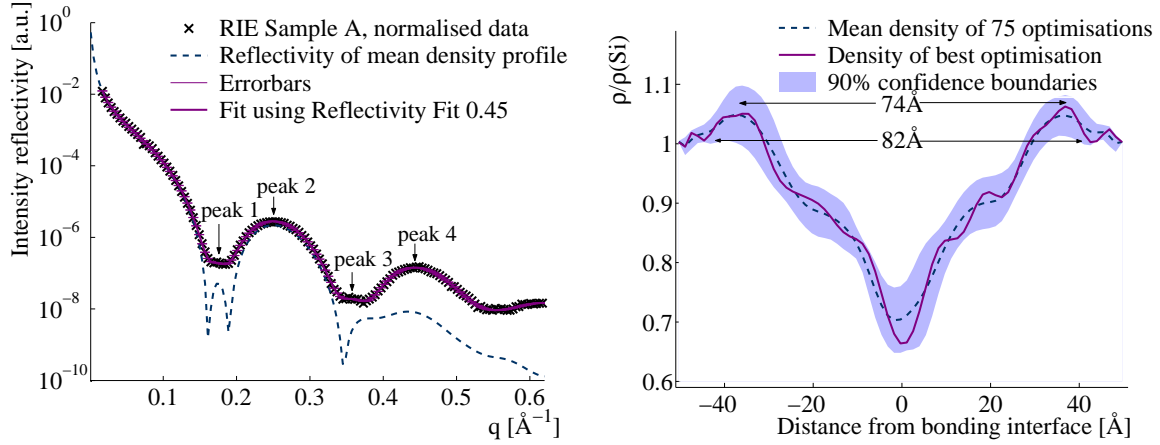
Figure 5.13: [21] Left: Measured data and reflectivity fit of RIE sample A are plotted and are in good agreement. Furthermore, the reflectivity curve corresponding to the mean density curve of 75 optimizations is depicted as a blue dotted line. Right: The density profile for RIE sample A. The 75 optimizations resulted in an almost symmetric mean density profile. The density profile corresponding to the best fit is depicted as well. The 90% confidence boundary is illustrated as a blue shadow excluding the non-symmetric solution

The densities vary from silicon oxide densities of $1.5 \text{g} \cdot \text{cm}^{-3}$ at the bonding interface to $2.5 \text{g} \cdot \text{cm}^{-3}$ close to the silicon substrate. The total thickness measured by ellipsometry is 77Å, which is in between the two given values in the figure. These values are the total width of the layers where the densities differ from the expected silicon value and the width measured from the two symmetric tops, where maximum densities are observed. The difference between the total width of the density fit and the measured thickness indicates, that a few Å of each Si wafer are disturbed by the oxide bombardment, or that the fitted thicknesses disagree. As observed for the previous sample a region of higher densities is found close to the silicon sample. Further it is observed that the density values close to the interface are remarkable lower for this sample, compared to result from the ICP-RIE activated sample. No plateau is observed, and in general a more triangular shape is found.

In this group of reflectivity data two additional samples have been considered, RIE sample E and RIE sample F. They are made from identical recipes within the activation process, and their measured reflectivity curves are similar in the sense that both have double oscillations, but they are not identical. It is of interest to compare the fits for these two samples, and also to compare them with other measurements, since they are made with a remarkable higher power value in the activation process(200W), compared to the other measured samples(40-60W). The results for the two samples are depicted in figure 5.14 and 5.15

It turned out that the fitting process for these samples was far more complicated than the earlier runs. For the RIE sample E in fact 241 optimizations were done, but most of them were not physically interpretable even though constraints were added in the fitting routine. As a result most of them were deselected and for sample E, only 32 optimizations were left. Figure 5.14 shows the fit of the reflectivity data for sample E. The best fit is in good agree-
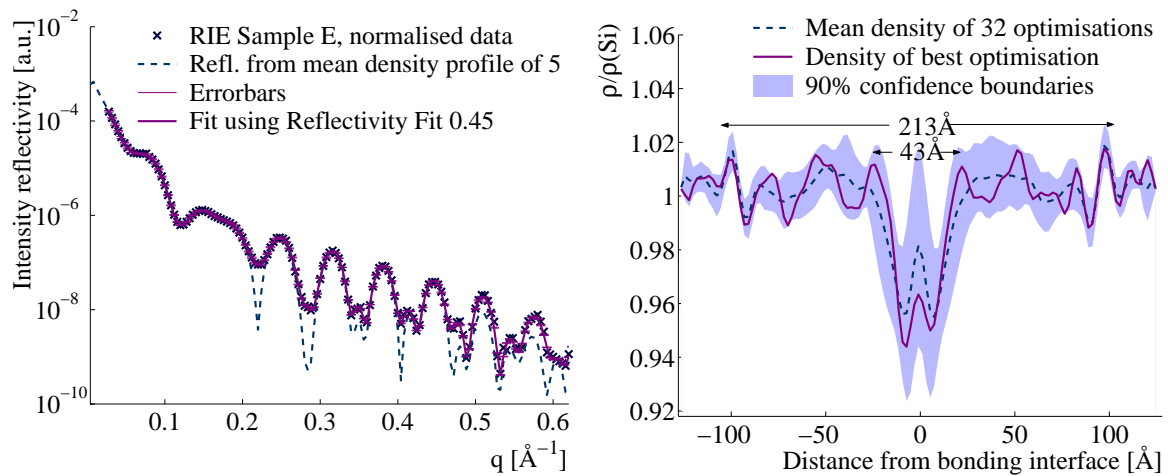
Figure 5.14: [21] Left: Measured data and reflectivity fit of RIE sample E. The reflectivity curve corresponding to the mean density curve of 32 optimizations is depicted as a blue dotted line. Right: The density profile for RIE sample E. The 32 optimizations resulted in an almost symmetric mean density profile. The density profile corresponding to the best fit is depicted as well. The 90% confidence boundary is illustrated as a blue shadow excluding the non-symmetric solution
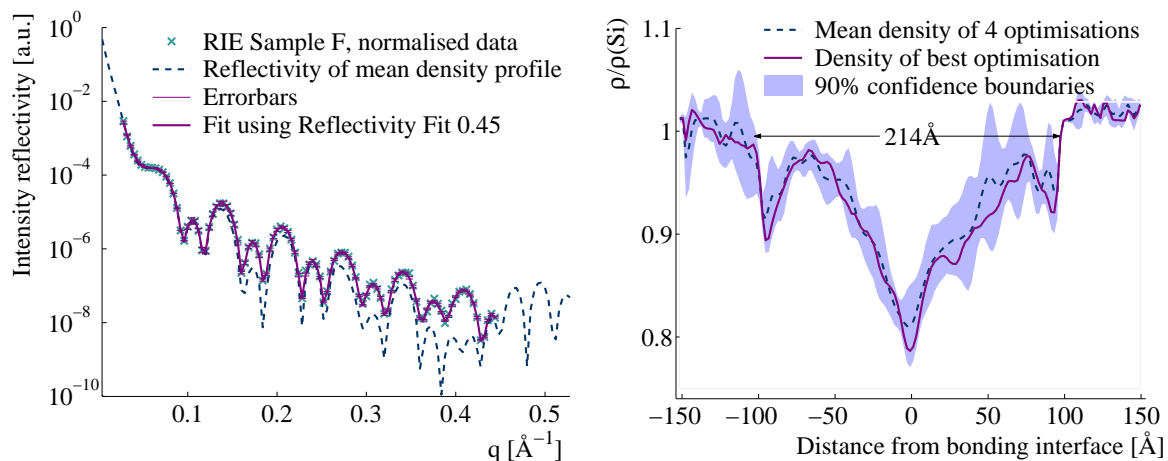
Figure 5.15: [21] Left: Measured data and reflectivity fit of RIE sample F. The reflectivity curve corresponding to the mean density curve of only 4 optimizations is depicted as a blue dotted line. Right: The density profile for RIE sample F. The 4 optimizations resulted in an almost symmetric, but very fluctuating mean density profile. The density profile corresponding to the best fit is depicted as well. The 90% confidence boundary is illustrated as a blue shadow excluding the non-symmetric solution

ment, but the curve calculated from the mean value is indeed off.

The density profile is presented in the figure on the right and it is clearly different from what is observed for the other fits. It covers a range from $2.38 \mathrm{g \cdot cm^{-3}}$ (2% higher than the density of silicon) to $2.19 \mathrm{g \cdot cm^{-3}}$ (the standard density value of silicon oxide), which indicates an

oxide layer that is more dense than the other samples prepared in the RIE system. Further the profile is very fluctuating and the confidence interval is even broader for this sample. The region with adequate variations from the converging density value measures 213Å, which is more than the expected 180Å, and only a narrow region of approximately 40Å around the interface has a slightly lower density value.

The results for RIE sample F are found in figure 5.15. The same problems with the fitting were found and therefore only four optimizations are used. Again the best fit is in good agreement and the mean value reflectivity fit off. The confidence interval for this sample is also relatively broad and the density ranges now from 2.42g·cm^{-3} to 1.80g·cm^{-3}, which is remarkable lover than before. The total width of the density profile is 300Å, and the region where an adequate relative density is observed measures 214Å, which is close to the value stated for sample E of 213Å, but this sample seems to have a broader region around the interface with a lower value of density. RIE sample E and RIE sample F were activated using identical power settings, and the density level and total oxide thickness for the two samples were supposed to be roughly equal. This is not the case, and therefore it can be argued that maybe the reproducibility for the samples is rather poor. Great care should therefore be taken to interpret the results from the measured reflectivity curve as a good description for the sample prepared using a special combination of recipe parameters.

The last sample to be presented is RIE sample I from the third group of reflectivity curves, which was far more simple to analyze.
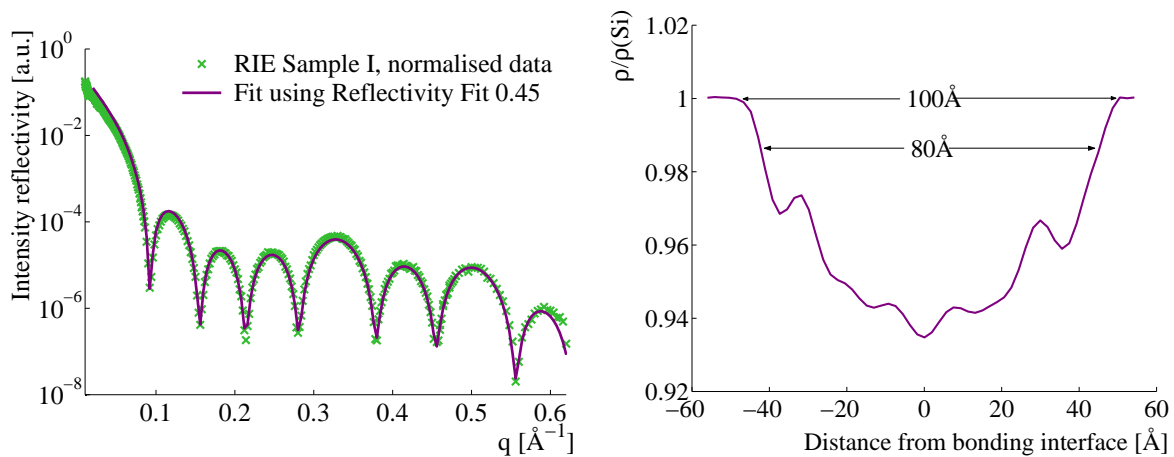
Figure 5.16: [21] Left: Measured data and reflectivity fit of RIE sample I. The reflectivity curve corresponds to the density curve of only one optimization. Right: The density profile for RIE sample I. The optimization resulted in a symmetric density profile.

The reflectivity fit of RIE sample I provided a nearly perfect match without applying a detailed optimization with additional constraints. The density profile was smooth, almost symmetric and does not show any non-physical features. The density varies from 2.33g·cm^{-3} to 2.18g·cm^{-3} at the bonding interface. The value at the bonding interface is 0.8% lower

than the standard value of silicon oxide, and the density converges towards 2.33g·cm^{-3} at the Si-SiO$_2$ interfaces. The width of the total density profile is 110Å, whereas it measures 100Å if the converging ends are omitted. If the outermost 'step' and matching roughness are excluded, the oxide is 80Å broad, which has to be compared with 76Å measured by ellipsometry. Depending on the thickness, a transition region in this sample is 5-15Å per wafer, and there is no indication of an interface layer with a density exceeding the density of crystalline silicon, which has been observed earlier.

RIE sample I was activated with a power of 60W, which is far below the power used in RIE samples E and F, where density values above 2.33g·cm^{-3} for silicon were observed. This indicates that the power directly affects the densities of the generated layers, creating more dense layers when higher power values are used. The exposure time for sample I was 60s which is around 30% of the process time used in RIE sample A, where also two high density symmetric tops were observed as neighboring layers of the silicon wafers. This indicates a density dependence of activation times.

5.4.3   Discussion of reflectivity fits

In the previous section different reflectivity curves were considered and divided into three main types. The presented curves have common features as well as individual features, which can be compared with the resulting density profiles and the used process parameters in the surface activation. In general, sharper and deeper peak valleys were observed in the reflectivity curves generated from the mean density profile fits compared to the best fit. It was found that the number of included optimizations clearly affects the derivation from the best fit and great care should be taken that only reasonable solutions should be selected and included in the optimization runs.

Double peak periods are clear in RIE samples A-F, and they are closely related to the density levels in the oxide layer. According to the model simulations, this oscillation pattern appears, when a layer or multilayer has a density profile with dips. The relation between the width of narrow and broad peaks is controlled by the relative density variation in the profile. Neighboring density levels that are equal, cause regular periods. Levels that are close, cause a very narrow peak 1 and a broad peak 2, whereas sharp dips cause the period to split up in two peaks with very different widths.

RIE sample E and RIE sample F were activated with identical process parameters (60s, 200W and 300mTorr). In general, the reflectivity curves of the two samples behave equally, c.f. figure 5.14 and figure 5.15. The periods of the two curves are almost identical (peak 1+2 and peak 3+4), which is expected since identical process parameters are used for plasma activation. Even though the samples are expected to be identical, the density profiles obtained from the fitting of the data of the two samples, are somewhat different. The range of relative density variations throughout the oxide layer in the best fit of RIE sample E is (0.94-1.02) which is less than the range for the best fit of RIE sample F (0.79-1.03). Further the density of neighboring layers in RIE sample F differ more than in RIE sample E. This difference is in agreement with the peaks in the reflectivity curves, which are sharper in sample F but clear

in both cases[21].

In both density profiles, there is an indication of a narrow region bordering the silicon wafer with a density dip. Approaching the bonding interface, the density rises before it declines towards the bonding interface. It is funnel-shaped in RIE sample F, and in RIE sample E there is a small extra density peak in the bonding center. RIE sample E and RIE sample F were activated using the highest power allowed with standard time and pressure settings. Thus, it is surprising that the overall density levels are not equal, when the ion bombardments in the RIE chamber were carried out using the same settings. For sample F the first shoulder in the oscillations is observed with an intensity of approximately 10^{-4} whereas for sample E the intensity is almost a factor of 10 lower. The observed intensity difference is not expected, and can be due to errors in data normalization.

Further it should be remarked that the fitting of these types of data with double oscillations of different size was very difficult. Typical the optimization runs ended with a physical unrealistic solution, and only a few runs were included in the final profiles. As can be seen in the earlier presented graphs of the density profiles the derivations of the mean reflectivity curves were relatively large, and for both samples a large confidence interval was found indicating large uncertainties of the profiles.

In conclusion it is not clear if the difference in the profile is only related to normalization and data fitting problems or also related to the reproducibility of the samples. Despite of that, a general tendency is that more dense oxide layers are formed, compared to the other samples. It is reasonable, that a more dense oxide layer is obtained, when the oxide is generated with high power consequently causing ions to pelt the surface more aggressively.

RIE sample A has a different double oscillation pattern, where peak 1 is remarkably smaller than peak 2 with respect to intensity as well as width. The reflectivity curve of RIE sample A is reproduced by successive fits and depicted in figure 5.13. The peaks are not sharp, but rather have a tendency to be smeared out. In the corresponding density profile, there are no dips with large and abrupt differences. The profile is soft and V-shaped with terraces approximately midway between the bonding interface and the silicon wafer. This soft shape with small relative changes in densities between neighboring layers is in agreement with the ratio between peak 1 and peak 2[21].

The relative density level corresponding to the best fit of RIE sample A is ranging from 1.05 to 0.67, which is considerable lower than what was found for sample E and F. Further the profile is more triangular with a relatively decrease in density already close to the silicon. Activation in the RIE chamber was carried out with almost same pressure, but with lower power settings and longer activation time, and this is believed to cause a broader and lower density profile.

In RIE samples G-I, the multiple oscillation was less pronounced and not perfectly regular. Nonetheless, there is an indication of double oscillations. The sample was prepared in the RIE chamber using the same time and pressure settings as used for RIE sample E and F, but

the power was only 60W. The ratio between peak 3+4 as well as peak 5+6 is closer to unity, which is in agreement with the smooth density profile, where the relative density is between 1.0 and 0.93. There are small dips and terraces, c.f. figure 5.16, but none of them are sharp and abrupt. The widths of different layers in the oxide differ by few Ångström according to the profile, and cause the reflectivity peaks to be rounded, whereas peak valleys are sharp.

Comparing sample I(60s/60W/300mTorr) with sample E and F (60s/200W/300mTorr) indicates that changing the power to higher values results in broader rounded oxide density profiles, with a relatively broad range around the interface with a lower density. Compared to sample A (190s/40W/300mTorr), which is made in the same power range, but with much longer activation time the profile is still more rounded and the density range level considerable higher, and this indicates that prolonging the activation time also have an important effect on the generated oxide layer, especially in a narrow region around the interface. It is possible that due to the relative low power, the ions hitting the surface primary affect the outermost oxide layer, and therefore density changes close to the bonding interface are observed.

ICP-RIE sample A was prepared in a different chamber, which is supposed to produce a more dense and homogenous oxide [41, 10]. The reflectivity curve of ICP-RIE sample A, has very regular oscillations and a period of one peak. The density profile is smooth, and there are no abrupt changes or sharp dips in the density that cause neighboring layers to differ enough to produce double oscillations. Nonetheless, the density level varies more than, e.g., observed for RIE sample E. Thus, a difference between the widths of peak 1 and peak 2 was expected. An explanation for the lack of this feature might be the use of a different plasma activation-method. In general all measured curves for the ICP-RIE prepared samples seemed to much more regular. The shape of the density profile is different compared to what is found for samples made in the RIE chamber. The profiles are compared in figure 5.17below.
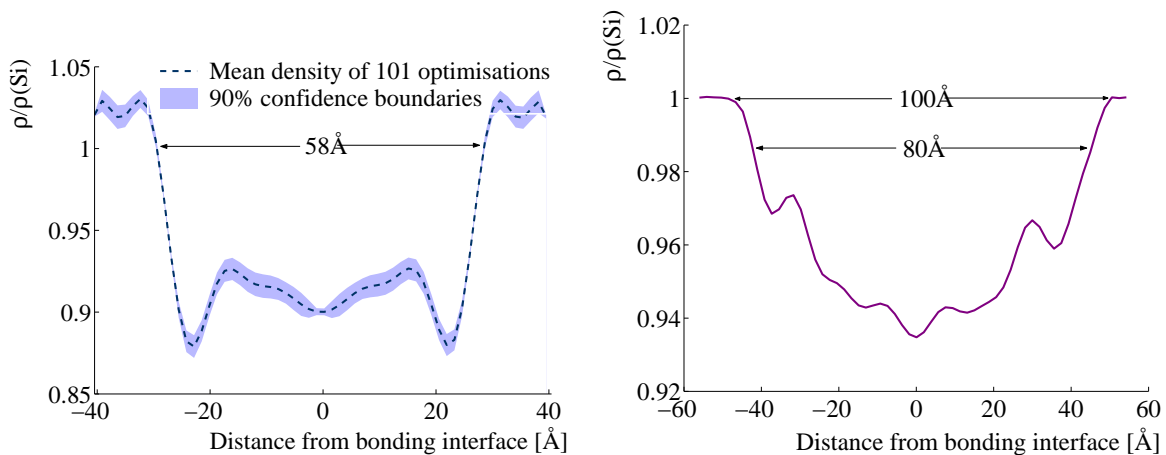
Figure 5.17: [21] Density profile for sample ICP-RIE A and sample RIE I.

For the ICP-RIE prepared sample, a broad intensity dip is found close to the silicon surface.

The intensity drops rapidly and then goes up to an almost constant level around the bonding interface. The thickness of dips and terraces in the profile of the oxide does not remarkably vary, but a small dip is observed at the interface, which is common for all the samples, but in general it is more pronounced for the RIE prepared sample.

The level of density profiles for all the samples were compared with the process parameters, and the density of the bonding-interface oxide is clearly a function of the RF power. However, it is not clear whether a lower pressure and power setting are the only factors causing a less dense oxide layer in e.g. RIE sample A. Further data optimization on series of samples with different process parameters is needed. All density profiles have a dip around the bonding interface, but the levels of oxide density and the shape of the dip vary from sample to sample. This confirms the existence of a linking layer but makes it difficult to propose a structure.

For some of the profiles, the confidence interval was broad at the bonding interface, whereas other data resulted in a very good agreement between all the optimizations. The oxide layers on the wafers are not identical, but variations on the Ångström scale are not expected to be reflected in the density profiles. For one sample, RIE sample E, the density peaks at the bonding interface indicate a linking layer between the two oxides, which is more dense than surrounding layers in the oxide[21].

The programme Reflectivity Fit 0.45 was observed to reproduce reflectivity data successfully, and the fitted density curves are physically reasonable. The correlation between process parameters, which were used to activate the inspected samples, and the density level of profiles was investigated. Furthermore, the form of each profile was analyzed. There are clear indications of interfacial density dips close to the Silicon, which are typically 10-20Å wide. There is a region with low density around the bonding interface for all the samples, except for RIE sample E, but the shapes are somewhat different. In order to compare the density profiles of samples made from different recipes and thereby analyze the effect of RF power and chamber pressure thoroughly, optimizations on additional data sets are needed.
The optimized density profiles indicate that the oxide layer has a graded density. It is smeared out, either by the inter diffusion of oxygen atoms resulting in a non-homogeneous silicon oxide or by formation of transition layers where new states of silicon oxide are formed. The interfacial density dips indicate an abrupt interface between crystalline and amorphous materials.

The observed dip at the interface in the fitted data is also reported by Rieutord et al[62, 63]. In [62], they are measuring on bonded hydrophilic wafers of native oxide and thermal grown oxide, whereas their systems are different from those investigated here. For the data fitting, they have been using a simple electron - density box model, where the density dip at the interface is modelled by a gaussian well. In their profiles homogenous layers of oxide are used, which is also to be expected from thermal grown oxides. They have measured the density profile as a function of temperature, and at room temperature they report an interface dip of width 4.4 Å and a density gradient depth of 0.23 $\overset{\circ}{A}^{-3}$. As the temperature increases, the width increases and the depth of the dip decreases. In comparison the typically width of the interfacial dip for our samples is much broader and the depth very varying depending of

the sample parameters, and it is clear, that the oxide layer produced by plasma activation results in far more fluctuating density profiles.

In the other paper by [63], investigation of reflectivity from standard hydrophilic silicon bonding is discussed. The profile was found by direct inversion of the reflectivity data, and also here the interfacial dip is found, and again the size is a function of temperature. They observe small shoulders in the profile which are attributed to native oxide and in some temperature range a relatively wide dip profile is observed and speculated to be due to nanometer micro voids. Compared to the density profile found for the plasma assisted bonding, these profiles are much more smooth in shape and the depth at the interface for the room temperature bonding is found to be far more pronounced with a $\rho(z)/\rho_{Si}$ ratio of approximately 0.5.

5.5   Summary and conclusion

The interfacial oxide between two plasma activated silicon wafers was studied through a set of complementary techniques that operate on the micro- and nano-scale. The aim was to obtain structural information about the bonding, which could contribute to a better understanding of the details within the low temperature plasma activation bonding process.

Recipes of two reactive etching systems, RIE and ICP-RIE, that deposit an oxide layer were tested and optimized in order to obtain the highest possible bond strength. For both types of activation, a general improvement in sample preparation was obtained, and an optimized recipe that resulted in reproducible bond strengths and a high yield of samples without voids were developed. The optimized bonding process occurred spontaneously when the two wafers were adhered, and the bond strengths were high compared to those obtained by other room temperature techniques. This process renders heating superfluous and is therefore of great interest in instances where a subsequent annealing step hampers the intended application.

An improvement of the bond strength test equipment would be an easily applicable method, which is able to perform reproducible measurements independent of the person who performs the tests. This demands a reconstruction of the test equipment, a sharper razor blade made of a harder blade steel and that the separation is done automatic instead of manual. Furthermore it was found that control of the ambient air (e.g., the humidity) by sealing the test equipment in an appropriate box would affect equilibrium conditions and thereby contribute to a stable method. If a not optimized system is still used for the test, it would be of great advantage, if at least the measurements condition and statistic are specified in details.

Since plasma bonding is a sensitive process, it should also be considered to do in situ bonding, where activation and bonding take place in a closed chamber. This is recommended for implementation in industrial set-ups, and this way, the time delay between activation of the surface and the bonding is in good control, and contaminations from handling the wafers manual are avoided.

Water and porosity

The effect of water treatment before bonding has been extensively discussed in other studies, but no definitive explanation exists. In general by including a water treatment after the surface activation, spontaneous, strong and stable bonding was observed, whereas no water treatment resulted in samples where non-bonded areas often were dominating.

To investigate the influence of water in more details Egebjerg performed TOF-SIMS experiments of D_2O treated samples and further the idea of the surface consisting of micro-pores was investigated by TEM measurements. The latter was proposed by Amirfeiz et al. and Sanz-Velasco [65, 3], which suggest that the oxide formed under activation is porous, having micro pores that collect excess water from air moisture and the waterdip. The TOF-SIMS experiments of the D_2O treated samples showed however, that the water treatment affects only the outermost atomic layer on each plasma activated silicon wafer and from the TEM measurements, pores on the nano-scale were clearly disproved. Thus, there is no indication of a porous oxide, and only a hydrated mono- or bilayer is present. Water is transported by diffusion on internal surfaces as a mono- or a bilayer and this is considered to explain the importance of the water treatment, which is believed to ease the bonding by bridging the gab[21].

Effect of plasma activation

The oxygen plasma treatment of the surfaces affects the reactivity of the two wafers, whereas it is important to study the relationship between changes in the process parameters and the bond strength of bonded wafers. In the optimization work, it was found that recipes could be optimized, to yield a high bond strength for RIE and ICP-RIE activation techniques. In general the effect in bond strengths was most sensitive when changing parameters in the RIE system.

The ion bombardment, which takes place in the plasma chamber, changes the chemical state of the oxide and consequently increases the reactivity of the surfaces. The conditions, under which an increased surface energy is achieved, are balanced between the increased reactivity and the degradation of surface quality when the ions are too energetic at a high RF power.

Density profiles and reflectivity curves

From the measured reflectivity curves and modelled density profiles clear indications of small density dips close to the Si-SiO$_2$ interface and a dip around the bonding interface were found. The latter had different shapes for the samples presented here, and in order to compare the density profiles of samples made from different recipes and thereby analyze the effect of RF power and chamber pressure in detail, we must conclude that additional data sets are needed. The used x-ray geometry is indeed suitable for measuring bonding interfaces, but it was experienced during the work that the samples were very sensitive for the cutting and mounting process. The room temperature bonded sample is relatively week immediately after adhesion. It is known that the bond strength is raised considerable already within the first 24 hours after bonding, and it is believed that this can affect somewise the measured data. The

samples are after the cutting stored in plastic boxes and transported to the beamline, and measured as short as possible afterwards. Since it is not possible to measure on more than one sample at a time, a time delay between the different sample was difficult to avoid.

Immediately after the bonding the wafers are cut in narrow strips of only a few hundredths of microns and in the cutting process the diamond blade and sample are covered with water for cooling. The actual bonded areas are after the cutting were small and it could be possible that the water penetrates through the side and affects the bonding structure.

It is known from other similar bonded systems that the observed increase in bond strength as a function of storage time is related to water rearrangement and diffusion, either to bulk or along the interface to the sample edge[70]. Typically the strength increases within the first few days and reaches a stable saturated value often 2-4 times what is observed immediately after bonding. The path length within the narrow stripes used in the set-up is very short and it could be, that for the strips an increased stable bond strength is observed on a much shorter time scale, and already a few hours after cutting no further interface changes are observed.

Some tests were performed to investigate the stability of the samples. For several samples not only reflectivity from one interface area was measured, but also at different positions along the interface. The results were identical and from this it can be concluded that the reproducibility within each sample is good. The same samples were also measured with a time delay of tree months, and the results were identical indicating that the long term stability of the sample is high.

Future work

Indeed more measurements should be done to reproduce data on bonded wafer samples, with specific activation parameters. Further measurements on small pieces of activated single wafers should be performed(Small pieces are not expected to bend as much as whole wafers, and it might solve the problem of collecting data on these samples).Thus, it would be possible to compare the fitted density profiles of the thin oxide film before and after bonding as well as investigate structural differences.

Further it is suggested[21] that chemical analysis with an electron microscope can be invoked by electron energy-loss spectrometry, energy filtered TEM and scanning TEM. Also a detailed study of the interface by EELS will be of great advances in the search for a detailed model of the atomic structure of the plasma assisted room temperature bonding.

Chapter 6

Introduction to Waveguides

During the last years there has been a considerable interest in achieving micro-focusing of high brilliance x-rays generated at third generation synchrotrons. Producing x-ray beams with high flux and significant small spot size open up a whole new range of applications in scattering, microscopy and spectroscopy with a real space resolution down to the nanometer range. Examples of interesting applications are elemental analysis of nanoparticles by x-ray scanning fluorescence microscopy, high resolution x-ray tomography, sub-micrometer magnetic analysis of semiconductor nano-structures or x-ray coherent diffraction experiments[54].

The sub micrometer spot size can in principle be achieved by using slits or pin holes apertures, but a limitation is either imposed by the availability of suitable sufficient absorbing materials, especially for the hard x-rays with a wavelength < 0.1 nm or the precision of the fabrication process, and even if, hypothetical pinholes of such size were available, the flux throughput would not be sufficient[54]. To obtain high flux beam spots, the x-rays can be focused either coherently by fresnel zone plates and bragg fresnel lenses or incoherent by planar waveguide of varying cross sections, capillaries, mirror optics and compounds of refractive lenses[54]. For incoherently focused x-rays, spot-sizes of about 100 nm are reported in the wavelength range of 0.1-0.15 nm by glass capillary optics, whereas mirror optics is reported to produce spots below 800 nm, in the same wavelength range. Compound refractive lenses reports a spot-size of 8.0 micro meter at $\lambda = 0.089$. Using coherent focusing optics, fresnel zone plates spot-sizes of 29 nm is observed for $\lambda = 2.4$ nm, but due to absorbtion and phase shift with increasing energy it is very difficult to obtain small coherent spots for the hard x-rays below 0.1 nm. For the hard region the smallest reported spot size is in the range of 500 nm [54][55][27].

X-ray waveguide structures presents a new approach which is an alternative technique for obtaining very intense fully coherent micro or even nano beams. Precisely defined beam properties concerning shape and coherence are obtained based on the principle of resonant beam coupling, and the size of the beam at the exit of the guide is smaller than the thickness of the guide layer[38]

The basic principle of a simple waveguide structure is illustrated in figure 6.1.
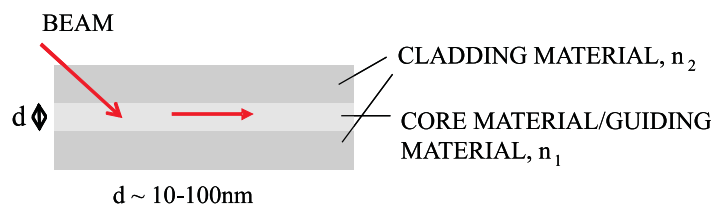
Figure 6.1: Basic principle of a simple waveguide structure.

The typical x-ray waveguide structure consists of a low density core material with refractive index n_1 and a typically thickness in the order of 100-150nm. The core material is surrounded by layers of cladding material, with a different higher refractive index, n_2. The structure in the figure have identical cladding layers, but for some systems these are different. The beam is coupled into the guide either through the cladding layer or from the front of the guide(not shown in figure). The structure allows the formation of a strong x-ray standing wave field in the guiding layer, with a periodicity depending on the incident angle and of the structure geometry. Each time the standing wave periodicity is an integer fraction of the layer thickness a resonance takes place, and the resonantly enhanced electromagnetic fields travels along the wave guide and exits at the end. The out-coming beam will have in one dimension the size constricted by the guiding layer thickness. For a guide with thickness 130-160 nm is the size of the beam produced by the waveguide about 65-80 nm.[16].

The first attempt to fabricate and study waveguides for hard x-rays were performed in 1974 by Spiller and Segemüller [66]. They demonstrated, that the principle of guiding electromagnetic radiation could be extended into the x-ray range. In their work, they made a waveguide structure consisting of a BN film(300-500Å) sandwiched between an Al_2O_3 cladding and by coupling x-rays through the topcladding layer, they successfully demonstrated the excitation and propagation of single modes over a length of 0.3 mm, for x-rays with 1.54 Å wavelength. However, due to the coupling mechanism, non ideal material choice and geometrical properties of their structure the resulting efficiency was relatively low.

Several years later Feng et al.[26, 27] demonstrated the principle of a planar dielectric waveguide structure for which they were achieving significant flux enhancement by coupling a highly collimated, monochromatic synchrotron beam through a cladding layer into the guide medium. The investigated structure consisted of a thin film polyamide guiding core on top on a silicon substrate and a SiO_2 layer used for top cladding. Using the Resonant Beam Coupling scheme(RBC), they observed a 20-fold flux increase, and thereby suggesting that this is the most sufficient way of coupling intensity into the waveguide.

In 2002 Pfeiffer et al. published a paper demonstrating two-dimensional(2D) x-ray waveguiding [55]. Previous work within the area has mainly been exclusively studies of one dimensional waveguide structures, but since most interesting nano beam applications would require two dimensional pencil like beams, this paper is indeed important. They investigated a 2D structure made of poly methyl methacrylate (PMMA) as core material and Cr chosen as cladding material on top on a Si(111) wafer. Using resonant coupling of synchrotron beams

into the structure, they successfully produced a coherent x-ray point source with dimensions of 68.7 nm times 33.0 nm at the exit of the waveguide structure which was the smallest spot size ever archived for hard x-rays. In conclusion they demonstrated the proof of principle that such devices can be used for making nano-beams, but the perspective of a powerful x-ray point source is only realistic in the coupling efficiency can be considerably increased over the value estimated for the fabricated structures in the paper. For improvements they suggest, that devices with higher perfection like the interfacial roughness and homogeneity of the layers should be developed and that further progress may derive from improved material composition or adapted pre-focusing optics.

Last year, Jarre et al. [37] published a paper, where a two dimensional confining x-ray waveguide structure is combined with a high gain Kirkpatrick-Baez(KB) prefocusing mirror system resulting in a hard x-ray beam with a cross section of $25x47nm^2$(FWHM). The incoming beam is no longer coupled in the RBC scheme, but now from the front side whereas the beam is no longer accompanied by disturbing spurious reflected or transmitted beams. Using the front coupling(FC), the total count rate would be lower than for the RBC waveguides, since they do not provide an intrinsic increase in flux. This problem can nevertheless be solved by using the property that the angular acceptance of the FC waveguide is in the range of some hundredths of a degree, which matches the focusing angle of the presently most efficient focusing x-ray optics, and by using such optics to increase the total flux Jarre et al . successfully report well defined intense hard x-ray nano beams. For further improvement the authors suggest to use higher demagnification ratios of the KB optics and hence smaller over illumination, in combination with a waveguide structure down to a 10nm cross section. Furthermore it is suggested that the ideal waveguide structure consist of vacuum instead of a polymer core and is fabricated by techniques such as wafer bonding, focused ion beams or nanotubes.

Making waveguides using air as guide medium has been done in the work by Zwanenburg et al.[80, 81]. They were investigating a tunable x-ray waveguide with an air gap as the guiding medium, and in their paper they report discrete transverse-electric(TE) modes excited in the air gap. They are propagating almost undisturbed through the planar waveguide with essential no attenuation and with negligible scattering losses to other modes, and it is suggested that filling the air gap with a fluid allowing for studies of ordering phenomena in a confined geometry. Relatively high transmission was found, typically around 98%, and typically values of gap hight are between 250nm-650nm. The beam is coupled into the guide from the front, but since a larger bottom plate is used, the incoming beam is totally reflected into the guide rasing the efficiency. The dimensions are restricted to the control of the plate positions by the used pierzo motors. Compared to the previous mentioned structures they are much higher, and ultimately they would like to reduce the gap to a few nanometers thereby allowing study of the structural ordering of liquids on a molecular scale.

6.1   X-ray waveguides made by waferbonding

The waveguides investigated in this project is made by etching nano-structures in silicon and using the wafer bonding technique for closing the etched structures thereby obtaining nanometer dimensional air channels buried in silicon. The principle is illustrated in figure 6.2.
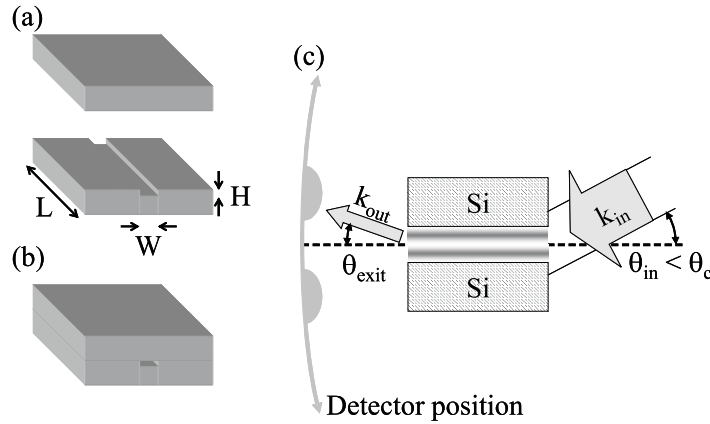
Figure 6.2: Sketch of fabrication of waveguides with wafer bonding

Air is used as guiding medium and the silicon as cladding material. The beam is coupled into the guides from the front(FC) and the expected mode propagation is investigated in the farfield region at the exit of the guide. The fabrication technique has not previous been used for fabricating x-ray waveguides, and the work presented in this thesis has been focused on characterizing the structures and making first proof of principle experiments demonstrating that using this technique it is possible to fabricate useful waveguides. Using the FC scheme, the efficiency of the investigated guides is relatively low, since the guide entrance are very small compared to the dimensions of the beam. This problem will be further discussed in the next sections, but could be solved by using a prefocusing mirror system as described earlier.

In the next chapter, the theory related to the waveguide propagation is described and in chapter eight are a description of the used fabrication methods followed by a section of characterization of the structures. In chapter nine are a presentation of the measured farfield modes for a selected amount of the investigated structures compared to what was expected from the theoretical considerations. The work is summarized at the end of chapter nine. Part of the work related to the fabrication of one dimensional guides can be found in the paper [58] and the results of the two dimensional guides in [59]which are in progress.

Chapter 7

Waveguide theory

In this chapter we will go through the theoretical considerations needed to describe the concepts of an x-ray waveguide. The first section(8.1) describes the simplest waveguide structure, a planar waveguide, were waveguiding only takes place in one dimension. We start with Maxwells equations applied on plane electromagnetic waves. This yields the one-dimensional reduced wave equation witch then has to be solved using the boundary condition for the system. The boundary condition on the plane electromagnetic wave, lead to the transcendental equation witch is central in the mode description of waveguides. The next section(8.2) contain the theory for a rectangular waveguide, where waveguiding in two dimension can take place. Again we end up with two transcendental equation describing the modes. There after will be a description of the far field intensities (8.3) and at the end of the chapter a discussion of different coupling methods(8.4), their efficiency, and gain values(8.4). The theoretical description used in the chapter is based upon the treatment of optical waveguides. The extension to x-rays is made by taking into account the appropriate x-ray optical description[42, 54].

7.1 Planar waveguide theory

The most simple type of a waveguide is a symmetric slab waveguide consisting of one core layer of refractive index n_1 with a medium below and above having a smaller refractive index n_2. The guide is considered to be infinite in the direction perpendicular to the propagation direction(y). The modes propagating in the waveguide are described by Maxwells equations.

7.1.1 Maxwell's equations

Maxwells equations for a uncharged, nonconducting and nonmagnetic medium can be written in the form

$$\nabla \times \mathbf{E} = -\frac{\partial \mathbf{B}}{\partial t} \tag{7.1}$$

$$\nabla \times \mathbf{H} = \frac{\partial \mathbf{D}}{\partial t} \tag{7.2}$$

$$\nabla \cdot \mathbf{D} = 0 \tag{7.3}$$

$$\nabla \cdot \mathbf{B} = 0 \tag{7.4}$$

where the fields can be connected through the material equations

$$\mathbf{D} = \epsilon_0 n^2 \mathbf{E} \tag{7.5}$$

$$\mathbf{B} = \mu_0 \mathbf{H} \tag{7.6}$$

and ϵ_0 and μ_0 are the vacuum dielectric permittivity and magnetic permeability given by $\epsilon_0 = 8.854 \times 10^{-12} C^2 N^{-1} m^{-2}$ and $\mu_0 = 4\pi \times 10^{-7} N s^2 C^{-2}$.

For x-rays the refractive index, n, can be written

$$n = 1 - \delta - ib \tag{7.7}$$

where δ can be expressed by[2]

$$\delta = \frac{2\pi \rho r_0}{k^2} \tag{7.8}$$

ρ is the electron density, $r_0 = 2.82 \times 10^{-5} \mathring{A}$ and k is the wavevector related to the wavelength of radiation, $k = 2\pi/\lambda$. The value of δ is in the order of 10^{-6}.

In expression 7.7, b is connected to absorption, which implies that the beam is attenuated in the material with a characteristic 1/e length denoted by μ^{-1}. and μ is the known as the linear absorption coefficient. b is expressed by

$$b = \frac{\mu}{2k} \tag{7.9}$$

The solutions to Maxwells equations describe the modes propagating in the waveguide and they can be classified in two types, transverse electric(TE) or transverse magnetic(TM)modes [42]. The TE modes do not have a component of the electric field in the direction of wave propagation, while TM modes do not have a longitudinal magnetic field component. For x-rays the difference between TE and TM modes is very small since all propagations angles are within fractions of a degree, and in the description we will only focus on the TE modes which corresponds to the experiments.

7.1.2 Planar Waveguide

The simplest planar waveguide structure is sketched in figure 7.1. It consists of a film with refractive n_1 sandwiched between two semi-infinite layers of refractive index n_2.
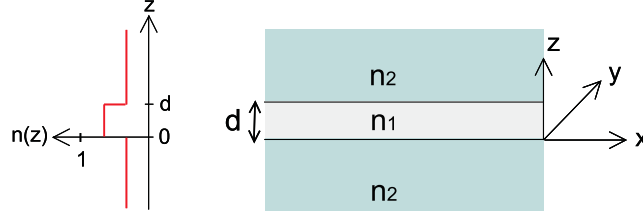
Figure 7.1: Sketch of planar waveguide structure. n(z) is the refractive index profile where $n_2 < n_1 \leq 1$

n is assumed to be homogeneous and independent of the x- and y coordinate and can be written:

$$n(z) = \begin{cases} n_2 & \text{for } -\infty < z < 0 \\ n_1 & \text{for } 0 < z < d \\ n_2 & \text{for } -\infty < z < 0 \end{cases} \tag{7.10}$$

If we choose the coordinate system as shown in figure 7.1 the modes will propagate in the x direction. For the TE modes the propagating wave is polarized in the y-direction and have only three non-zero field components: E_y, H_x, H_z.

The solutions to be considered are plane electromagnetic waves which can be expressed as

$$\mathbf{E}_j = E_j(z)e^{i(\omega t - \beta z)} \qquad [j = x, y, z] \tag{7.11}$$

$$\mathbf{H}_j = H_j(z)e^{i(\omega t - \beta z)} \qquad [j = x, y, z] \tag{7.12}$$

where ω is the radian frequency, $\omega = 2\pi f$, f being the actual frequency and β is the propagation constant, identified as the projection, k_x, in the x direction of the wavevector, $\beta = n_1 k \cos(\alpha_i)$.

By applying Maxwell's equations, 7.1 and 7.2, on expression 7.11 and 7.12, set of equations for the non-zero field components will result, and by substituting the expressions for the H components, the problem of finding the TE modes is reduced to find solutions to the one dimensional differential equation(Helmholtz equation)[42, 54].

$$\frac{\partial E_y(z)}{\partial z^2} + [k_0^2 n^2(z) - \beta^2]E_y(z) = 0 \tag{7.13}$$

The TE modes of the waveguide are now found by solving equation 7.13 using the boundary condition, that the fields and the tangential fields must be continuous at the dielectric interfaces, z=0 and z=d. Further we want the modes to be confined in the guiding layer

$(0 < z < d)$ and hence the fields to decay outside this region. The confinement condition can be expressed by the requirement

$$n_2 k^2 \leq \beta^2 \leq n_1 k^2 \tag{7.14}$$

When this is fulfilled the fields would be exponentially decaying outside the guiding region. If β is outside the range, the fields will be oscillating. These solutions are called *radiation modes* and corresponds to a free travelling wave[54]. We will only consider solutions that are damped outside the core region.

Providing now the boundary conditions and equation 7.14is satisfied, the solutions to the wave equation 7.13 can be written in the form

$$E_y = \begin{cases} Ae^{\gamma z} & \text{for } -\infty < z < 0 \\ A\cos(\kappa z) + B\sin(\kappa z) & \text{for } 0 < z < d \\ Ce^{-\gamma(z-d)} & \text{for } -\infty < z < 0 \end{cases} \tag{7.15}$$

where the parameters κ and γ are defined by the following relations[42]:

$$\kappa = (k^2 n_1^2 - \beta^2)^{1/2} = n_1 k \sin(\alpha) \tag{7.16}$$

$$\gamma = (\beta^2 - k^2 n_2^2)^{1/2} = ((n_1^2 - n_2^2)k^2 - \kappa^2)^{1/2} \tag{7.17}$$

Using the boundary condition the parameters A, B and C can be found. If A is equal to one, the values for B and C are

$$B = \frac{\gamma}{\kappa} \tag{7.18}$$

$$C = \cos(\kappa d) + \frac{\gamma}{\kappa}\sin(\kappa d) \tag{7.19}$$

Finally the allowed values of κ(7.17), and hence β, has to be determined. This is done by differentiation of expression 7.15 and requirement of continuity at the two interfaces resulting in the following equation system results

$$\gamma A - \kappa B = 0 \tag{7.20}$$

$$(\gamma \cos(\kappa d) - \kappa \sin(\kappa d))A + (\kappa \cos(\kappa d) + \gamma \sin(\kappa d))B = 0 \tag{7.21}$$

The equation system has a solution only if the system determinant vanishes.

$$\gamma(\kappa \cos(\kappa d) + \gamma \sin(\kappa d)) - \kappa(\kappa \sin(\kappa d) - \gamma \cos(\kappa d)) = 0 \tag{7.22}$$

This is referred as the eigenvalue equation or the transcendental equation, and can be rewritten first as

$$\tan(\kappa d) = \frac{2\kappa\gamma}{\kappa^2 - \gamma^2} \tag{7.23}$$

and next by defining the dimensionless waveguide parameter $V = kd\sqrt{n_1^2 - n_2^2}$ and setting $x = \kappa d$ as

$$\tan(x) = \frac{2x\sqrt{V^2 - x^2}}{2x^2 - V^2} \tag{7.24}$$

The original problem of finding the TE modes for the waveguide is now reduced to solving the transcendental equation 7.24, which in practice is done with a numerical algorithm. In figure 7.2 is illustrated an example of a plot of the left and right side of the equation for a silicon(SiO_2)/air guide. Each point of intersection represent a solution to the transcendental equation. There is only a finite number of solutions, $x = x^i$, and for each of these x^i values corresponds a set of κ^i and β^i values, where $i = 0, 1, 2, ...$ denotes the excitation order of the corresponding electric field $E_{y,i}$.
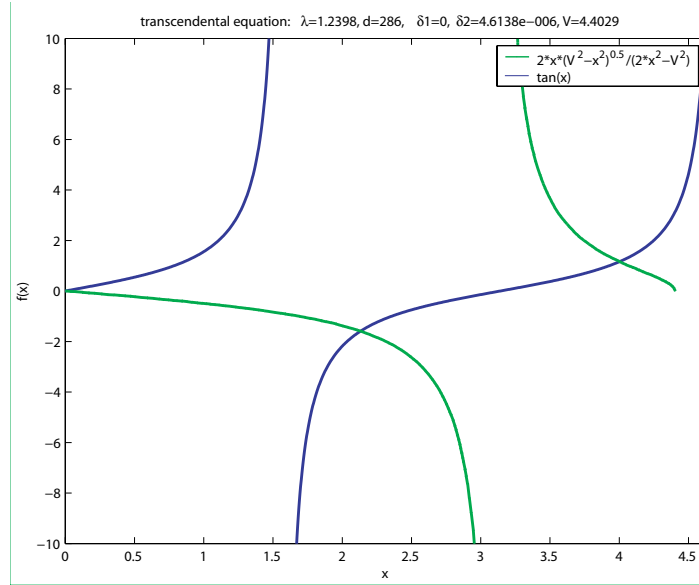
Figure 7.2: Left side (green) and right side (blue) of the transcendental equation 7.24 with the parameter of the 286 Å guide.

The transcendental equation for x has always at least one solution, which means that a symmetrical wave-guide has always at least one mode.

Solving the transcendental equation numerically or graphically one obtains x-values which are by the above given definitions related to incidence-angle values α_i:

$$\alpha_i = \arcsin(\frac{x}{n_1 kd}) \tag{7.25}$$

For the example plotted in figure 7.2 are the x values of the crossing points 2.131 and 4.002, and the corresponding angles (using expression 7.25) are 0.084° and 0.158°.

In summary we have derived the transcendental equation for a planar waveguide given by expression 7.24. By solving this equation for the actual waveguide to be investigated we can deduce mode number and corresponding incidence angles.

The electric field for the i'th mode is written :

$$E_{y,i}(z) = \begin{cases} e^{\gamma_i z} & \text{for } z < 0 \\ \cos(\kappa_i z) + \frac{\gamma_i}{\kappa_i} \sin(\kappa_i z) & \text{for } 0 < z < d \\ (\cos(\kappa_i d) + \frac{\gamma_i}{\kappa_i} \sin(\kappa_i d)) e^{\gamma_i(d-z)} & \text{for } d < z \end{cases} \qquad (7.26)$$

i.e., exponential decay outside the guide and a cosine and sine superposition inside the guide.

The absolute value of the electric field squared ($|E_{y,i}(z)|^2$) for the example of a 286 Å wave-guide is shown in figure 7.3. The second mode is exited at an angle of 0.158° which is already quite close to the critical angle for SiO2 at 10 keV of 0.174°. Therefore a larger part of the field intensity is outside the wave-guide in the walls, i.e., the mode is already close to become a leaky mode[42]. This will probably lead to an increased damping of this mode compared to the first one.
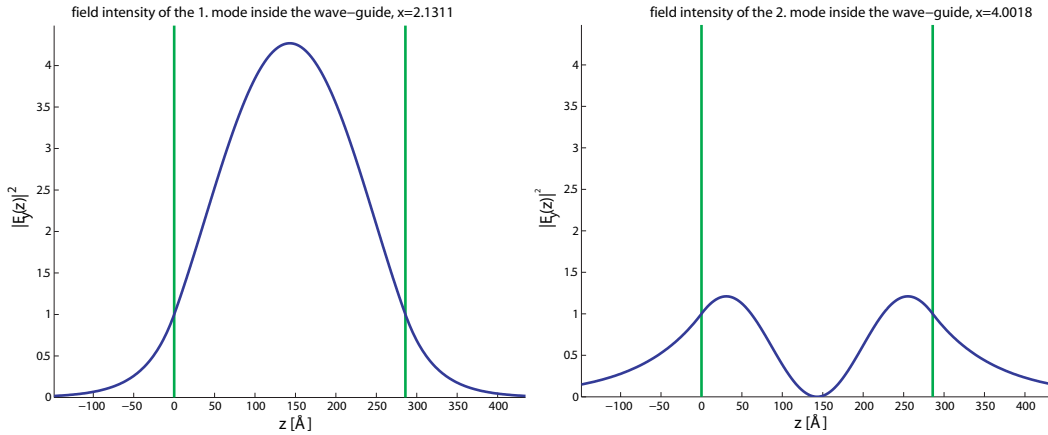
Figure 7.3: The squared, absolute value of the electric field inside the 286Å wave-guide of the first mode (left) and the second mode (right). The y-axis has in both cases the same (arbitrary) scaling.

The calculations shown here assume flat walls, but as will be shown later, roughness of the walls play a role and mode coupling can be expected.

7.2 Modes in rectangular waveguides

For the planar waveguide discussed in last section the waveguide effects only takes place in one dimension, while in the other dimension, the beam is defined by the x-ray source. In this section we will extend the theoretical considerations from the the planar guide to a two

dimensional guide structure. We will use the most simple two dimensional structure with a waveguiding core of refractive index n_1 embedded in a cladding with refractive index n_2 for the description.
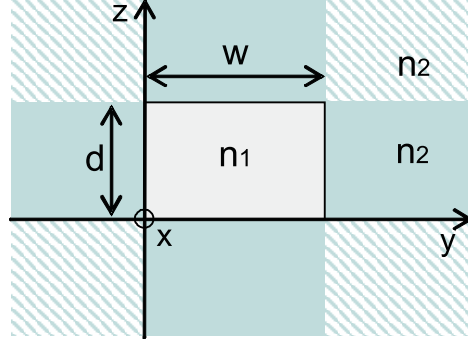
Figure 7.4: Front view of a rectangular x-ray waveguide with a guide core of width w and hight d and with refractive index n_1 embedded in a cladding layer with refractive index n_2

Figure 7.4 shows the geometry of the 2D structure. The corresponding refractive index profile is given by

$$n(y, x) = \begin{cases} n_1 & \text{for } 0 \leq y \leq w \wedge 0 \leq z \leq d \\ n_2 & \text{elsewhere} \end{cases} \tag{7.27}$$

The refractive index is now a function of two coordinates and as a consequence the description of the modes far more complicated. An exact analytical solution of Maxwell's equations is not possible, but approximate solutions by numerical methods have been obtained and can be made as accurate as desired [42]. The method is a good approximation for modes of low excitation orders, where the field is mainly confined within waveguide core region, and only a little field energy leaks into the cladding material. In particular there is very little field energy in the shaded regions of figure 7.4 and the analyze can be simplified by ignoring these regions completely. Given this assumption the Maxwell equations can again be solved using the plane harmonic fields

$$\mathbf{E}_j = E_j(z)e^{i(\omega t - \beta z)} \qquad [j = x, y, z] \tag{7.28}$$

$$\mathbf{H}_j = H_j(z)e^{i(\omega t - \beta z)} \qquad [j = x, y, z] \tag{7.29}$$

Similar to the one-dimensional case described in the previous section, the solutions to Maxwells equations can be classified into predominantly y-polarized and z-polarized modes. The two dimensional wave equation, analogue to 7.13 can be written

$$\frac{\partial^2 \psi(y, z)}{\partial y^2} + \frac{\partial^2 \psi(y, z)}{\partial z^2} + [k^2 n^2(y, z) - \beta^2]\psi(y, z) = 0 \tag{7.30}$$

Where $\psi(y,z)$ denotes $E_y(y,z)$. As before the the field has to be confined within the core region leading to the expression

$$n_2 k^2 \leq \beta^2 \leq n_1 k^2 \tag{7.31}$$

and the fields within the five regions, inside the core, and the four regions surrounding the core, see figure 7.4 is given by [54]

$$\psi_1 = (i/\kappa_z\beta)(n_1^2 k^2 - \kappa_z^2)cos[\kappa_y(y+\eta)]\sin[\kappa_z(z-\zeta)] \tag{7.32}$$

for $0 \leq y \leq w \wedge 0 \leq z \leq d$

$$\psi_2 = -i[(\gamma_z^2 + n_2^2 k^2)/\gamma_z\beta]\cos[\kappa_y(y+\eta)]\cos[\kappa_z(d-\zeta)]\exp[-\gamma_z(z-d)] \tag{7.33}$$

for $0 \leq y \leq w \wedge -\infty < z < 0$

$$\psi_3 = i[(\gamma_z^2 + n_2^2 k^2)/\gamma_z\beta]\cos[\kappa_y(y+\eta)]\cos(\kappa_z\zeta)\exp(\gamma_z z) \tag{7.34}$$

for $0 \leq y \leq w \wedge d < z < \infty$

$$\psi_4 = i(n_1^2/n_2^2)[(n_2^2 k^2 - \kappa_z^2)/\kappa_z\beta]cos[\kappa_y(w+\eta)]\exp[-\gamma_y(y-w)]\sin[\kappa_z(z-\zeta)] \tag{7.35}$$

for $w < y < \infty \wedge 0 \leq z \leq d$

$$\psi_5 = i(n_1^2/n_2^2)[(n_2^2 k^2 - \kappa_z^2)/\kappa_z\beta]cos(\kappa_y\eta)\sin[\kappa_z(z-\zeta)]\exp(\gamma_y y) \tag{7.36}$$

for $-\infty < y < 0 \wedge 0 \leq z \leq d$

η and ζ being phase parameters, making the solution general and with the following relations for $\kappa_y, \kappa_z, \gamma_y, \gamma_z, \eta_y, \eta_z$ and β[42]

$$\gamma_y^2 = (n_1^2 - n_2^2)k^2 - \kappa_y^2 \tag{7.37}$$

$$\gamma_z^2 = (n_1^2 - n_2^2)k^2 - \kappa_z^2 \tag{7.38}$$

$$\tan(\kappa_y\eta_y) = -\gamma_y/\kappa_y \tag{7.39}$$

$$\tan(\kappa_z\eta_z) = -(n_2^2/n_1^2)/(\kappa_z/\gamma_z) \tag{7.40}$$

$$n_1^2 k^2 + \beta^2 = \kappa_y^2 + \kappa_z^2 \tag{7.41}$$

As in the planar waveguide section, the boundary conditions that the fields must be continuous at the interfaces must be satisfied. This results in two sets of uncoupled transcendental equations, giving the allowed discrete values of κ_y and κ_z

For κ_z we have

$$\tan \xi_z = \frac{2\xi_z \sqrt{(\tilde{V}_z^2 - \xi_z^2)}}{2\xi_z^2 - \tilde{V}_z^2} \tag{7.42}$$

$\tilde{V}_z$ again being a dimensionless wave parameter

$$\tilde{V}_z := kd\sqrt{n_1^2 - n_2^2} \tag{7.43}$$

and

$$\xi_z := \frac{d}{2}\sqrt{k^2 n_1^2 - \beta^2} \tag{7.44}$$

and κ_z

$$\kappa_z = \frac{\xi_z}{d} \tag{7.45}$$

For κ_y the corresponding expressions are

$$\tan \xi_y = \frac{2n_1^2 n_2^2 \xi_y \sqrt{(\tilde{V}_y^2 - \xi_y^2)}}{n_2^4 2\xi_y^2 - n_1^4(\tilde{V}_y^2 - \xi_y^2)} \tag{7.46}$$

$$\tilde{V}_y := kw\sqrt{n_1^2 - n_2^2} \tag{7.47}$$

and

$$\xi_y := \frac{w}{2}\sqrt{k^2 n_1^2 - \beta^2} \tag{7.48}$$

and κ_y

$$\kappa_y = \frac{\xi_y}{w} \tag{7.49}$$

As for the planar waveguide the two transcendental equations 7.42 and 7.46 can be solved by plotting left and right side of the equations. The finite points of intersection gives a set of (ξ_y, ξ_z) and thus (κ_y, κ_z) values corresponding to the modes propagating in the guide. Each mode, ψ^{pq} is attributed to the (pth,qth) exitations order in the (y,z) direction with the corresponding values for (ξ_y^p, ξ_z^q), (κ_y^p, κ_z^q) and β^{pq}.

For each mode, the two angular values are given by[54]

$$\tan \phi_{int}^p = \frac{\kappa_y^p}{\beta} \tag{7.50}$$

and

$$\tan \alpha_{int}^p = \frac{\kappa_z^q}{\beta} \tag{7.51}$$

7.3   Intensity in the far-field region

The electric field at a height z at the wave-guide exit is known from equation 7.15, and the next to determine is the intensity at a point P far away from the wave-guide. The angle between the wave-guide axis and a line from the wave-guide exit to this point is called the exit angle α_f. For describing the far-field intensity we use the far-field approximation which is valid for distances significantly larger than the wave-guide opening and the wave-length. Within the approximation it is assumed that beams emitted from two neighboring points at z and $z + \Delta z$ that interfere far away at the point P are parallel[53]. Therefore the path-length difference $\delta_L(\alpha_f)$ between the distance from the point at z to P and the one from $z + \Delta z$ to P is simply $\delta_L(\alpha_f) = \sin(\alpha_f)\Delta z$. Integrating the known electric field, $\psi^q(z)(\mathrm{E}_{y,i})$, q is the mode number, with the correct phase factor $\exp(ik\delta_L(\alpha_f))$ across the wave-guide exit gives the far-field at a certain point P described by α_f. The intensity is proportional to the absolute value of the far-field squared.

$$I^q(\alpha_f) = I_0 | \int_{-\infty}^{\infty} \psi^q(z) \exp^{ik\alpha_f z} dz |^2 \tag{7.52}$$

In the expression the small angle approximation, $\sin x \simeq x$ has been used.

For the $286\mathring{A}$ wave-guide the far-field for the first and second mode is shown in Fig. 7.5 (the two small blue curves) as well as the sum of these two intensities (small green curve). To relate these intensities to the measured data the intensities have to be convoluted with a box function corresponding to the used 0.5 mm detector slit, which is shown with arbitrary intensity in cyan. Convoluting the intensity of the first mode with the detector box-function (of height 1) results in the large blue curve. Convoluting the sum of the first and the second mode with the detector box-function results in the large green curve. For comparison with the measured detector scans with a width of 0.132 a Gaussian of this width is plotted in magenta with the same peak-value as the calculated curve. These two curves closely resemble
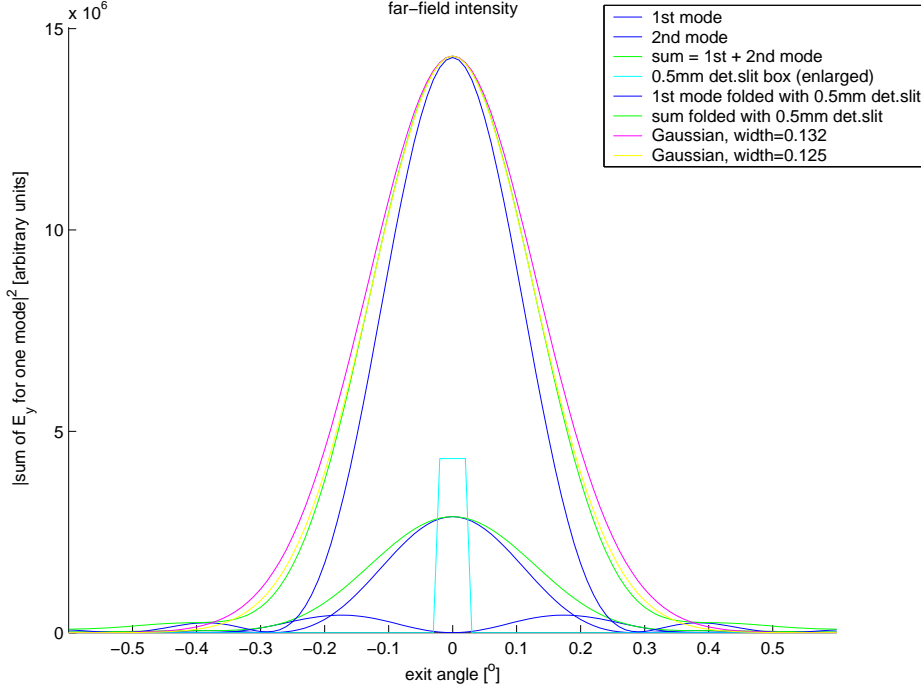
Figure 7.5: Calculated far-field intensity for 286Å guide. The first and second mode (small blue curves) and their sum (small green curve) are plotted. Further the detector box-function (cyan, arbitrary height) and the first-mode intensity (large blue curve) and summed intensity (large green curve) convoluted with this box function are illustrated. Gaussian peaks of the same height with 0.132 FWHM (magenta) and 0.125 FWHM (yellow)[12].

each other. Differences may be related, e.g., to the not precisely known detector-to-sample distance and other uncertainties.

7.3.1 Farfield intensities for a rectangular waveguide

The electric field for the rectangular waveguide depends both on the y and z coordinates. This means that the far-field diffraction integral is no longer reduced to a simple one dimensional integration as given by 7.53. For the case of a rectangular guide the intensity distribution is described by[54]

$$I^{pq}(\phi_f, \alpha_f) = I_0 | \int_{-\infty}^{\infty} \psi^{pq}(y, z) \exp^{ik(\phi_f y + \alpha_f z)} dy dz |^2 \tag{7.53}$$

For obtaining a detailed description of the far-field intensity patterns, we first solve the transcendental equations 7.42 and 7.46. For each mode $\psi^{pq}(y, z)$ we then have the calculated values of $\kappa_z, \kappa_y, \phi_{int}, \alpha_{int}$ and using equation 7.53 the expected field intensity distributions can be examined.

7.4   Coupling of intensity into the guide

There are different ways to couple intensity into the wave-guide. In this section we will shortly discuss different coupling methods and their feasibility of application to x-rays with wavelengths $\lambda \approx 0.1nm$.

1. **Directly through the front opening.**

   This is the obvious way and is well known from the optical wave guides(OWG) designed for visible light. In an optical systems the light source, the laser, is coupled directly through one end of the Waveguide(WG) and adapted in such a way that the output matches the characteristics of the WG allowing for efficient coupling. This works quiet well for systems where the source size matches the dimension of the guide material, which is indeed the situation for OWG with laser spots and optic cores both having μm dimensions. This is not the case for X-ray waveguides(XWG) where the core dimensions typically is in the nm range and the beam size usually in the mm range. The incidence angles are always small and therefore the intensity coupled into the guide in this way, is proportional to the opening area. This means when hitting the front of the XWG the intensity losses will be huge and the coupling efficiency very poor. Furthermore, for the guides made within this project, the opening on the incident and exit side of the guide may be closed by Si dust, due to the cutting of the samples with a diamond saw. This may slightly decrease the transmitted intensity, but as long as these grains are like walls, i.e., as long as the beam is almost perpendicular to the grain surface is refraction at these dust particles not a problem.

   Due to the relative large intensity lost when coupling into the guide from the front, we also made a front coupler a plateau in front of the guide in order to increase the intensity output of the beam actually going into the guide. The idea is illustrated in figure 7.6
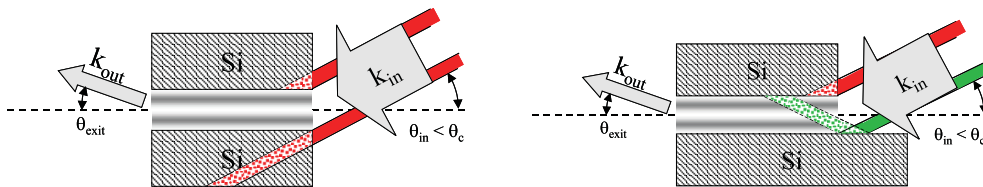
Figure 7.6: Left: Relatively much intensity is lost since it is not hitting the entrance of the guide. Right: Modified structure with a plateau in front of the guide raising the amount of the beam entering the guide

   In this way more of the x-ray beam is led into the guide. The actual fabrication only has to be slightly modified and in principle it should not be a problem to bond silicon pieces of different size instead of hole wafers. The details about the fabrication and the results of the test measurements for waveguide with front coupler are described in next chapter.

2. **Thin silicon topwafer used as a Reconant Beam Coupler(RBC)system**

   Another possibility is to use a Resonant Beam Coupler(RBC)system, which is known from other studies, to be an efficient way of coupling. For our guides this can be realized by bonding of a very thin silicon wafer on the top and couple through the thin silicon film, and as the the top wafer is thinned down, the absorption is very low. The principle of the x-ray RBC is similar to that of an optical prism couples. The principle of a RBC coupler is illustrated in figure 7.7 below.
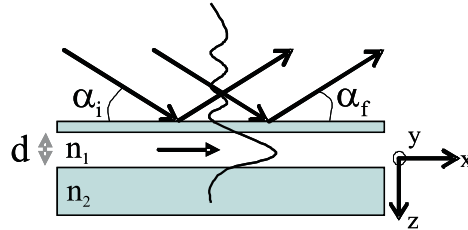
Figure 7.7: Sketch of a RBC Coupler.

The thickness of the top cladding layer is reduced to a thin film with a typical thickness of 1nm-50nm. A broad x-ray beam impinging with an angel α_i below the critical angle α_c will not only be specular reflected but also partly transmitted creating an evanesces wave below the interface. This evanescens wave can resonantly excite a guided mode provided that the right conditions for wave guiding regarding layer thickness, refractive index and incidence angles are full filled. The field will then propagate along the x-axis and exit the WG structure with a well defined amplitude and phase distribution. Using the RBC couplings scheme it is actually possible to enhance the flux intensity by several orders of magnitude relative to the incoming beam. The Resonant coupling principle can easily be measured by reflectivity measurements. By varying the incident angle, dips in the reflectivity curve can be seen, which are exactly mapping the guide mode of the specific waveguide. Examples of these characteristics can be found in[26, 54]. We have only tested the RBC coupling in a single measurement due to time limitation.

3. **Front coupling combined with a prefocusing mirror system[37]**

   As mentioned earlier the efficiency of coupling intensity into the guide from the front is rather poor. If we further consider two dimensional guides with both nm dimension in width and height the amount of vasted beam is even larger. This problem can be accomplished by using a combined system with a prefocusing mirror in front of the guide and has been demonstrated for both planar waveguides[28] and recently also for a two-dimensional confining x-ray channel[37]. The mirror system was a Kirkpatrick-Baez mirror system, and in the setup the total flux of the waveguide beam was increased significantly leading to a very small and well defined coherent beam with high flux and high signal to noise ratio. It is believe that the system can be even further improved by using higher demagnification for the KB optics, resulting in an even smaller cross section.

The optics could easily be incorporated into our system. We have not tested the combined setup, but it is believed to be a good choice for raising the efficiency of our guides.

7.4.1   Gain

For many applications a high flux at the waveguide exit is important. The flux is defined as the number of photons per second per unit area. Using the RBC couplings scheme would provide an intrinsic increase in flux density and thus also a resonant enhanced flux of the exiting mode with respect to the incident beam, whereas for the standard front coupled guides the total flux rate would be lower. The gain value is characterizing the flux performance of the guide and is defined by the ratio

$$\mathcal{G} = \frac{\mathcal{F}_{out}}{\mathcal{F}_{in}} \tag{7.54}$$

where $\mathcal{F}_{out}$ is the integrated exiting flux and $\mathcal{F}_{in}$ is the flux of the primary beam which is coupled into the device[54]. Experientially we can measure the transmission T for the object as the ratio between the photon flux F' at the exit of the waveguide and the incident photon flux F. Knowing the vertical and horizontal dimensions of the incident beam, S and H and the FWHM size S' of the exiting beam we can write the experimental deduced gain [35] as

$$G = \frac{I_{out}}{I_{in}} = \frac{TF/S'H}{F/SH} \tag{7.55}$$

As can be seen in the expression a higher transmission will result in higher gain values, whereas the choice of the guiding core material is important. The material absorbtion has been discussed already by Spiller et al [66] for the early waveguide production. A further discussion of the transmission in a thin-film waveguide can be found in [36] where it is found that the experientially transmission efficiency ($T_{experimet}/T_{cal}$) in state of the art one- and two dimensional waveguides is ap. 50%.

Typical theoretical x-ray RBC have gain values for the zero mode excitation in the range between $10 < \mathcal{G} < 200$[54]. For two dimensional(2D) waveguide structures made by ebeam lithography tested in the RBC scheme [55] is reported a 70 fold gain in flux. This is still to poor for most application, but is expected to be higher with improved fabrication techniques. Latest results on 2D guides using front coupling combined with a prefocussing mirror system as described in the earlier section will increase the total

flux, and for these combined systems very high gain values of $G \simeq 4000$ are reported.

The calculated maximum theoretical gain derived in the limit of infinitely sharp and flat interfaces for a perfect waveguide is not always in agreement with actual measurements. For a real device several effects can reduce the efficiency.

- **Interface quality and layer inhomogeneity**

  These are important factors which may reduce the gain of the device. The real waveguide devices are never perfect as assumed in the theoretical considerations. Often they have index inhomogeneity and slight changes in core widths, which cause the modes of the waveguide to couple among each other. This means for even when a pure excited mode at the entrance of the guide, some of the mode may be transferred to other guided modes and to radiation modes[42]. Mode mixing to other modes will results in signal distortion and transfers to radiation modes will results in waveguide losses since power is carried away from the core region into the cladding.

  Feng et al[25] have been investigated mode mixing in x-ray thin-film waveguides with a 4-6Åinterfacial roughness based on coupled power theory for optical waveguides[42]. They attribute the origin of the mode mixing to x-ray diffuse scattering from rough interfaces. The waveguide in this project have roughness between 5-20ÅRMS values (measured by AFM). For the non etched top wafer used for closing the waveguides is the RMS roughness value below 5Å, which is standard for polished wafers at the laboratory. For the etched wafers the RMS roughness where typically slightly raised and showed RMS up till 20Åfor the bottom of the guides. The roughness of the sidewall is expected to be relatively high depending of the choice of etching process.

- **Angular acceptance**

  Even for third generation synchrotron sources with high x-ray brilliance the diverges is not negligible. This means that the measured efficiencies are diminished compared to the calculations, where an ideal plane wave were assumed. For the front coupled system FCW, the angular acceptance is in the range of some hundreds of degrees while for the RBC-XWG it is only in the range of a few thousands degrees. Using a combined system as described previously the high value of angular acceptance for FCW matches the presently most efficient x-ray optics focusing and there by it is actual possible to obtain well defined intense nanobeams using such systems [37]. For the RBC couplings scheme the effect from the angular acceptance can partly be compensated by adjusting the top layer thickness [54].

- **Absorbtion**

  The absorbtion is also an important effect. Absorbtion in the materials implies that the beam is attenuated with a characteristic 1/e length which is denoted μ^{-1}, where μ is the absorbtion coefficient(The absorbtion length refers to the intensity attenuation). The absorbtion is formally equivalent to the imaginary part, b, of

the refractive index (7.7). The absorbtion is strongly dependent of the x-ray energy. The effect is strong for small x-ray energies and can be minimized by using hard x-rays with wavelength $\lambda < 0.15$nm. Unfortunately this also effects the excitations angles, which then become smaller.

- **Coherence**

  Finally the coherence of the incoming beam can also affect the wave guiding. The degree of coherence is expressed as a length scale over which the wavefronts can be considered to be efficiently a monochromatic plane wave. There are two length to be considered, the transverse coherence length $\mathcal{L}_T$ and the longitudinal coherence length $\mathcal{L}_L$ [2]. If the transverse coherence length of primary beam is not sufficiently high this affects the efficiency of the coupling. In the RBC coupling systems the coupling effect relies on the transverse coherence length, and it is a problem if the coherence length in one of the dimensions is in the same range as the accepted beam width. The longitudinal coherence length for the used x-ray source is in general low, and due to small values of internal propagation angles and the relatively thin guiding layer the differences in the total path length of the internally propagating x-rays are much smaller than the coherence length.

Chapter 8

Fabrication and characterization

The waveguide fabrication consists of two main steps. The etching of the channels on one wafer and the hydrophobic wafer bonding to a standard wafer closing the channels. The success of the wafer bonding is very sensitive to the handling of the wafers before bonding and therefore the etching process has to be carried out very carefully. Small particles or chemical contamination will results in voids or weak bond strengths and in the worst case, the waveguide may fall apart. For the etching of the channels it is also important that the shape and roughness are of high quality if the x-ray beam should be reflected from the surfaces inside the channel.

In this section there will be a presentation and discussion on the preparation of the guides. The critical parameters will be discussed in details ending up with a complete process recipe. First a short introduction to the basis concept of direct hydrophobic waferbonding is given, and some extra considerations due to the bonding of the structured wafers. After that we will focus on the lithograph process, transferring the wanted structures to the wafer and the subsequently etching process. The chapter ends with a description of characterizations performed for evaluating the quality of the guides.

8.1 Waferbonding techniques

8.1.1 Hydrophobic waferbonding

The type of wafer bonding used to fabricate the cavities was hydrophobic fusion bonding annealed to 1000 degrees.

In the fusion wafer bonding process the two wafer are placed on top at each other and carefully pressed together in a single point. The process is carried out at room temperature after cleaning the surfaces chemically. The two wafers are pressed together in a single point, where physical contact is made and the bonding will subsequently spread from this point as a wave all over the wafer. The process only take a few seconds

and to be sure that the wafers are extremely well bonded, the bonded wafer pair is annealed at high temperature. The annealing of structured bonded wafers may be a problem sometimes damaging the structures, but can also be a benefit since voids with trapped air or other specimens will more easy tend to diffuse to the structured areas and strengthen the bonding. For the wave guides made in this project there was no problems were observed related to the annealing , and they have all been annealed at 1000 degrees for 30 min. IR pictures before and after annealing shows that voids visible at room temperature are disappearing during the heating resulting in better bonding.

The direct bonding at room temperature is due to interactions between the two surfaces brought in contact. For obtaining an hydrophobic surface, the wafer is rinsed in HF immediately before the bonding. When making the waveguides, the one wafer has be through a series of process step for etching the channels, and at the end the surface is covered with thermal grown oxide of app. 1000Å. This is removed in a buffer solution of HF. The other wafer is typically a standard polished wafer, which is cleaned from the producers and sealed when arriving in the cleanroom. This wafers are clean but hydrophilic due to reactions with the surroundings, where water reacts and creates Si-OH bonds. This native oxide layer is 1-2 nm thick and can be removed by a short HF clean in 30s. The hydrophobic surface is covered by hydrogen and fluorine bonds and the surface is very reactive and the bonding should be carried out immediately after the HF rinse.

When the oxides are removed in HF, it is important not to over etch, since the HF have a small tendency to enhance the micro roughness of the silicon surface. A increased roughness for the wafers to be bonded is crucial, since good contact between the surfaces are necessary. Second, an increased roughness affect the guiding properties of the waveguide.

8.1.2   Bonding of structured wafers

When bonding silicon wafers at room temperature each wafer is elastically deformed to achieve conformity of the two surfaces, and if the wafers are not sufficiently flat, unbonded areas results. If a gap caused by non-uniform flatness is present between wafers, the condition for gap closing depends on the lateral extension, R, of the gap, and the wafer thickness, t_w. When bonding structured wafers the situation can be regarded as equivalent to bonding of wafers with high surface flatness variations. This means, that the equations describing the conditions for gap closing regarding voids due to surface variations can be used as guidelines for the design of pattern dimensions to avoid closing the structures.

For the situation where two identical wafers is bonded and $R > 2t_w$ is the condition for avoiding gap closing given by [70]

$$h > \frac{R^2}{\sqrt{\frac{2}{3}Et_w^3/\gamma}} \tag{8.1}$$

h is the gap height, E Youngs modulus[41], and gamma the surface energy of the bonding. For the opposite situation, $R < 2t_w$, the expression is independent of t_w and given by [70]

$$h > 3.5(R\gamma/E)^{1/2} \tag{8.2}$$

The cavities are fabricated by bonding structured wafers to standard silicon wafers and for predicting whether the unstructured wafer on top of the cavities will bond to the bottom of the cavity, we can use the above considerations as guidelines. The dimensions used for the cavities are highly asymmetric with lengths up to several centimeters and narrow widths from 1.5 to 100 microns for the one dimensional guides and 100-200 nm for the 2D guides. The depth is from 20-100 nm. If we insert typically values for our guides in expression 8.1 and 8.2, we would expect the cavities to be unstable with a high probability of closing, especially for the cavities with the largest width and smallest depth. This is not observed, and can probably be assigned to very asymmetric design[58]. For the guides made with a very thin top wafer bonded to structured wafers the equations has to be modified[70] and the probability for collapsing is even higher, since thin wafers are more easily deformed.

The bonded wafers are typically annealed at very high temperatures and during this process, gasses inside the cavities can affect the structure and strength of the bonding and damage the cavities. When annealing several possible reaction can take place:

(1) Reactions between the trapped gas and the silicon inside the cavity.

(2) Part of the gas may escape from the cavity as the wafer is heated up.

(3) The contaminants on the surfaces of the bonded wafers may desorb.

(4) A plastic deformation may occur if the differential between the pressure in the cavities and the outside pressure increases beyond the yield point of silicon at that temperature.

The deflection of the silicon surface above the cavities has not been measured. It is reported from others, that for sealed cavities bonded from silicon in air, annealed at 1000 degrees and subsequently cooled to room temperature, it is expected that the silicon layer over the cavities is deflected into the cavities. In the annealing process oxygen within the sealed cavities reacts with the silicon and forms SiO_2, and the pressure is expected to drop from 1 to ap. 0.8 atmosphere. Experimentally this is not always the case. One possibility for that is that the wafers are debonded during the annealing. If debonding occurs the residual pressure will be smaller than expected. The size of the cavity affects the possibility of debonding. For a typical 500μm 4 inch. silicon wafer,

cavities limited in size below 3 mm. in diam will not tend to debond as the pressure below 1200 degrees is not sufficient high to open cavities bonded with a surface energy of 80 mj/m^2 or more[70]. This is typical the value for room temperature bonding. For thin top wafer the situation is different and the risk for either cracking the the silicon on top of the cavities and debonding large areas a quite large.

The cavity gas pressure is strongly depended on the bonded area surrounding the cavities. Test experiments shows that for the situation of a low density of cavities on a wafer, (corresponding to larger bonding area around each cavity) a higher increase in pressure inside the cavity is observed, thereby increasing the possibility of debonding. On the other hand a very high density of cavities will lower the pressure increase in the cavities, but then the contact area needed for initiate the bonding is reduced. These considerations must be kept in mind when designing the structures.

It is necessary to heat op the bonded wafers to sufficient high temperatures above 1000 degrees, both for raising the bond strength, but also in order to avoid small interface bubbles. This is a general known problem within wafer bonding processes. Since the annealing not seems to be aproblem for the stability of the guides, we decided to heat all samples to 1000 degrees in 30 min. IR inspection after the heating show no small heat related interface bubbles. Comparison of IR pictures before and after annealing in fact showed that the heating had a positive influence on the voids visible at the room temperature bonding, often were remarkable reduced or total disappeared.

During the annealing process oxygen within the sealed cavities reacts with the silicon and forms a SiO_2 layer at the interfaces. This has to be kept in mind when calculating the x-ray reflections from inside the cavities. Furthermore we are cutting the guides in desired lengths from one to several mm. and thereby opening the cavities. As a result trapped gasses and other spices from inside will then have the possibility diffuse out.

More details and examples of bonding of structured wafers can be found in reference [70, 6, 17, 39]

8.2 Lithography processes for fabricating the one dimensional guides

The cavities on the structured wafer are fabricated using standard UV-lithography or e-beam lithography. For UV-lithography using a standard type of mask, the resolution limit in width is 1.5 μm. 1.5 μm is far to much for obtaining guiding in this(horizontal) direction, but the depth of the guide can be controlled down to a few nm and guiding in this direction(vertical) is possible. For making two dimensional guides, e-beam lithography is needed. With this equipment lines with widths typically of 100-200 nm were fabricated. The standard UV-lithography process is very easy to access and relative

inexpensive to run, and the process can be carried out at DANCHIP. Fabricating one dimensional guides and learning about the quality of the guides and the modes was the first step in the project. The e-beam writer was not always easy to access and the first samples were fabricated at MC2, Chalmers, Goteborg. The e-beam writer has to be run by specially trained people, and the cost price for making one structured wafer using the e-beam is several thousand kroner.

In the next sections we will go through the different process step used for making the cavities.

8.2.1   UV-lithography

The first was to fabricate a mask for the waveguide pattern that we wanted to make. We made a mask of seven different arrays with widths varying from $1.5\mu m$ to $100\mu m$ and always with double line width spacing. For $1.5\mu m$ lines the spacing is $3\mu m$, for $3\mu m$ lines the spacing is $6\mu m$ etc. The mask design is illustrated in figure 8.1.
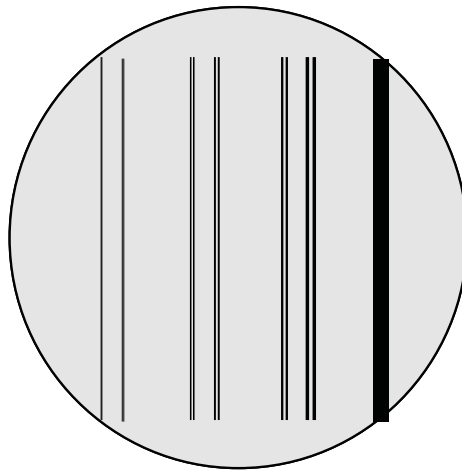

Figure 8.1: Mask design for 1D guides. Each black line consists of an array of ten equally lines.

Then we needed to consider, which kind of etching gives the best result. It is important that the roughness in bottom of the cavity after the etching is relatively low, in order to not influence the quality of the reflected x-ray beam to much. Further it must be considered that the etching gives nice sidewall. This is not crucial for the one dimensional guides, but critical when making 2D guides, where reflections also are made from the sides.

We have been working with several different process for making the cavities. Testing the shape of the etched structures, the roughness effect and how easy the etch can be controlled when very precise cavity depths are wanted. We ended up choosing the

Reactive Ion Etch(RIE) process which fulfilled mostly of the demands listed above.

For the fabrication we always used 4 inch double sided polished 350 μm (100)wafers. They were all p-doped and had same low resistivity. Typically the roughness is below 5Å. All the process steps in the fabrication were carried out in cleanroom facilities at DANCHIP. Before the photo sensitive resist layer was spined on, we grew a layer of thermal oxide. This was found to be necessary due to very poor bonding if the resist was added directly at the surface. Typically huge voids were present, and for some wafers it was not possible at all to get the two surfaces in appropriate contact. The problem could be connected to the wet chemicals used to remove the resist prior to the bonding. Further it was beneficial that the oxide then could be used as etching mask, thereby minimizing the amount of wet chemical used to remove the resist layer directly into the cavities.

The thermal process used was a dry oxidation process[41]. The oxidation temperature was set in the range of 1000-1100 degrees, and the process time was a few hours depending on the wanted thickness of the grown oxide. Prior to the oxidation the wafers were cleaned in a RCA-clean.

Before spinning the photo resist, the wafers were heated in order to make the sticking of the resist better. The thickness of the resist were 1.5μm. The wafers are exposed in a negative process. The quality of the lithography was found to be very sensitive to time and humidity. 1.5μm lines are close to the resolution limit for the UV-lithography and if the humidity changes, the exposure time necessary for making nice well defined structures are affected. After several test the best suited exposure time were found, using a first exposure time of 25 sec through the mask followed by a flot exposure of 3 sec. The wafer were afterwards developed and the quality of the pattern inspected by an optical microscope.

When using the RIE system to etch the channels, it is necessary to have good control of the etch rate for the involved materials. Standard recipes made for oxide and silicon etch were used as basic recipes [41]. The etch rate and selectivity values have to be correct, matching the structures specific for the samples. The rates are very area sensitive, and are expected to be opposite proportional to the area. The parameters for the two recipes used are listed in table 8.1. The etch rate was found running the processes on test wafers and measure the depth of the cavities with a tencor profilometre. For the oxide, we found typically values around 190$\mathring{A}$/min which is 45 percent lower that expect from the listed standard values. For the silicon, the values was found to be app. 70 Å/sec corresponding 4200 Å/min which is close to the expected values of 4000 Å/min. For very short process times, below 8 seconds, the rate have a small tendency to slow down to 55 $\mathring{A}$/sec.

The thickness of the oxide was 200-250 nm and for etching through to the silicon, the oxide was etched for 14 min. The selectivity to silicon is 7:1, and a small over etch

	Oxide etch	Silicon etch
CHF_3	26sccm	32sccm
CF_4	14sccm	-
O_2	-	8sccm
Pressure	100mTorr	80mTorr
Power	60W	30W
Etch rate$_{ox}$	350 Å/min	100 Å/min
Etch rate$_{resist}$	180 Å/min	400 Å/min
Etch rate$_{si}$	50 Å/min	4000 Å/min
Selectivity Res : Ox		
Selectivity Ox : Si		

Table 8.1: RIE ecth parameters

will not have huge effect in the silicon. After transferring the pattern to the oxide, the resist was remove in Ultra sound + acetone, and to be sure that the resist is totally remove the wafers were treated in an plasma system.

The final etch into the silicon can now be made. We chose to make several wafers with depths from $400\mathring{A}$ to $5000\mathring{A}$. The depth were estimated using the results from the etch rate tests. The expected depths were later compared to values measured in x-ray reflectivity scans.

In between the etching and chemical treatments for removing the oxide, the wafers were inspected in the microscope. The cavities are now ready to be closed by bonding. The oxide layer remaining is removed in a HF solution. The standard wafers that were used as top wafers were made hydrophobic in HF and immediately after, they are bonded at room temperature. To check if there is good contact between the surfaces, the bonded wafers were carefully inspected by IR camera. The strength of the bonding is low, but good enough to withstand some handling. If the bonding results is acceptable the wafers are transferred to the anneal oven and heated for 30 min at 1000 degrees. Comparing the IR pictures before and after annealing clearly shows that the annealing process improve the bonding. The guides were brought out of the cleanroom and diced in desired length with a diamond saw. An overview of the process steps can be found in appendix A.

The one dimensional guide structures has also be made with bonding half a structured wafer to a hole wafer. The process were almost identical, with the small change that before removing the oxide in the HF , the cavity wafer was mechanically broke in to half and each half were bonded to one hole wafer. The purpose was to create a plateau in front of the guide, that could increase the intensity coupling into the guide. The bonding of half wafers where done without any problems.
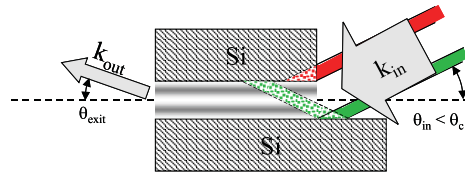
Figure 8.2: Schematic draw of waveguide made with plateau in front.

This was done since, part of the beam were not hitting the front of the guide and thereby lost. The construction of an plateau in front, illustrated in figure 8.2, was thought to overcome some of this problem, rasing the intensity of the guides. The bonding of half wafers where done without any huge problems.

The one dimensional structures have also been made by bonding a thin (500Å) wafer on top of the etched cavities.

This was to done to test if intensities could be coupled into the guide using through the thin topwafer (Resonant beam coupling) The steps for making such samples are identical to the earlier description only with the change that a thin SOI wafer is bonded on top instead of a standard wafer. After the bonding and annealing, the backside handle wafer and the oxide box layer of the SOI is removed in KOH and HF.

It was possible to bond such thin wafers, but as the top wafer thickness was only ap. 500Å, the guides were very mechanical unstable. Further the probability of collapsing is increased since the top wafer more easily is deflected into the cavity. Optical microscope pictures clearly shows that for many of the one dimensional structures the thin top were broke or collapsed. Microscope pictures is found in the characterization section.

8.3   E-beam lithography processes for fabricating two dimensional WG

With the e-beam equipment it is possible to fabricate guides narrow enough to obtain guiding in two directions. The width of the e-beam is tunable and can be adjusted to the wanted size. We have been making channels with to different widths, 100nm and 200nm.

8.3.1   e-beam process steps

The pattern design for the e-beam is illustrated in figure 8.3. The design was made so that both a single guide, interference between two guide and interference between an

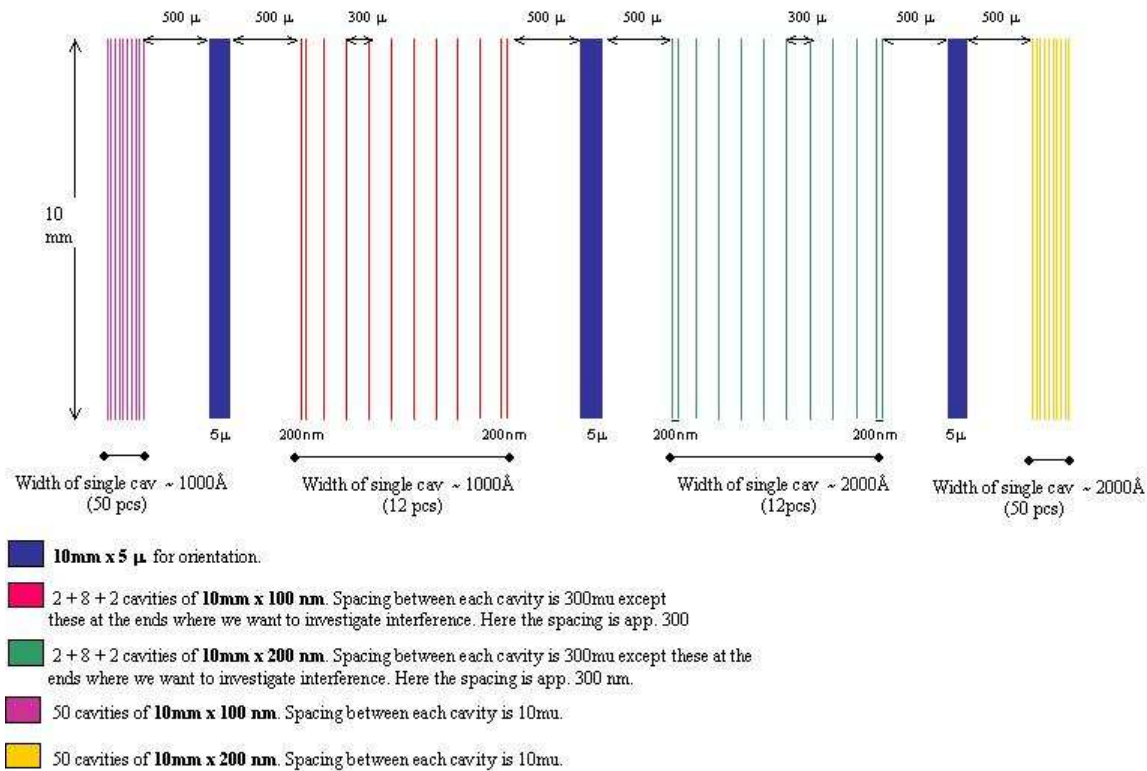array of 50 identical equally spaced guide could be investigated.

Figure 8.3: Mask pattern used for the e-beam

The 5μm channels were put into the design for helping finding the structures later. Further they were used to measure the depth of the etching since the tip of the tencor is to broad to go into the nm channels.

The used resist is a PMMA resist, with a thickness of app. 100nm. The thickness is small compared to the photo resist, which means that the process steps used for the UV lithography fabricated guides has to be modified before using it for the e-beam. The selectivity in the RIE etch for the oxide to the resist is app. 1:2 and due to the relative thin resist it is now difficult to transfer the mask pattern to the protecting thermal oxide layer without total removing the resist. If all the resist is removed it affects the etch rates, thereby loosing the control of the depth of the guides. The problem was solved by adding a poly silicon layer on top of the oxide. The pattern is then by e beam transferred to the resist, developed and then by a silicon RIE etching transferred to the poly silicon. The resist is then removed and the poly silicon is working as etching mask. The thickness of the poly silicon was ap. 70 nm and when etching through the oxide and into the silicon below, making the cavities, the poly silicon is also removed.

The pattern was aligned with the wafer flat and placed in the center of the wafer. One pattern was written pr. wafer so that every line for that wafer has the same depth. The final patter size was ap. 1cm^2. The wafers were as for the UV bonded annealed at 1000 degrees for 30 min , and then cut in 1-3 mm pieces. The process steps are illustrated in appendix A.

Guides with the plateau were only made for the one dimensional guides whereas the thin top wafer bonding were made for both. These samples were far more mechanically stable.

8.4   Characterization

During the process development the structures were investigated with optical microscopey to check the quality of the structures. AFM was used to estimate the roughness of the bottom and the sidewall structures of the cavities before the bonding. Further the bonding was inspected by IR camera. X-ray reflectivity measurements were used to estimate the height of the cavitiesafter bonding. Transmissions scans were measured to check the position the cavities withrespect to the beam. and bonding in between the guides.

8.4.1   Optical microscope

With the optical microscopy it was possible to inspect the surface after UV-exposure and the different etching and wet chemical cleaning steps. Excess of resist material can damage the surface and spoil the ability of bonding later.

Examples of microscope images from one dimensional cavities are depicted in figure 8.4.
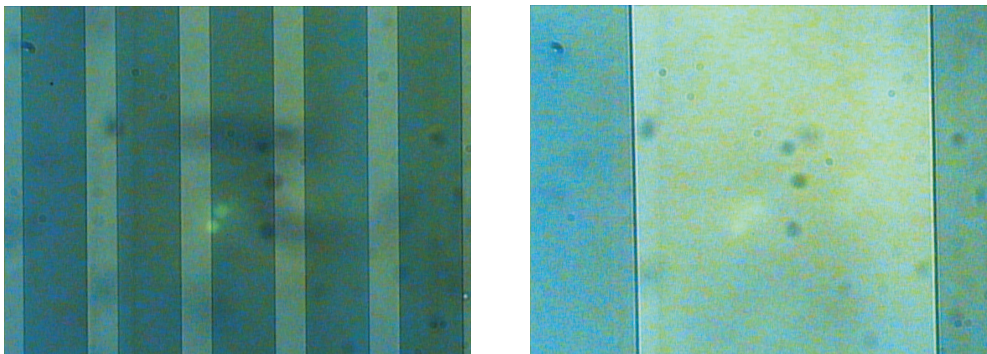

Figure 8.4: left: Optical microscope picture of 1.5 μm lines after etching the structure in the oxide. Right: 100 μ line also after oxide etching

As can be seen in the images for the one dimensional structures, the quality of the pattern is good. The pictures shows the structures after the oxide etch prior to the etching into the silicon wafer. Even though the 1.5 μm lines are close to the limit of resolution, nice well defined structures were observed. Further the area in between the structures were inspected and in general no additional structures from left over of resist were observed.

The two dimensional cavities are too small in order to get a detailed overview of the channels, but the general condition of the whole wafer and especially the areas around the channels, were we need the wafer to be good bonded can be inspected. Examples of optical inspection of the narrow to dimensional channels is depicted in figure 8.5
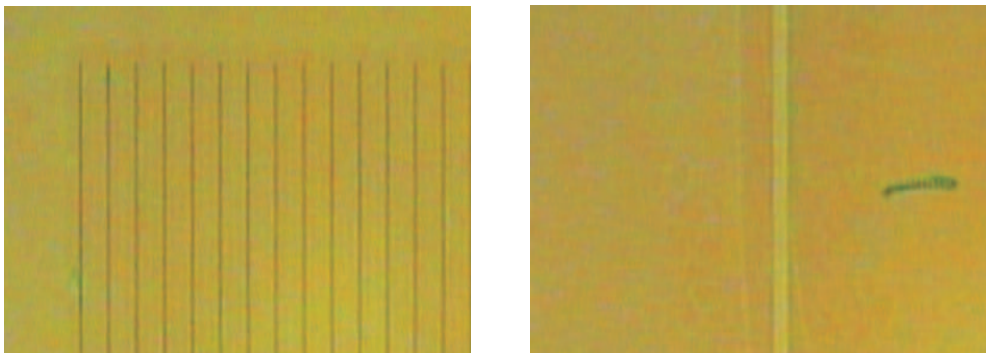

Figure 8.5: left: Optical microscope picture of 200nm lines after etching the structure in the oxide. Right: A single 5 μm line from the same wafer. The dirt in the right part of the pictures are from defects in the resist layer.

The thin bonded 1D samples were inspected both prior and after the bonding. It was clear from the microscope pictures after bonding, that some of the structures were damaged. For some cavities it seemed like the top wafer was broken and small parts was floating around at the surface. At other places the structure was rough at the channel edges, maybe due to chemicals attack during the KOH and HF thinning of the backside handle wafer. Other parts seemed to be OK. The backside thinning is carried out app. seven hours in KOH, using a special designed holder for etching only at one side. If the holder is not sufficiently tight , KOH can attack the edge of the wafer. Since the design of the pattern is placed close to the edge there is possibility that KOH actually is located inside the closed channels.

Furthermore there was circulation in the KOH bath and in the water used for rinsing the wafers after the etching. This can be a problem for the very thin top wafer, standing as membranes over the cavities. The width of the channels are several microns, and the thickness is only 500 Å, making them very mechanical unstable, and small vibrations from the circulation can easily cause them to break. Pictures from the bonded thin samples are found in figure 8.6.
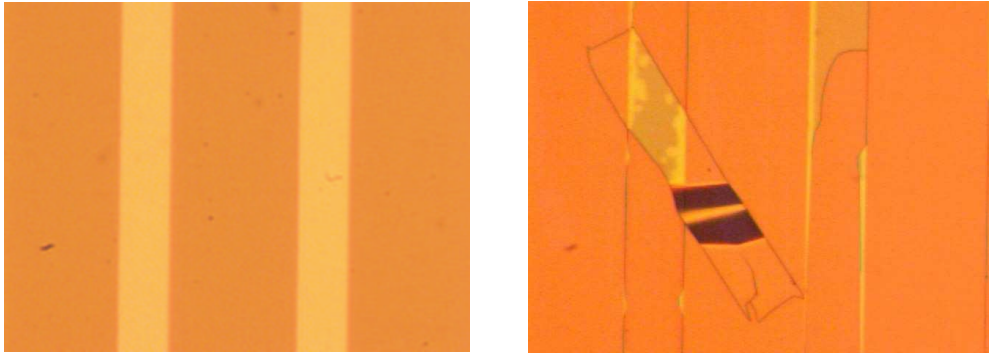
Figure 8.6: left: Optical microscope picture of 10 μm lines after bonding. The top wafer is ap. 50 nm. Right: A damaged guide. The thin upper wafer is broken and the piece is floating at the surface.

For the two dimensional guide it was not possible to inspect the the quality in detail using the microscope,but we would expect that no KOH has been into the channels, since they are only placed in a 10x10 mm area at the center. Further the width for these samples are in the nm range making the top wafer much more mechanical stable.

8.4.2   AFM

The roughness of the walls in the cavity is very important when reflecting the x-rays within the guides. AFM measurements in the bottom, and on the top prior to the bonding step, was used to evaluate the surface quality after the etching. The profile structure is depending on the shape of the AFM tip and when measuring relative sharp edges the resulting edge profile is rather a picture of the tip shape than of the true structure. The sidewalls were not examined by AFM, since for measuring the sides, the cavities has to be cut though the middle and tilted 90 degrees. For measuring the top wafer roughness a hole wafer that has been rinsed in HF for 30 sec was used.

The roughness in the bottom of the 1D guides were typically in the range of 10-30Å. The area in between the channels have typically values around 10-15Å. This is slightly more than the roughness for standard polished silicon wafers, but sufficient good for the bonding process. The enhanced roughness in the bottom can explain why asymmetric reflectivity curves are observed depending on using positive or negative incoming angles.

For evaluating on the etching angle SEM pictures made on comparable etch teststructures[29] has be inspected. An example of a RIE silicon etch on a test structure is depicted in figure 8.8.

As can be seen in the figure the RIE etch do not result in straight walls. Angles of several degrees were observed and this will for sure affect the result of two dimensional wave guiding were the beam are reflected from the sides. The structure on the walls
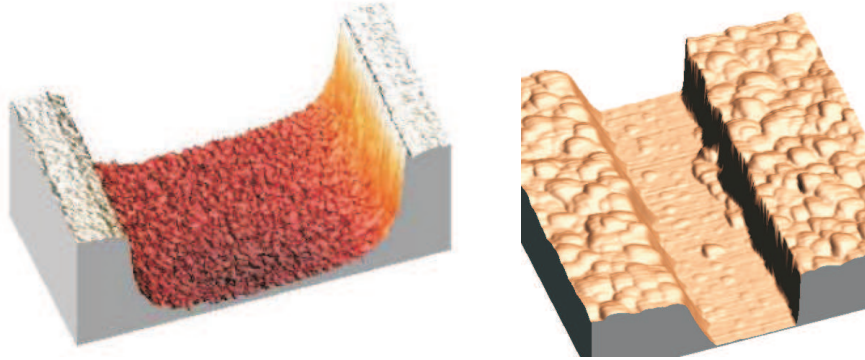
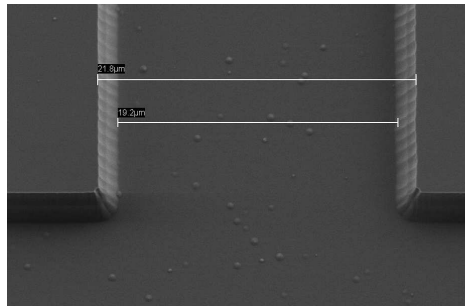Figure 8.7: left: AFM picture of 1D guide. Right: AFM of a 200nm guide.

Figure 8.8: SEM picture of the a silicon RIE etch.

in the figure are properly related to the quality of the lithography and has not been observed for our samples.

8.5   X-ray translation- and reflectivity scans

To ensure that the guides were not collapsed after the bonding and for mapping the positions of the guides, the sample was horizontally translated through the beam. The transmitted through the sample as a function of beam position along the sample was measured. The beam size were chosen to match the size of the cavities. The transmission is high when the beam hits a cavity and drops to zero between. The latter is important since it shows that the the sample is well bonded. The length is typically several mm and the absorbtion length for silicon at 10 kev is 133.7 microns.

An example of 10 one dimensional guides is illustrated in figure 8.9 above. All 10 wave-guides with the expected 300 μm spacing can be seen. The transmitted intensities are quite similar for the ten wave-guides, with only one exception. Furthermore we observed that the intensity in between the cavities went to zero indicating successfully
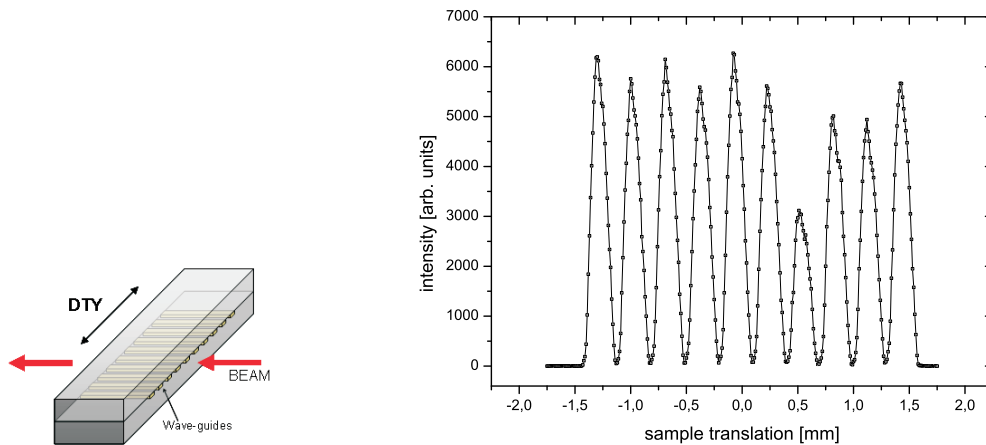
Figure 8.9: left: Translation scan setup. Right: Example of translation scan for 10 equally spaced 100 μm guides..

bonding. The intensity variation in the transmitted beam can be explained by silicon dust and gains left overs from the cutting. The cutting is a relative rough process. This was investigated by SEM and that clearly showed traces from the diamond blade and small pieces of silicon all over.

For the 2 dimensional cavities the transmitted intensity through a single guide was very small, making the localization rather difficult. In the design we had hence made several 5 microns line and by localizing them first the 100 and 200 nm lines lines could be find by translating the sample a known distance.
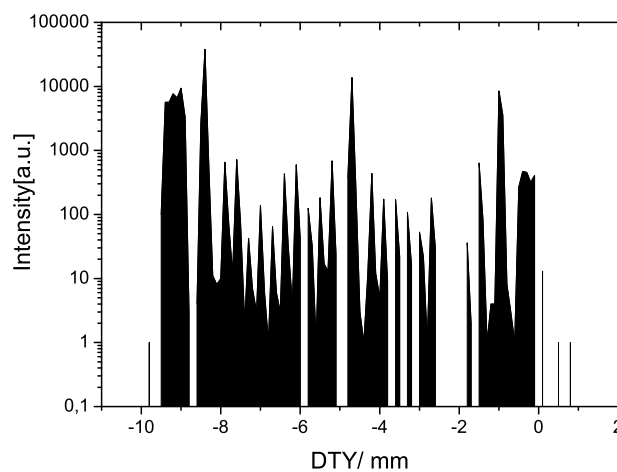

Figure 8.10: Translation scan of 2D guides.

The outer most broad peaks corresponds to the array of 50 guides of width 100-200nm. The three smaller peaks are the 5 μm guides made for orientation whereas the smallest peaks corresponds to single guides. The width of the beam are large compared to the width of the guide and the in between spacing, and hitting only a single guide is not possible.

For the thin top wafer samples it was clearly not possible to make the translations scan directly. The direct beam will not be absorbed in the silicon top wafer as before and light passing through the guide can not be distinguished from the direct beam. Instead a translation scan were done at a Bragg reflection and when hitting areas with guides intensity changes was expected. This was not possible for the single guides since the intensity changes were to small. The top wafer thickness were only 500Å, so the beam is only slightly attenuated,but for the array of guides we observed en effect and the width of the area were the intensity dropped were matching the total width of 50 guides. When localizing the array we could use the pattern design to find the position for the rest of the system.

After localizing the position were changes in intensity are observe in the translation scan, we tried to make a rod scan searching for oscillations. If guides were present,we would expect to see oscillation corresponding to the involved layers, silicon - air - silicon. The oscillations should only be in the rod scans made when the beam was reflected from a cavity area. Moving to areas outside, we only have silicon, and thereby no layer oscillations. An example is depicted in figure 8.11
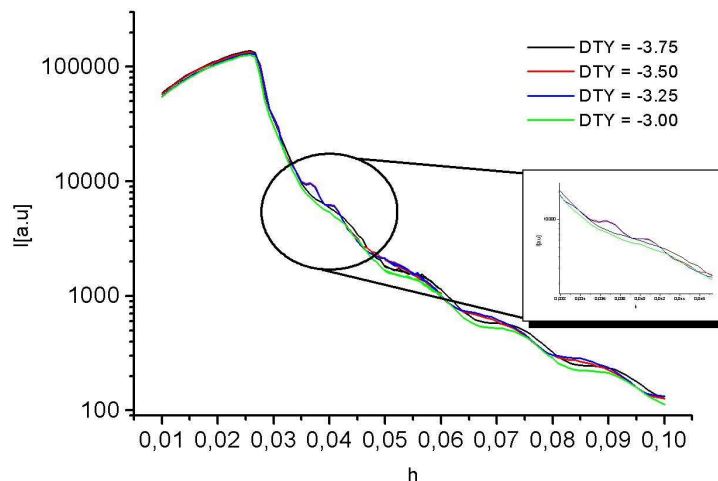

Figure 8.11: Rod scans within and outside a guide array area.

In the figure four scans are depicted. The red and blue curve is from positions with

cavities, the black an green from outside. As can be seen in the blow up the extra oscillations are only visible in the red and blue curve indicating that there is a layer structure here.

For the one and two dimensional guides with the standard wafer on top we made reflectivity measurements using 1mm long samples. The period of the thickness oscillation were compared to expected values known from the etch rates, and in general good agreement were found. An example of at typical reflections scan is illustrated in figure 8.12. This is from a 1D nominally 625 Å thick guide 1 mm long.

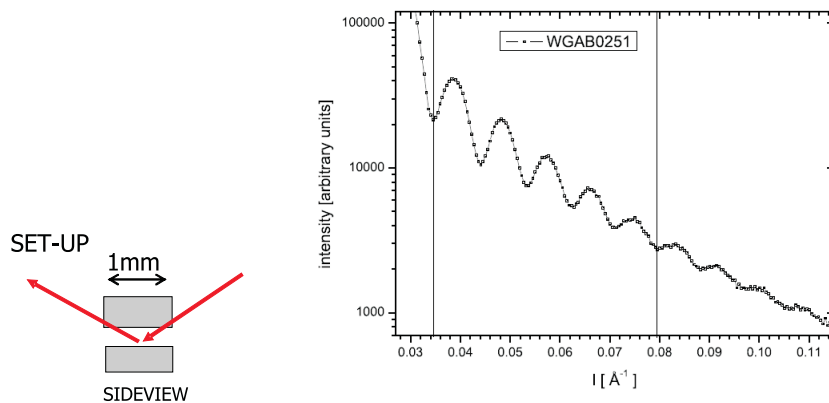
Figure 8.12: left: Reflectivity setup. Right: Example of reflectivity scan for a 625Å nominal thick guide

As can be seen there are oscillations with a period corresponding to a thickness of 698 Å which is close to the 625Å . In general the depth of the guide were in good agreement with what was expected from the etch rate tests in the cleanroom, and we can conclude that it was possible to control the depth, by adjusting the process time to obtain the wanted dimensions.

8.6   Summary

In general the quality of the lithography was good, both using the UV and e-beam technique. For the one dimensional cavities , the etching rates and thereby the depth of the guide were in good agreement with the results from the x-ray reflectivity. Further optimization runs o n the system would properly results in even better control. Using the RIE system resulted in relatively low roughness in the bottom, but the unfortunately there seems to be some problems with the straightness of the side walls. More time should be spent on investigating alternative etching methods, keeping in mind that the roughness in the bottom should still be acceptable.

Experiments with guides made with a in coupler plateau in front has been made, but no remarkable effects were seen on the intensities, and a better solution would properly be to combine the guides with a pre-focusing system.

The transmission through the guides has been calculated by comparing the amount of intensity actually hitting the entrance of the guide to the measured intensity at the exit. Typically values of 20-30% were found for the 1D guides. The intensity loss is properly connected to the quality of the silicon surfaces inside the guide and maybe also to material blocking at the entrance and exit.

After characterizing the guides, knowing the dimensions, the number of modes and their position can be calculated from the transcendental equation.

Chapter 9

X-ray measurements on waveguides

In this chapter examples of x-ray measurement are presented. The one dimensional waveguides have mainly been measured at BW2, Hamburg [30] using an energy of 10keV, whereas the two dimensional guides were investigated at ID1 at ESRF in Grenoble [23] with an energy of 12 keV.

The first section of this chapter contains general information about the set-up and alignment of the experiment. In the second section there is a description of measurements on one dimensional cavities performed at BW2. The section contains a selected number of measurements and is ended with a summary. The last section describes measurements on two dimensional cavities. These measurements were made using a CCD camera measuring the intensity distribution in two dimensions. The measurements were recorded as a function of incidence angles and from the pictures a series of video sequences was made. In this section, however, only single frames can be showed. The section is ended with a summary.

9.1   Experimental setup

The samples were mounted in the diffractometer using a sample holder designed for the guides (figure 9.1). Using the holder it was possible to entrance the guide at both positive and negative angles.

The holder was made such that samples with different lengths and thicknesses could be mounted. In the bottom plate, an extra hole was cut (not shown in figure) so that transmission of the direct beam could be used as alignment both from the front and top of the sample. In order to align the sample to be in the center of rotation of the diffractometer, it is important that the sample is aligned translational in both directions. Furthermore, using the shadow effect of the sample strip, the sample was aligned
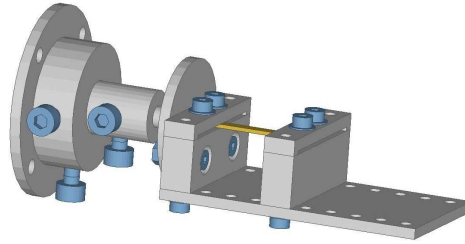
Figure 9.1: Sample holder for waveguide designed by Bunk et al.

to be horizontal.

As all the wafers were equal in thickness(350μm), it was possible to locate the verti-cal position where the cavities were expected, and from this position the samples were translated horizontal. The length of the samples was several millimeters and only when hitting a cavity transmitted intensity was observed. In this way the exact position of the guides was located. An example of a translation scan was depicted in the previous chapter, figure 8.9.

In order to obtain information about the exact height of the guides, reflectivity scans on 1 mm samples were made. For this thickness, the transmission of photons (10keV) through the sample is sufficient to perform reflectivity measurements above the critical angle for total reflections. The cavity height was measured in the cleanroom before closing the guides and not always on the actual sample used for the cavities. Instead a test wafer made in parallel using same recipes was measured. This is not as precise as the result from a reflectivity measurement, and to evaluate on the control of the etch rate the two values are compared. An example of a reflectivity scan was also presented in the previous chapter, figure 8.12.

Knowing the exact dimensions of the guides, the expected mode number and position can be calculated and compared with what was observed experimentally.

9.2   Planar waveguide - one dimensional guiding

Many planar one dimensional structures were made with different dimensions. In this section some of the measurements have been selected and will be presented. The results are compared to theoretical predictions, in order to illustrate a 'proof of principle' of our x-ray waveguiding systems. The guides chosen to be discussed in more details here are nominal 625{Å high guides of different widths and lengths. Besides of the standard front coupled measurements, a few results using a incoupling plateau in front are presented.

9.3   Investigations of 698Å(625Å) waveguides

This guide was made as described in the previous chapter, with an expected depth of 625 Å. This depth was chosen because it would allow 4 wave guiding modes to be inspected. The sample was aligned as described in the procedure above. First the exact height was measured by reflectivity. From this it was found that the guides were deeper than expected having reflectivity oscillations corresponding to a height of 698 ± 8 Å. 698Å is approximately 10% more than expected. Better agreement can be obtained by running more etch test experiments and adjusting the gasses used for the etching procedure, but as the tests are very time consuming, we were satisfied with 10 percent.

To map the exact position of the guides in the sample, a translations scan was made as described above. The beam dimensions were sat to 10μ x 100μ and the detector slits to 0.5 mm in both directions. The translation scan for the guides is depicted in figure 9.2 The number marks in the figure correspond to the later measured waveguides.
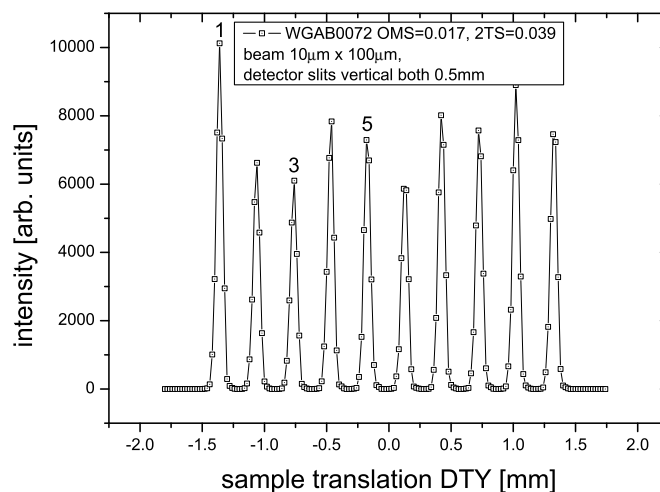

Figure 9.2: Horizontal sample translation scan (3mm x 100μm x 698Å)

In the translation scan, it can be seen that the transmitted intensities are very similar. The lower intensities for some of the guides can be due to grains blocking the front and exit of the guide from the cutting process. For each set of guides, samples of the length of 1, 3 and 5 mm had been made.

9.3.1   Expected mode behavior for a 698Å guide

By solving the transcendental equation (7.24), the number of expected modes and their positions can be calculated. For a d = 698Å, SiO_2/air waveguide, four mode positions are found using an energy of 10keV. The index of refraction inside the guide, n_1 is 1

and for the waveguide material, n_2 is $1-3.0016\cdot10^{-6}(SiO_2)$. The found transcendental solutions are listed in the table below.

x	α_i	mode number
2.644	0.0428	0
5.250	0.0852	1
7.800	0.1263	2
10.114	0.1638	3

Table 9.1: Transcendental equation parameter x and corresponding incidence angle α_i at E = 10keV

The 3'th mode is found at an angle of $0.1638°$ which is close to the critical angle for SiO_2 at 10keV of $0.174°$. Therefore a significant part of the intensity is outside the waveguide in the walls, i.e., the mode is close to becoming a leaky mode. As a result this will properly lead to an increased damping of this mode compared to the others.

The far-field intensity for the modes and the sum of all modes are shown on linear and logarithmic intensity scale in figure 9.3 and 9.4. In the logarithmic plot the higher orders of the single slit diffraction from the coherent light exiting the waveguide can be seen. For a guide of height h and a wavelength λ the first minimum in the exit-angle α_f is at $\alpha_f = arcsin(\lambda/h)(0.10°$ for h = 698Å and $\lambda = 1.24$Å[13].
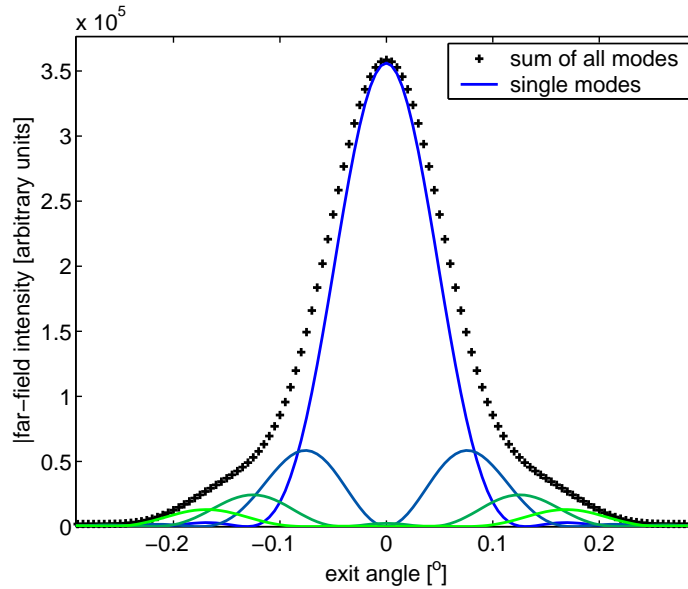

Figure 9.3: Far-field intensity for the modes of a 698Å waveguide and the intensity summed over all modes on linear scale [13].
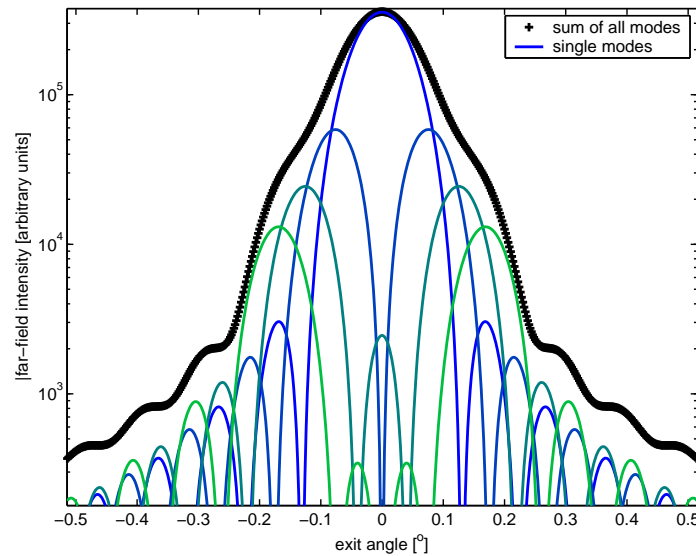
Figure 9.4: Far-field intensity for the modes of a 698Å waveguide and the intensity summed over all modes on logarithmic scale. Higher orders of the single slit diffraction from the coherent light exiting the waveguide can be seen [13].

9.3.2   Measurements on 698Å guides

The far-field intensities of the guides were measured by scanning for a selected range of incidence and exit angles. In this way a two dimensional mapping of the intensity behavior was recorded. A sketch of the geometry is depicted in figure 9.5.
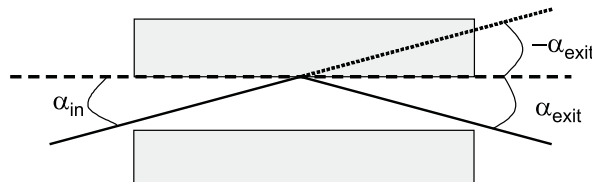

Figure 9.5: sketch of incidence and exit angles for a waveguide.

In figure 9.6 the intensity map measured on a 3 mm long, 100 μm wide and 698Å high guide is depicted. The numbers on the figure correspond to the maxima of the calculated intensities, 1 is the 0-order of mode, 2 is the 1st order of mode and etc. The standard reflectivity curves $\alpha_{in} = \alpha_{exit}$ and simple transmission $\alpha_{in} = -\alpha_{exit}$ are the diagonals in the plot.

The measured intensity map is almost symmetric, with raised intensities close to the expected positions, clearly showing the effect of waveguiding. As the samples are relatively long no significant intensity contribution from the simple transmitted ($\alpha_{in} = -\alpha_{exit}$) beam is expected when moving away from zero incidence due to absorbtion. The intensity from the standard reflected ($\alpha_{in} = \alpha_{exit}$) beam is also expected to be low, with
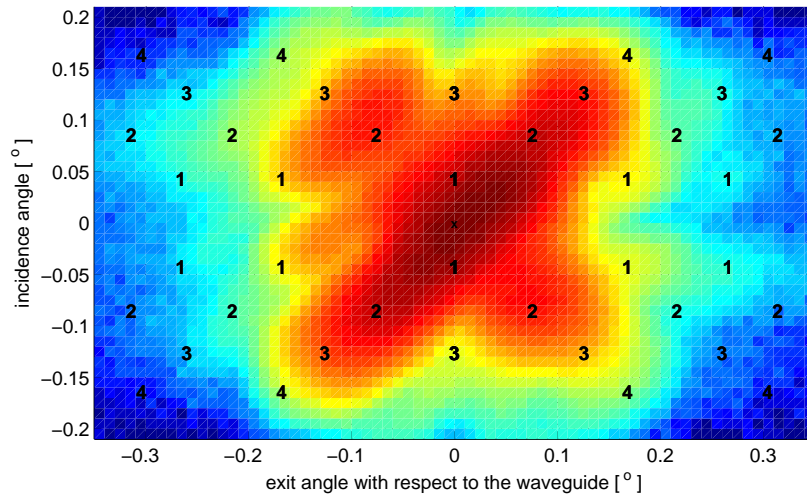
Figure 9.6: Far-field intensity map recorded at position 1 in figure 9.2[13].

highest contributions at small angles.

The incidence angles for the 4 modes are relatively close. This means that the possibility of exciting several modes at a time is relatively high, which is also observed in the scans. For obtaining single mode guiding, smaller guides have to be made. In this project the smallest investigated guide had a height of 286Å resulting in two modes[12]. Alternatively a lower energy could be used to increase the separation of the modes.

Two other guides at position 3 and 5 in the transmission scan, have also been measured. The results from position 5 are depicted in figure 9.7.
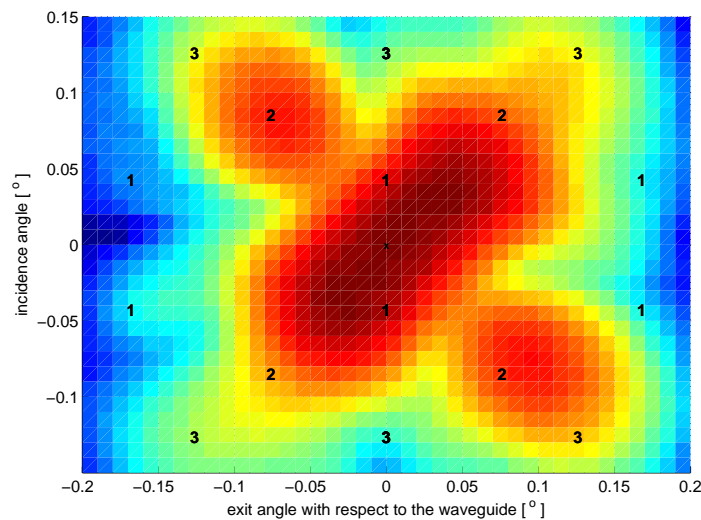

Figure 9.7: Far-field intensity map recorded at position 5 in figure 9.2[13].

In general the measured intensity maps are similar, and as expected the intensities were lower. The map is more asymmetric, but 1'st order modes marked with number two in the figure are more clearly separated. The reason for the asymmetry is not clear, but may be related to the lower quality of the guide.

The measurements were also performed on 1 and 5 mm samples. For each sample, translation scans were done mapping the array of the ten 100μm guides, and as for the 3 mm sample some variations in the intensities in between guides in the array were observed. Examples of measurements on a 1 mm and 5 mm sample are depicted in figure 9.8 and 9.9.
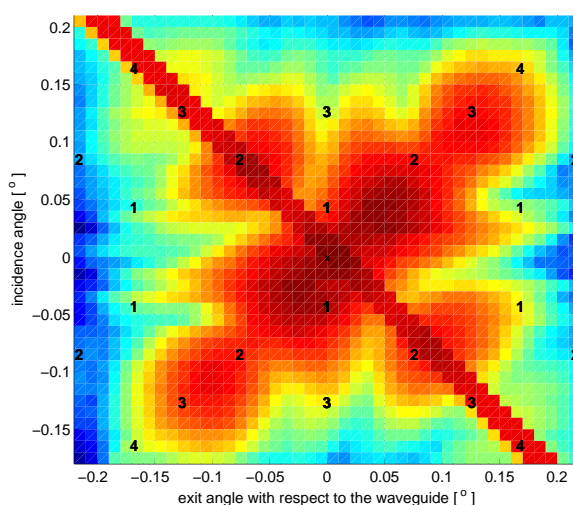

Figure 9.8: Far-field intensity map recorded for a 1 mm long, 100 μm wide and 698Å high guide. Maxima of the calculated far-field intensities are marked in the figure [13].

As expected the transmission intensity (the diagonal from the upper left to the lower right) recorded for the 1 mm guide is higher compared to the 3 mm guide (due to lower absorbtion). In general the pattern in the map is similar to the ones observed for the 3 mm guide, but with less intensities at the expected maxima positions. This indicates lower guiding efficiency, and that the observed intensities are dominated by reflected and transmitted intensities.

In figure 9.9 the map for a 5 mm guide is depicted. For unknown reasons the measurements are shifted by $0.078°$,$-0.03°$ with respect to the previous observed positions. The observed intensities are lower and the transmission intensity is no longer dominating. Raised intensities are still observed approximately at the expected maxima positions, but the pattern is more smeared out. In general it seems that the longer the sample the more smeared out the far-field pattern is, and this is most properly due to roughness problems of the interfaces in the cavities.
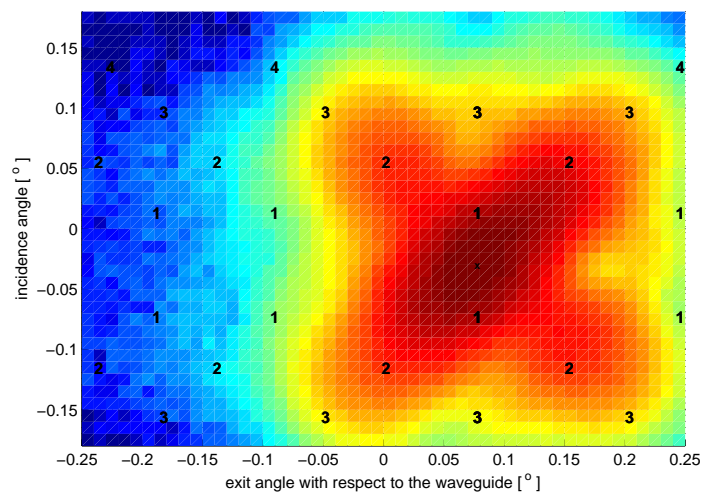
Figure 9.9: Far-field intensity map recorded for a 5 mm long, 100 μm wide and 698Å high guide. Maxima of the calculated far-field intensities are marked in the figure. Note that the marked positions are arbitrary shifted by (0.078°,-0.03°) [13].

Measurements on guides with an amplifier plateau

A series of guides were made with an amplifier plateau in front in order to increase the intensity entering the guides. In figure 9.10 an example of a measurement on an array of 10 guides, 3 mm long, 3 μm wide, 698Å high and with a 1mm incoupling plateau in front of the guides is shown. For comparison a measurement on the same type of guides without a plateau is depicted to the right.

As can be seen in the figure on the left the lower part of the intensity map is absent due to the plateau in front blocking the intensity. The measurements are made on two identical prepared arrays of guides of same type. Even though they are made using the same recipe, some small differences can be present. The small difference in the intensity pattern is comparable with what is typically observed measuring different positions/guides within an array.

To be able to compare the intensities, an intensity ratio has been calculated for each single guide and the array measurements[13]. The peak intensities are normalized with the counts from the beamline monitor, which is the monitor situated in the vacuum part of the beamline in front of the slit system. Further the intensities were normalized with the cross section area of the guides (nominally width times measured hight). The length of the guides does not enter the calculation. The area normalized ratio is expected to be more or less the same for all the guides, as they cut a part of the direct beam corresponding to the guide area, and a low ratio corresponds to a less effective guide.

The area normalized ratio for 3 mm long guides with a plateau measured on several comparable samples, was found to be in the range of 1.28 - 1.48. For 3 mm guides
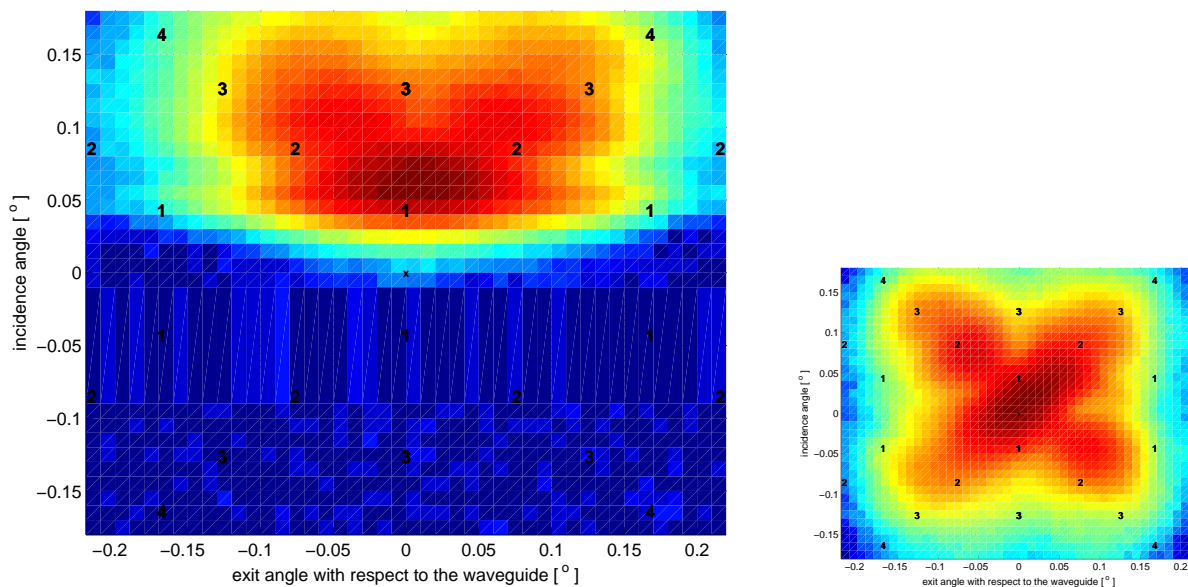
Figure 9.10: Left: Intensity map for an array of 10 guides, 3 mm long, 3 μm wide and 698Å high with a 1 mm incoupling area in front of the guides. Right: Intensity map for an array of 10 guides, 3 mm long, 3 μm wide and 698Å high without plateau.

without plateau the values were in the range of 1.03 - 1.13. Comparing the ranges indicates that adding a plateau clearly affects the measured intensities in a positive way.

Measurements on guides with alcohol

Single test experiments were made filling the guides with alcohol. This was done by dropping alcohol on the guides, and it has to be remarked that in the test it was not clear whether the alcohol was wetting the entire cavity or not. The guides were measured before and after the filling in order to investigate how the alcohol affected the mode properties. An example of a 1 mm long, 100 μm wide and 698Å high single waveguide with alcohol is depicted in figure 9.11. The guide measured without alcohol is depicted in 9.8.

For ethylene glycol the refractive index is n = 1 -2.32·10^{-6}, which has to be entered in the mode calculations. According to the calculations, the shift of the first three modes is almost negligible, changing from 0.043°, 0.085 ° and 0.126° to 0.040°, 0.079° and 0.114° for the incidence angle. For the exit angle a corresponding minor shift is observed. The 4'th mode will be at a incidence angle of 0.168°, which is above the critical angle of 0.123° for the ethylene glycol /SiO^2 interface and is no longer expected to be observed.
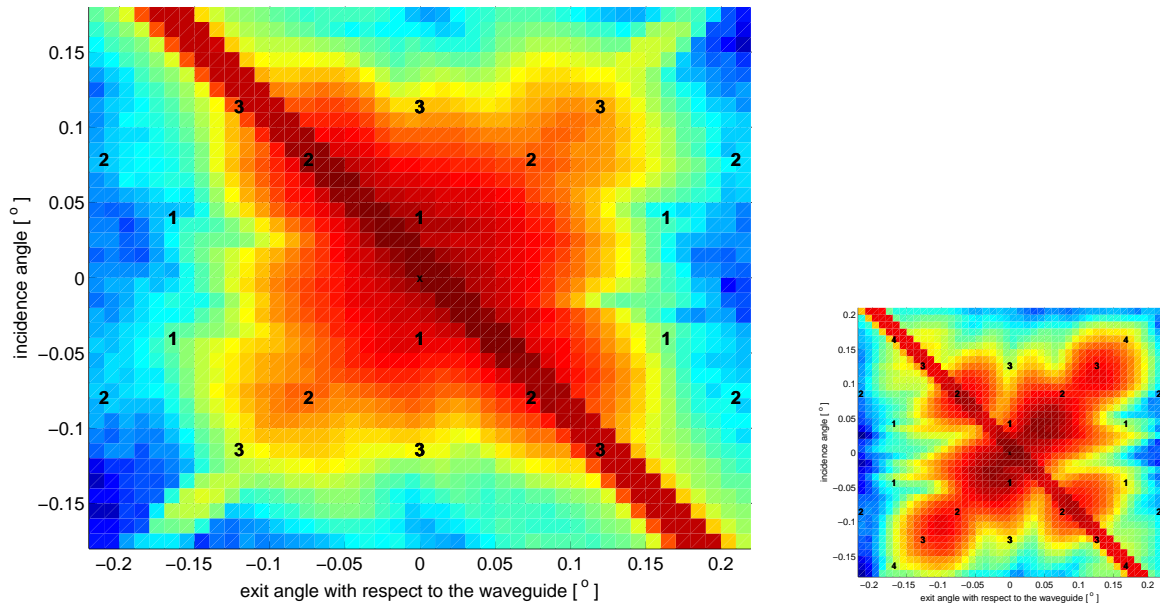
Figure 9.11: Left: Maps for a 1 mm long, 100 μm wide and 698P high single waveguide with ethylene glycol (position b in the translations scan). Maxima of the far-field are marked in the figure[13]. Right: Copy of 9.8 which is the intensity map for the same guide without alcohol.

The measured data depicted in figure 9.11 show the expected cut-off above the critical angle, and as expected, no 4'th mode. The rest of the modes are in relatively good agreement with the marked maxima positions, but compared to the measurement without alcohol, a blurring of the modes can be seen. Further the filling in general was found to lower the intensity ratio. For the guide in the figure it decreased from 1.01 to 0.69.

Several other guides with other heights have been measured. Some of these results can be found in appendix B, where a selected amount of examples for a 454Å and a 1351Å is presented.

9.3.3   Summary

It was clear from the measurements that one dimensional waveguides have successfully been fabricated using UV-lithography, RIE etching and wafer bonding. During the experiments some problems were found, and these have to be solved in order to raise the quality of the waveguiding. From the experiments on the one dimensional guide we concluded that:

- General good agreement was between expected and calculated mode positions.

- The measured intensities are smeared out as a function of the length of the guides. More clear mode separation is observed for the 1 mm samples compared to those of 3 and 5 mm. This may be related to the roughness of the samples.

- In general the depth measured in the cleanroom and with reflectivity are in agreement. The measured depths were above the measurements from the cleanroom, but agreed within 10%. This could be improved by further test experiments with the RIE system.

- No single mode guiding was observed. Making smaller structures would lower the number of modes and raise their separation. Larger separation would decrease the probability of modemixing where several modes are observed simultaneously. Further it is suggested to measure at lower energies which will also raise the separation. Measuring at lower energies should be possible with our structures, as we are not limited by absorbtion in the guide region.

- Modemixing will also be the result if the interface roughness is high. The roughness in the bottom of the cavities is determined by the used etch, and it should be considered if alternative etching methods result in less rough interfaces.

9.4   Two dimensional guiding

The measurements presented in this section are all performed at beamline ID1 at ESRF. The two dimensional guides were aligned as described above, and translation scans were made to localize the position of the guides. The width was determined by the e-beam process and expected to be either 1000 or 2000Å. The height was controlled by the RIE etching, but since the guides are relatively narrow, it was not possible to measure the depth of the etch at the real structure. Instead the etch rate was calculated using an area comparable etched test structure. The difference between the nominally height and the calculated height was found from x-ray reflectivity measurements and the height measured by x-rays was used as input value in the transcendental equation.

The width of the guides are now narrow enough to obtain guiding also in the horizontal direction. To record the mode intensity, a CCD camera was used. In this way both horizontal and vertical exit angles as a function of the incidence angle could be measured at the same time. In the measurements, either the horizontal or vertical incidence angle was situated at a fixed position, while the other was scanned. From the recorded CCD images, film sequences were created and the development of modes as a function of incidence angles could be investigated. A list of the different scan directions is given below and more information about the diffractometer can be found in [23].

Hai scans Vertical scan of incidence angle

Hphi scans Horizontal scan of incidence angle

delta Vertical scan of exit angle

mu Horizontal scan of exit angle

Hy Horizontal translation scan

9.4.1   Measurements on nominally 850Å high times 1000 and 2000 Å width guides

To map the structure a translation scan was made as described for the one dimensional measurements.
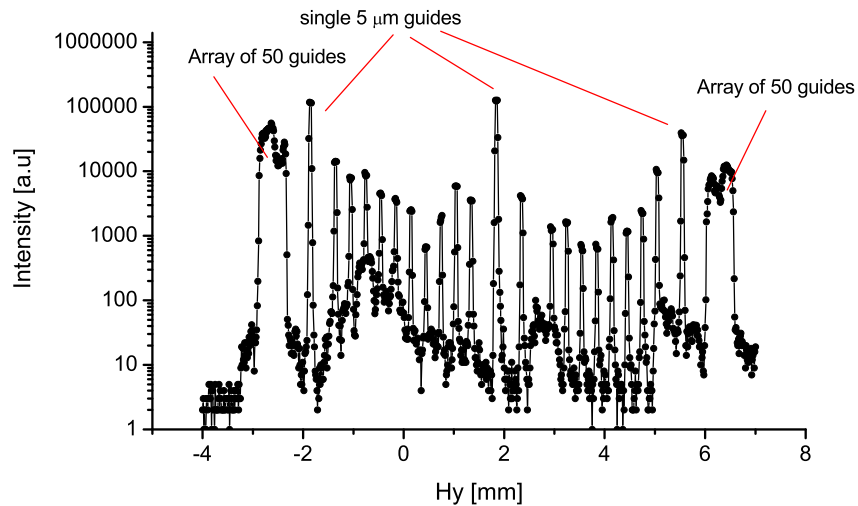

Figure 9.12: Translations scan mapping the positions of the cavities
.

The measured pattern should correspond to the mask design presented in the fabrication chapter. The array of cavities at the edges resulted in a broad intensity peak covering all the 50 guides and the two peaks besides the arrays and the one at the center correspond to the 5μ cavities. The small peaks in between are either single guide or double guides of nominally 1000 or 2000Å. The intensities of the small peaks are very alike, and it is not clear from the translation scan which side of the scan corresponds to 1000Å guides and which to the 2000Å guides.

The nominally height of the cavity is 850Å. To find the exact height, a reflectivity scan on a 1 mm long sample was done. The result is depicted in figure9.13.

The oscillations correspond to a thickness of 650Å. This is far below what was expected from the etch rate experiments, and it can be concluded that for the small two dimensional structures, the control of the etch dept has to be improved. It is believed that this could be obtained through further test experiments.

The expected mode position for a 650Å guide is listed in table 9.2.

An example of measured intensities at incidence horizontal angles (hai) situated at the positions listed in table 9.2 is depicted in figure 9.14 below. The measured guide is a
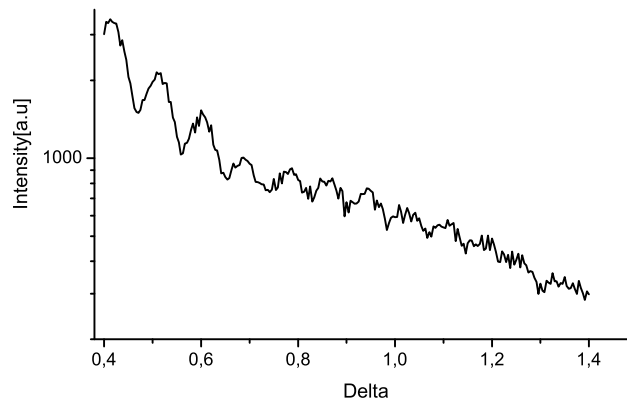
Figure 9.13: Reflectivity measurement on a nominally 850Å high cavity. The oscillations correspond to a thickness of 650Å.

x	α_i	mode number
2.613	0.0379	0
5.129	0.0753	1
7.676	0.113	2
9.816	0.1423	3

Table 9.2: Transcendental equation parameter x and corresponding incidence angle α_i for a 650Å guide at E = 12keV.

single guide situated at h_y=-0.77 in the translation scan and it is 3 mm long.
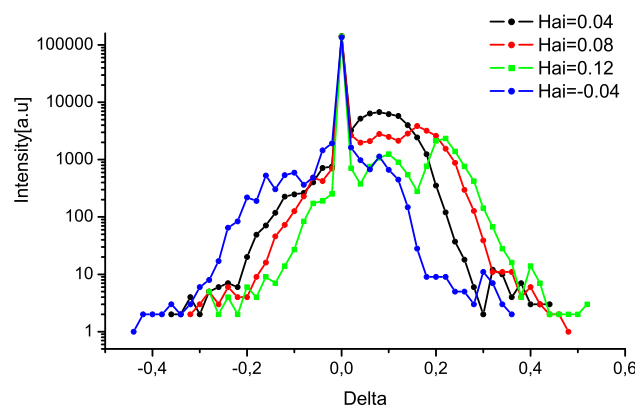

Figure 9.14: Delta scan for four hai values corresponding to the incidence angle of mode guiding.

For the guide, the measured signal moves as a function of hai, which is to be expected

as different modes are guided depending on the incidence angle. Extra peaks are observed for hai=0.08 (1'st order), which are not visible at hai=0.04. The same holds for hai=0.12. As we also observed for the one dimensional guides, we probably have a certain overlapping of modes. A scan was also done at hai=-0.04 (scan 16 in the figure) This scan was expected to be symmetric to the scan made at hai=0.04, however this was not the case. The asymmetry is speculated to be related to the quality of the guides.

The guides were nominally 1000 and 2000 Å in width. The incidence angles for the first three modes are listed in table 9.4.1.

$2000\mathring{A}guide$	$1000\mathring{A}guide$
0.0139	0.0262
0.0278	0.0523
0.0417	0.0781

Table 9.3: Transcendental equation parameter x and corresponding incidence angle α_i at E = 12keV

To check the agreement between nominally widths and actual widths of the guides a horizontal scan was made. This was done for a single 1000Åguide at position Hy=4.14.
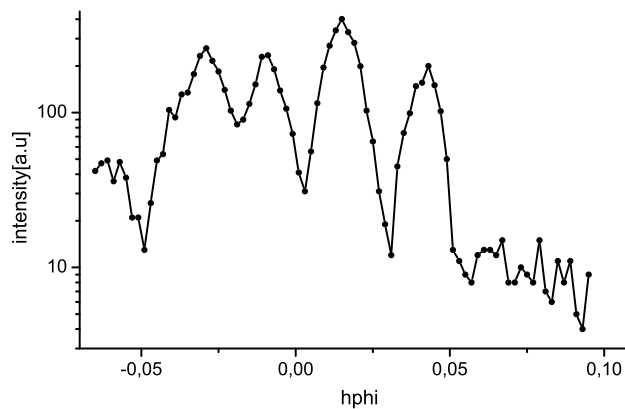

Figure 9.15: Hphi scan of a nominally 1000Å wide cavity.

The periodicity of the fringes is not regular. In the horizontal scan, reflectivity from the side walls is measured and it is known from the characterization that the side walls are not expected to be perpendicular and that the roughness can be increased. This can affect the measured periodicity. Further the measurements are disturbed by relatively high divergence in the horizontal plane (0.208 mrad compared to the vertical plane 0.009 mrad).

Taking the mean value of the distance between the four peaks in the middle results in a period corresponding to a thickness of 2682Å. This value can not be considered

as the exact width, but the width is far above the expected value of 1000Å. In the translation scan 9.12 almost equal intensities are observed in the left and right part, and it is possible that the width of the nominally 1000Å and 2000Å guides are almost identical with a width of 2000-2800Å. Not knowing the exact width it is difficult to calculate the incidence mode angles.

9.4.2   Examples of measured far-field intensities

The far-field intensities of the waveguides were investigated for several structures. The intensities were recorded with a CCD camera as a function of incidence angles, and the pictures were combined into movie sequences. In this section a selected number of frames from some of the movies for a 650Å waveguide are presented. The pictures give an overview of the guide behavior in both directions when changing the incidence angle.

The first guide to be considered was a 5μm wide, 650Å high and 3 mm long guide. For these dimensions, four modes are expected in the vertical direction, while for widths of 5μm no guiding will take place in the horizontal direction.

The pictures in figure 9.16 show four frames corresponding to the calculated incidence angles for the four modes. A = 0.039°, B=0.0753°, C=0.113° and D=0.1423°. The angles were found by solving the transcendental equation for a 650Å high guide measured at 12 keV. Picture A corresponds to 0'th mode and a single intensity peak around zero exit angle is expected. Moving from frame A to D the different modes are observed. As for the guides measured a BW2, we also observe overlap of modes for this guide. Further it seems to be asymmetric with the mode intensities shifted towards positive angles.

The opposite scan for the 5μm guide is depicted in figure 9.17. No guiding in this direction is expected.

Four frames are depicted in the figure corresponding to horizontal incidence angles of A = -0.05°, B=0°, C=0.05° and D=0.1°. No guiding was observed, but the transmitted and the reflected intensity from the interfaces were very intense. The vertical incidence angle was sat to 0.038 ° and the observed intensity variations in the vertical direction are related to wave guiding in this direction. 0.038 ° corresponds to 0'th order mode excitation, but the 1'st order is also observed. Further interference patterns were observed around the reflected signal, which are probably related to the quality of the interface in the guide. The divergence of the beam in this direction is high and will also affect the measured intensities.
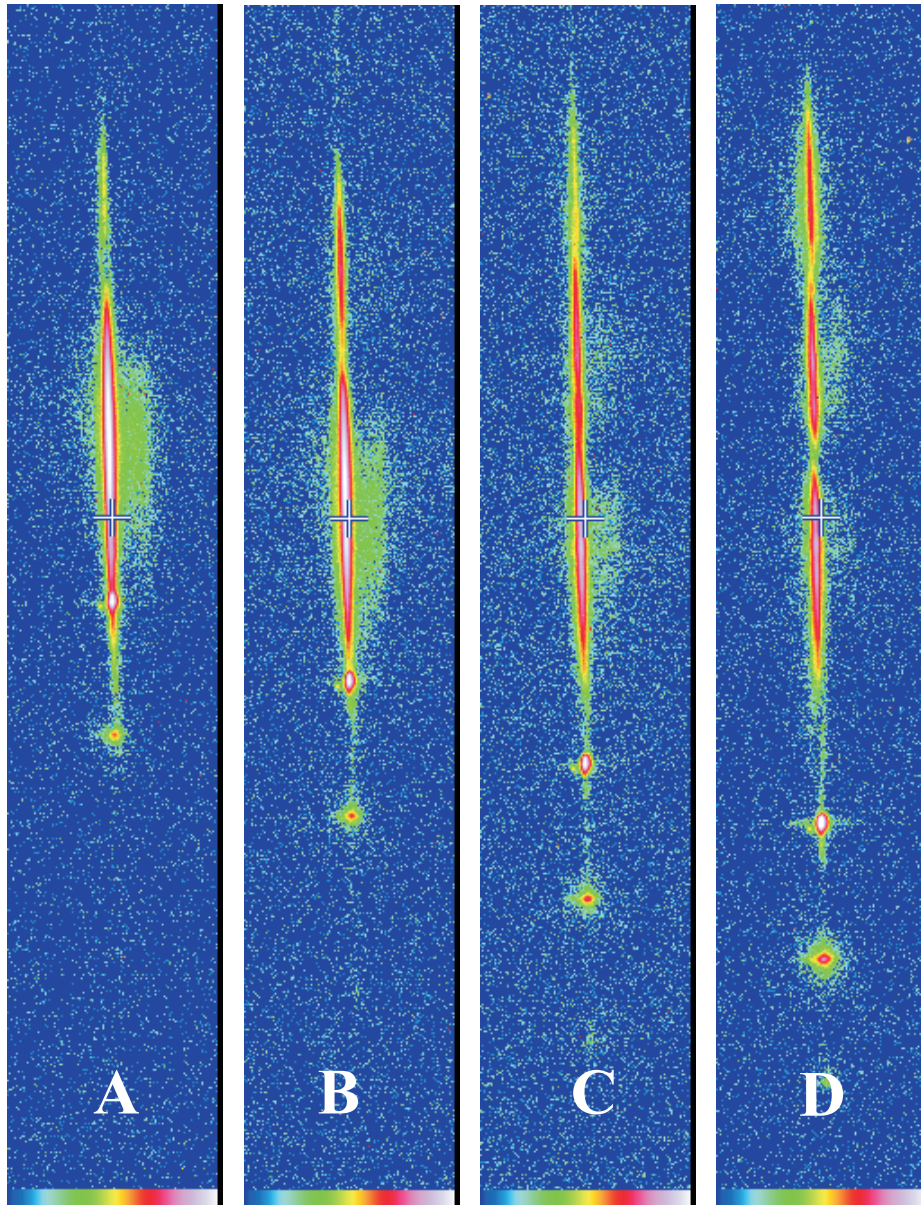
Figure 9.16: Far-field intensities measured in two dimensions with a CCD camera for a 5μm wide guide, when the vertical incidence angle (hai) is scanned. The selected frames correspond to the calculated incidence angles for the four modes. A = $0.039°$, B=$0.0753°$, C=$0.113°$ and D=$0.1423°$. Hphi = $0°$.
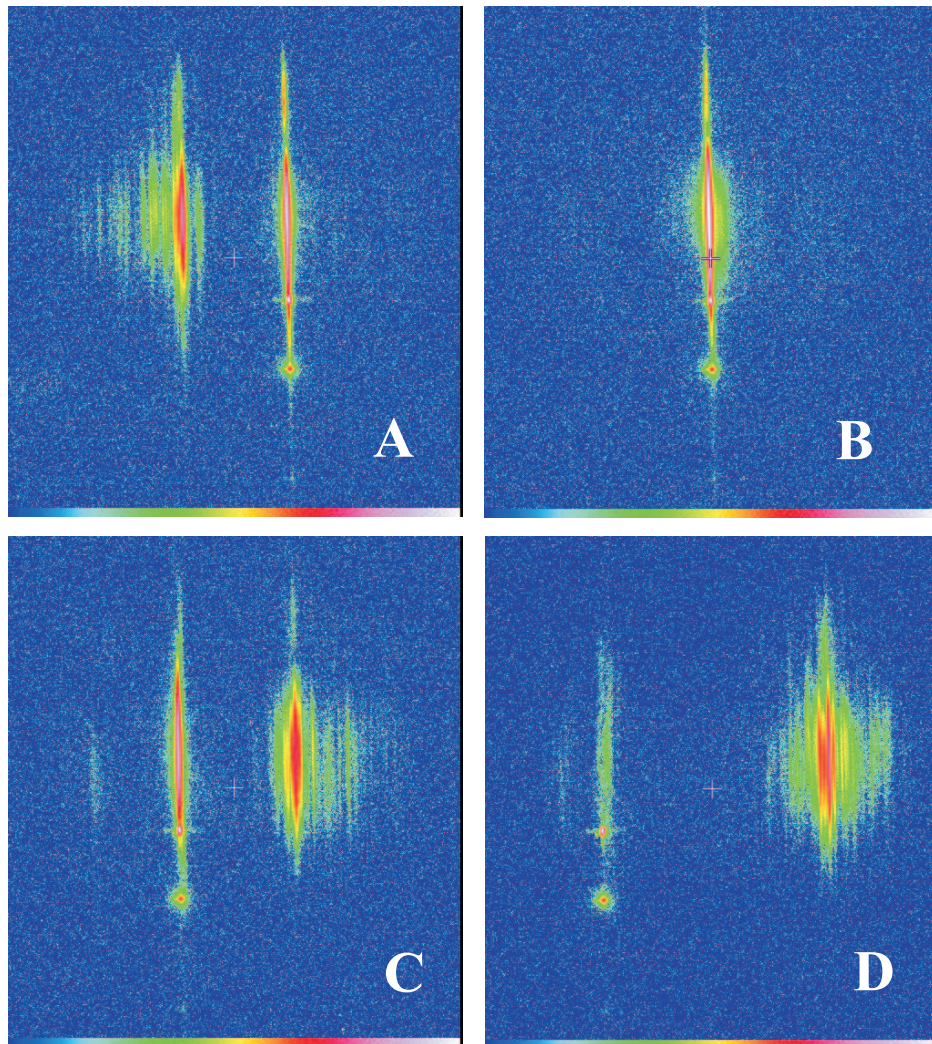
Figure 9.17: Far-field intensities measured in two dimensions with a CCD camera for a 5μm wide guide, when the horizontal incidence angle (hphi) is scanned. The selected frames correspond to incidence angles of A = -0.05°, B=0°, C=0.05° and D=0.1°. Hai was sat to 0.038 °.

The next guide is still 650Åhigh, but now nominally 2000Åin width, which means that guiding can take place in both directions. Frames from the vertical scan of incidence angel are depicted in figure 9.18. The fact that the guide has the same height as the previous, means that the guiding in this direction is expected to be similar to what we observed above.
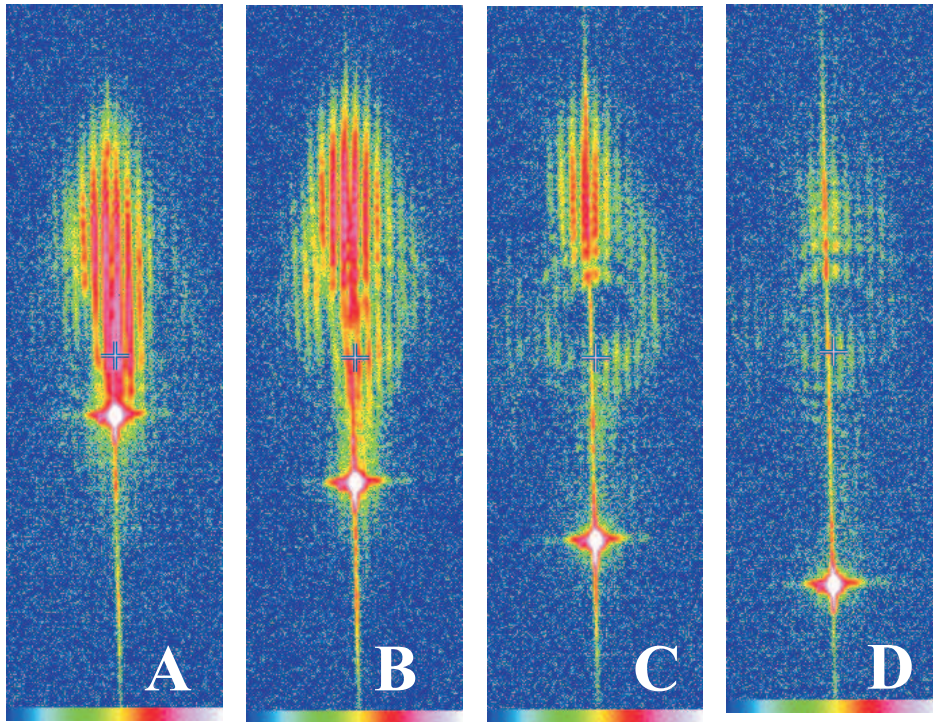

Figure 9.18: Far-field intensities measured in two dimensions with a CCD camera for a 2000Åwide guide, when the vertical incidence angle (hai) is scanned. The selected frames correspond to calculated incidence angles for the four modes. A = 0.039°, B=0.0753°, C=0.113° and D=0.1423°. Hphi=0°.

Comparing figure 9.16 and 9.18 clearly shows that narrowing the width also affects the waveguiding in the vertical direction. The vertical peak position and intensities are, as expected, changing as a function of hai, but the mode seems to be even more displaced than before. Hpi is situated at 0° incidence and in principle if the beam was not divergent and the cavity was perfect, no guiding should be observed in the horizontal plane. This is, however, not the case, and a combination of waveguiding in both directions and intensity contributions due to imperfections of the cavities is observed.

In figure 9.19 - 9.22 the corresponding vertical scans are depicted. The frames are taken at horizontal incidence angles which are calculated for the first four modes for a nominally 2000Åwide guide. Both positive and negative angles are showed.

Figure 9.19: Far-field intensities measured in two dimension with a CCD camera for a 2000Åwide guide, when the horizontal incidence angle (hphi) is scanned. The selected frames correspond to calculated positive and negative incidence angles for the first mode. A = $0.0139°$, B =$-0.0139°$. Hai = $0.038°$.

Figure 9.20: Far-field intensities measured in two dimensions with a CCD camera for a 2000Åwide guide, when the horizontal incidence angle (hphi) is scanned. The selected frames correspond to calculated positive and negative incidence angles for the second mode. C = $0.0278°$, D =$-0.0278°$. Hai = $0.038°$.

Figure 9.21: Far-field intensities measured in two dimensions with a CCD camera for a 2000Åwide guide, when the horizontal incidence angle (hphi) is scanned. The selected frames correspond to calculated positive and negative incidence angles for the third mode. E = 0.0417°, F =-0.0417°. Hai = 0.038°.
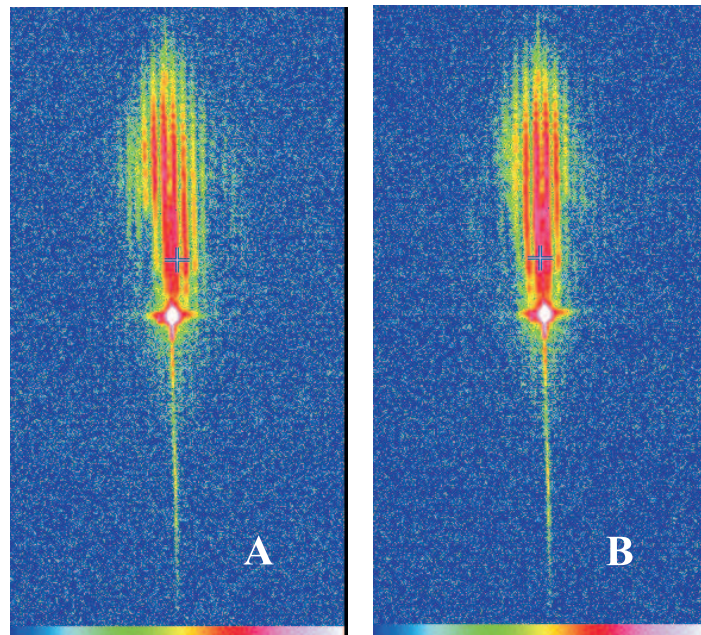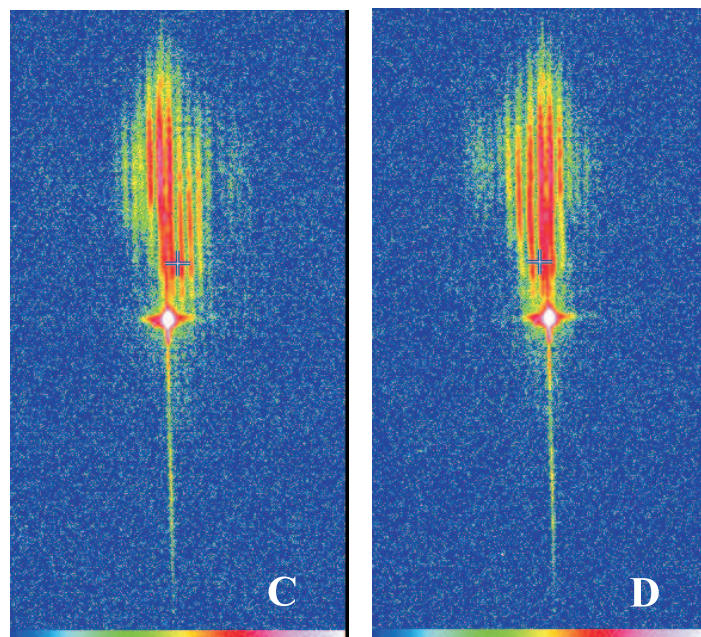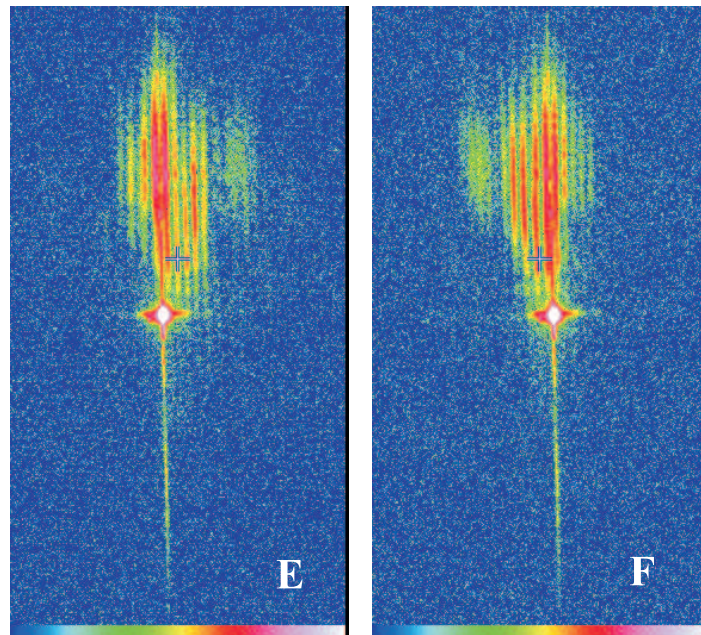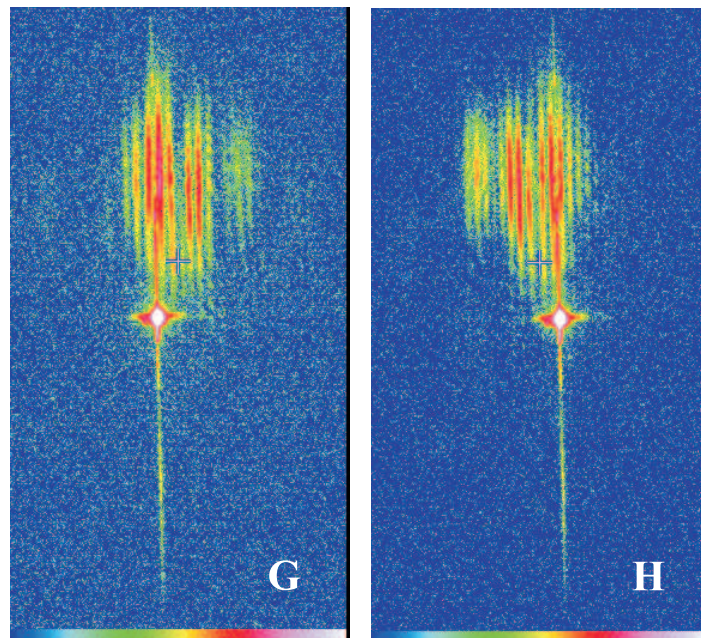

Figure 9.22: Far-field intensities measured in two dimensions with a CCD camera for a 2000Åwide guide, when the horizontal incidence angle (hphi) is scanned. The selected frames correspond to calculated positive and negative incidence angles for the fourth mode. G = 0.0550°, H =-0.0550°. Hai = 0.038°.

As expected the left and right pictures in the figures were almost symmetric and with almost equal observed intensities. Hai is 0.038°, which is the angle corresponding to the guiding of the 0'th mode, whereas guiding in the vertical direction also is expected. The measurements in the four pictures are made at hphi equal to the the calculated incidence angles for the first four modes assuming a width of 2000Å. Because the width is not known for sure, the calculated angles and thereby the shown frame can be off. The unknown width (and shape) also makes it complicated to make a detailed comparison between calculated far-field intensity distributions and recorded intensity patterns.

Frames from a measurement on a second 2000Åwide (650Å) guide is depicted below. In this measurement Hai was 0.055, which is in between the angle of 0'th and 1'st order mode. The frames are selected without calculating incidence angles for the modes.
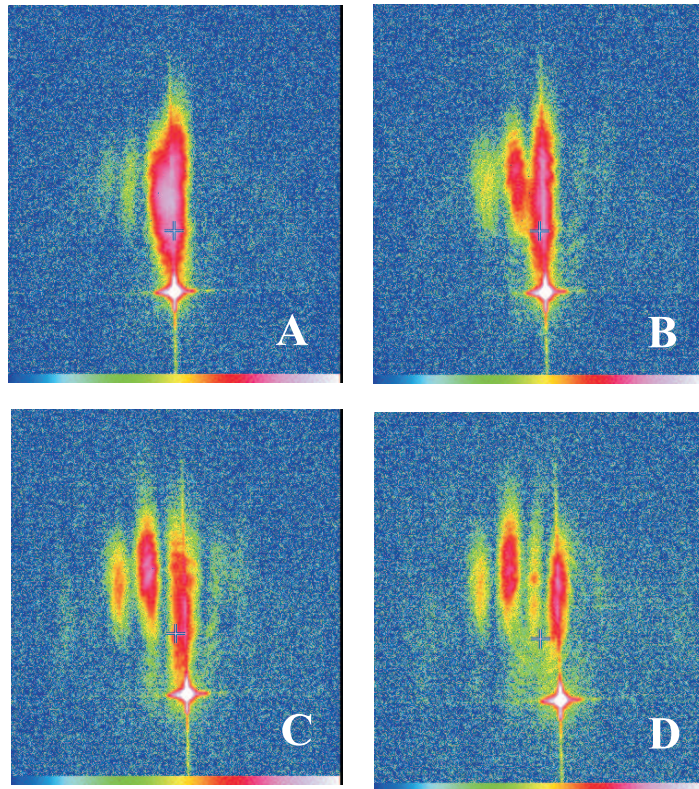
Figure 9.23: Far-field intensities measured in two dimensions with a CCD camera for a 2000Åwide guide for different horizontal incidence angles (hphi). Hai = 0.055°.

In frame A one peak is observed, corresponding to the 0'th order mode. In B the intensity distribution is, as expected for a 1'st order mode, where also some contribution from the 0'th and the 2'nd is observed. In frame C, three peaks are found and in frame D four. The angular spacing between the horizontal incidence angle for the four frames is almost identical, and below what is calculated for a 2000Åwide guide. This indicates that the guide is more than 2000Å.

9.4.3   summary

Several cavities have been measured and general inspections of the video sequences show that the intensity patterns change as a function of the incidence angle and that measured intensity distributions are comparable to what is expected[54] if guiding in both directions in a perfect guide were measured. From the measurements the following can be concluded:

- The width of the cavities were nominally 1000 and 2000Å, but the results of the measurements indicate that they are more likely between 2000 and 4000Å. A more precise way of measuring the width (and shape) should be found, as the width has to be known for the calculations. The depth was 650Å, which is far below what was expected from the etch rate tests. It seems like etching these very small structures has large influence on the etch rate and more time should be spent on tests in order to obtain better control of the depth.

- As the dimensions of the guides were relatively large many modes can be guided, and in the measurement it was not possible to obtain single mode guiding. For this, smaller structures should be made or the guides should be measured at lower energy thereby increasing the mode separation.

- The measured intensities are in general more smeared out when guiding in the horizontal direction. This indicates that the roughness of the sidewalls of the cavity is increased compared to the top and bottom. The observed asymmetry in the horizontal guiding is probably also related to increased roughness. The sidewalls are not perpendicular. From experiments on test structures, an angle of $10°$ or more was found. It is believed that the same range is valid for the etched cavities, and this can have huge influence on the success of performing waveguiding. If an angle of $10°$ is assumed on a 650Ådepth cavity, the difference between width in top and bottom is 230Å. This should be investigated in more detail and alternative etch methods to the RIE could be considered.

- The divergence in the horizontal plane is relatively high, and this in combination with the not vertical side walls will also affect the success of guiding. To investigate this in details the samples could have been rotated 90 $°$. This was unfortunately not tried.

Chapter 10

Conclusion

10.1 Investigations of plasma assisted low temperature bonding

The aim of this work was to obtain structural information about the bonding, which could contribute to a better understanding of the details within the low temperature plasma activation bonding process.

Two reactive etching systems, RIE and ICP-RIE, were tested and the used recipes were optimized in order to obtain the highest possible bond strength. For both types of activation, an optimized recipe resulting in reproducible bond strengths and a high yield of samples without voids was developed, and the bond strengths were high compared to those obtained by other room temperature bonding techniques.

Tests were performed to investigate the reliability and reproducibility of the bond strength measurements. It was found that the ambient air (e.g., the humidity) clearly affects the measurements and should be controlled if more precise values are wanted. Further it would be an improvement if the separation is done automatically instead of manually. If a not optimized system is still used for the test, it would be of great advantage, if at least the measurements conditions and statistics are specified in details.

The oxygen plasma treatment of the surfaces affects the reactivity of the two wafers, and the relationship between changes in the process parameters and the bond strength of bonded wafers was investigated. In general the effect in bond strengths was most sensitive when changing parameters in the RIE system, and within the three investigated parameters, power, pressure and time, changes in power were found to have the most influence.

From the measured reflectivity curves and modelled density profiles clear indications of small density dips close to the Si-SiO$_2$ interface and a dip around the bonding interface

were found. The latter had different shapes depending on the process parameters. In details the correlation between measured density profiles and changes in process parameters is not clear, and we must conclude that additional data sets are needed.

It is known from other similar bonded systems that the observed increase in bond strength as a function of storage time is related to water rearrangement and diffusion, either to bulk or along the interface to the sample edge. Typically the strength increases within the first few days and reaches a stable saturated value often 2-4 times higher than what was observed immediately after bonding. The path length within the narrow stripes used in the set-up is very short and it could be, that for the strips an increased stable bond strength is observed on a much shorter time scale, and already a few hours after cutting no further interface changes are observed. X-ray reflectivity measurements performed and repeated on the same sample within the first few days show identical results and this indicates that no structural changes takes place.

For several samples not only reflectivity from one interface area was measured, but also at different positions along the interface. The results were identical and from this it can be concluded that the reproducibility within each sample is good, and it is believed that the used x-ray geometry is indeed suitable for measuring the buried bonding interfaces.

Outlook

For future experiments the following is suggested:

- Indeed more measurements should be done to reproduce data on bonded wafer samples prepared identically, with specific activation parameters.
- Also measurements on small pieces of activated single wafers should be performed (Small pieces are not expected to bend as much as whole wafers), as these data are more easy to interpret, and can be used as input parameters in the fitting of the data for the bonded samples. In this way it would be possible to compare the fitted density profiles of the thin oxide film before and after bonding as well as investigate structural differences.
- Further it is suggested[21] that chemical analysis with an electron microscope can be invoked by electron energy-loss spectrometry, energy filtered TEM and scanning TEM. Also a detailed study of the interface by EELS will be of great advance in the search for a detailed model of the atomic structure of the plasma assisted room temperature bonding.

10.2 Fabrication and characterization of x-ray waveguides made by wafer bonding

The goal of this part of the work was to fabricate and characterize x-ray waveguides made by using standard silicon process technologies in combination with hydrophobic

wafer bonding.

The etched structures fabricated for guiding in one dimension were made by using standard UV-lithography and RIE etching. Cavities of different depths were made by adjusting the etch time. The expected depths were in good agreement with values found by x-ray reflectivity measurements, and due to this good control of the etching rate it was possible to fabricate cavities of arbitrary depths. The roughness of the bottom was investigated by AFM and was found to be relatively low, which is important for successful waveguiding. The quality of the cavity sidewalls was not influencing the ability for one dimensional guiding.

The cavities were closed by hydrophobic bonding. The bonding process is very sensitive to surface contamination and the process steps made for etching the structures should be done carefully. The roughness of the area between the cavities was also investigated by AFM. It was found to be tiny increased, but still low enough to obtain good contact to the top wafer. IR inspections of the bonded wafer pair were done after the room temperature bonding and in general good results were observed with low amounts of voids. The bonded cavities were annealed for 30 minutes at a 1000 degrees without any problems.

Theoretical considerations about bonding of structured wafers were made, and bonding of structures with the chosen dimension was found to have a raised possibility of collapsing. This, however, was not observed, and from the x-ray transmission scans it could be confirmed that the wafers were nicely bonded in between the cavities and had the expected width.

Several structures with different depth were measured and waveguiding were successfully observed. The measured far-field intensities were compared to what was expected from theoretical calculations and good agreement was found.

We observed a certain overlap of modes which is probably related to the quality of the structures and the divergence of the beam. Further the measured intensities were found to be depending on the length of the guide. The coupling was made directly at the front. This is not an optimal solution, and resulted in relatively low intensities. As a consequence waveguides with a plateau in the front were made. This enlarged the part of the beam entering the guide. However, this was not an optimal solution either, and it is therefore suggested that a pre-focussing system should be incorporated instead.

The two dimensional guides were fabricated using an almost identical process except that e-beam lithography was needed to get sufficiently narrow structures. For the two dimensional guides the quality of the sidewall becomes important, but due to the small widths it was not possible to examine the roughness and shape in detail.

Two dimensional waveguiding was observed, and the measured intensity distributions were comparable to what was theoretically expected if guiding in both directions in

a perfect guide. The results of the measurements indicate that the quality of the sidewall is considerably lower than that in the top and the bottom. Further, we had some problems measuring the exact widths, which made the comparison to theoretical expectations difficult.

The dimensions of the guides were relatively large, whereas the angular spacing between the different modes was small. In the measurement a mix of modes was observed, and if single mode guiding is wanted, either smaller structures should be made or the guides should be measured at lower energy thereby increasing the angular spacing.

Outlook

In order to improve the success of waveguiding in the cavities a number of future experiments are suggested:

- The width of the cavities were nominally 1000 and 2000 Å, but the results of the measurements indicate that they are more likely between 2000 and 4000 Å. A more precise way of measuring the width (and shape) should be found, as the width has to be known for the calculations.

- More tests should be done related to the etching of the structures, both for improving the roughness, the sidewall quality and the control of the depth. Alternatively other etching methods could be considered.

- For the measurement on the two dimensional guides, the divergence of the beam in the horizontal plane is relatively high. This in combination with the not vertical side walls will restrict the success of guiding. To investigate this in details, the samples should have been rotated 90 °, thereby separating the effect from the sidewall from the effect of high divergence.

  Further the fabricated structure should be measured at lower energies. This will increase the angular spacing of modes, making single mode guiding possible. When measuring at higher energies the dimension of the structures has to be very small if the single mode guiding is wanted.

Bibliography

[1] R.A. Alberty and R.J. Silbey, *Physical chemistry*, Jonh Wieley & Sons, Inc., 1996.

[2] J. Als-Nielsen and D. McMorrow, *Elements of modern x-ray physics*, Wiley, 2001.

[3] P. Amirfeiz, S. Bengtsson, M. Bergh, E. Zanghellini, and L. Borjesson, *Formation of silicon structures by plasma-activated wafer bonding*, Journal of the Electrochemical Society **147** (2000), no. 7, 2693–2698 (English).

[4] J. Bagdahn, M. Petzold, M. Reiche, and K. Gutjarh, *Proceedings of the fourth international symposium on semiconductor wafer bonding*, The electrochemical society (1997), 291–298.

[5] B. Bataillou, H. Moriceau, and F. Rieutord, *Direct inversion of interfacial reflectivity using the patterson function*, Journal of Applied Crystallography **36** (2003), no. 6, 1352–5.

[6] H. Baumann, S. Mack, and H. Munzel, *Bonding of structured wafers*, Proceedings of the Third International Symposium on Semiconductor Wafer Bonding: Physics and Applications (1995), 471–87 (English).

[7] S. Bengtsson and P. Amirfeiz, *Room temperature wafer bonding of silicon, oxidized silicon, and crystalline quartz*, Journal of Electronic Materials **29** (2000), no. 7, 909–915 (English).

[8] A. Berthold, B. Jakoby, and M.J. Vellekoop, *Wafer-to-wafer fusion bonding of oxidized silicon to silicon at low temperatures*, Sensors and Actuators A: Physical **68** (1998), no. 1-3, 410–413.

[9] Y. Bertholet, F. Iker, J.P. Raskin, and T. Pardoen, *Steady-state measurements of wafer bonding cracking resistance*, Sensors and Actuators A **110** (2004), 157–163.

[10] J.K. Bhardwaj and H. Ashraf, *Advanced silicon etching using high density plasma*, SPIE **2639**, no. 224.

[11] O. Bunk, BW2 notes, Risø National Laboratory - AFM, Frederiksborgvej 399, DK-4000 Roskilde, o.37 edition, 2003, http://www.fys.risoe.dk/public/bw2.

[12] Oliver Bunk, *Synopsis on planar waveguide measurements*, BW2, Hamborg, August 2003.

[13] Oliver' Bunk, *Synopsis on characterization of 1d silicon waveguides produced by wafer-bonding*, BW2, Hamborg, Februar 2004.

[14] D. Buttard, J. Eymery, F. Rieutord, F. Fournel, D. Lubbert, T. Baumbach, and H. Moriceau, *Grazing incidence x-ray studies of twist-bonded si/si and si/sio/sub 2/ interfaces*, Physica B **283** (2000), no. 1-3, 103–107.

[15] D. Buttard, F. Rieutord, J. Eymery, F. Fournel, and B. Bataillou, *Buried hydrophobic silicon bonding studied by high-energy x-ray reflectivity*, Journal of Physics D: Applied Physics **36** (2003), no. 10, A205–A208 (English).

[16] A. Cedola, S. Di Fonzo, W. Jark, S. Lagomarsino, and G. Soullie, *Sub-micrometre coherent beams from x-ray waveguides: Principles and applications*, Journal of Applied Physics **32** (1999), A179–A183.

[17] G. Cha, W.-S. Yang, D. Feijoo, W.J. Taylor, R. Stengl, and U. Gösele, *Silicon wafers with cavities bonded in different atmospheres*, Proceedings of the First International Symposium on Semiconductor Wafer Bonding: Science, Technology and Applications (1992), 249–59 (English).

[18] W.B. Choi, C.M. Ju, B.K. Ju, and M.Y. Sung, *Wafer to wafer direct bonding using surfaces activated by hydrogen plasma treatment*, Proceedings of the IEEE/CPMT International Electronics Manufacturing Technology (IEMT) Symposium (1999), 148 (English).

[19] A. Doll, F. Goldschmidtboeing, and P. Woias, *Low temperature plasma-assisted wafer bonding and bond-interface stress characterization*, Micro Electro Mechanical Systems, 2004. 17th IEEE International Conference on. (MEMS) (2004), 665–668.

[20] V. Dragoi, S. Farrens, P. Lindner, and J. Weixlberger, *Low temperature wafer bonding for microsystems applications*, 27th International Semiconductor Confer-

ence, CAS 2004 and Proceedings of the International Semiconductor Conference, CAS **1** (2004), 199–202 (English).

[21] A. Egebjerg, *Studies of o₂ plasma activated bonding of silicon wafers*, Master's thesis, Copenhagen University, 2004.

[22] The eight international symposium on semicondutor wafer bonding, Spring meeting of The electrochemical Society, May 2005, Quebec, Canada, Private communication.

[23] 38043 GRENOBLE CEDEX 9 FRANCE ESRF (European Synchrotron Radiation Facility), BP 220, www.esrf.fr/UsersAndScience/Experiments/SurfaceScience/ID01/.

[24] J. Eymery, F. Rieutord, F. Fournel, D. Buttard, and H. Moriceau, *X-ray reflectivity of silicon on insulator wafers*, Materials Science in Semiconductor Processing **4** (2001), no. 1-3, 31–33.

[25] Y. P. Feng, H. W. Deckman, and S. K. Sinha, *Mode-mixing in an x-ray thin-film waveguide*, Applied Physics Letters **64** (1993), 930–933.

[26] Y.P. Feng, S.K. Sinha, H. W. Deckman, J.B. Hastings, and D.P. Siddons, *X-ray flux enhancment in thin-flm waveguides using resonant beam couplers*, Physical Review Letters **71** (1993), no. 4.

[27] Y.P. Feng, S.K. Sinha, and E. Fullerton, *X-ray fraunhofer diffraction patterns from a thin-film waveguide*, Appl. Phys. Lett. **67** (1995), no. 11, 3647–3649.

[28] C. Fuhse, A. Jarre, C. Ollinger, J. Seeger, and T. Salditt, *Front-coupling of a pre-focused x-ray beam into a monomodal planar waveguide*, Applied Physical Letters **85** (2004), no. 11, 1907–1909.

[29] B. Geilman Herstrøm, DANCHIP, Technical University of Denmark. Private communication.

[30] D-22603 HAMBURG Germany HASYLAB at DESY(Deutsche Elektronen-Synchrotron), Notkestr 85, www-hasylab.desy.de.

[31] S. Hayashi, D. Bruno, R. Sandhu, and M.S. Goorsky, *X-ray scattering techniques for assessment of iii-v wafer bonding*, Journal of Physics D (Applied Physics) **36** (2003), no. 10A, A236–40.

[32] S. Hayashi, R. Sandhu, M. Wojtowicz, Y. Sun, R. Hicks, and M.S. Goorsky, *Determination of wafer bonding mechanisms for plasma activated sin films with x-ray reflectivity*, Journal of Physics D (Applied Physics) **38** (2005), no. 10A, A174–8.

[33] C. Himcinschi, M. Friedrich, K. Hiller, T. Gessner, and D.R.T. Zahn, *Infrared spectroscopic investigations of the buried interface in silicon bonded wafers*, Semiconductor Science and Technology **19** (2004), no. 5, 579–585 (English).

[34] J. Janting, DELTA Danish Electronics, Ligth & Acustics.

[35] W. Jark, A. Cedola, S. Di Fonzo, M. Fiordelisi, S. Lagomarsino, N.V. Kovalenko, and V.A. Chernov, *High gain beam compression in new-generation thin-film x-ray waveguides*, Applied Physics Letters **78** (2001), no. 9, 1192–4.

[36] W. Jark and S. Di Fonzo, *Prediction of the transmission through thin-film waveguides for x-ray microscopy*, J. Synchrotron Rad. **11** (2004), no. 9, 386–392.

[37] A. Jarre, C. Fuhse, C. Ollinger, J. Seeger, R. Tucoulou, and T. Salditt, *Two-dimensional hard x-ray beam compression by combined focusing and waveguide optics*, Physical review letters (2005).

[38] A. Jarre, T. Salditt, T. Panzner, U. Pietsch, and F. Pfeiffer, *White beam x-ray waveguide optics*, Applied Physics Letters **85** (2004), no. 2, 161–163.

[39] E.C. Jones and S.W. Bedell, *Advanced applications of wafer bonding*, Silicon wafer bonding technology for VLSI and MEMS applications (2002), 93–121 (English).

[40] K. Jonsson, J. Kohler, C. Hedlund, and L. Stenmark, *Oxygen plasma wafer bonding evaluated by the weibull fracture probability method*, Journal of Micromechanics and Microengineering **11** (2001), no. 4, 364–370 (English).

[41] M. Madou, *Fundamentals of microfabrication*, CRC Press, 1997.

[42] D. Marcuse, *Theory of dielectric optical waveguides*, Academic, New York, (1974).

[43] T. Martini, J. Steinkircher, and U. Gösele, *The crack opening method in silicon wafer bonding. how useful is it*, Journal of the Electrochemical Society **144** (1997), no. 1, 354–357.

[44] S.A. McAuley, H. Ashraf, L. Atabo, A. Chambers, S. Hall, J. Hopkins, and G. Nicholls, *Silicon micromachining using a high-density plasma source*, Journal of Physics D: Applied Physics **34** (2001), no. 18, 2769–2774 (English).

[45] T.A. Michalske and B.C. Bunker, *Slow fracture model based on strained silicate structures*, J. Appl. Phys. **56** (1984), 2686–2693.

[46] A. Milekhin, M. Friedrich, K. Hiller, M. Wiemer, T. Gessner, and D.R.T. Zahn, *Characterization of low-temperature wafer bonding by infrared spectroscopy*, Journal of Vacuum Science and Technology B: Microelectronics and Nanometer Structures **18** (2000), no. 3, 1392–1396 (English).

[47] M. Nielsen, M. Poulsen, O. Bunk, C. Kumpf, R. Feidenhans'l, R.L. Johnson, F. Jensen, and F. Grey, *Mapping strain fields in ultrathin bonded si wafers by x-ray scattering*, Applied Physics Letters **80** (2002), no. 18, 3412–14.

[48] M.M. Nielsen, *Refractive index database*, Risø National laboratory - POL.

[49] OKMETIC, http://www.okmetic.com.

[50] D. Pasquariello, *Plasma-assisted low temperature semiconductor wafer bonding*, Ph.D. thesis, Uppsala University, 2001.

[51] D. Pasquariello, C. Hedlund, and K. Hjort, *Oxidation and induced damage in oxygen plasma in situ wafer bonding*, Journal of The Electrochemical Society **147** (2002), 2699.

[52] D. Pasquariello, M. Lindeberg, C. Hedlund, and K. Hjort, *Surface energy as a function of self-bias voltage in oxygen plasma wafer bonding*, Sensors and Actuators, A: Physical **82** (2000), no. 1, 239–244 (English).

[53] F.L. Pedrotti and L.S. Pedrotti, *Introduction to optics*, Prentice-Hall, 1993.

[54] F. Pfeiffer, *X-ray and neutron waveguides*, Ph.D. thesis, University of Saarbrcken, 2002.

[55] F. Pfeiffer, C. David, M. Burghammer, C. Rickel, and T. Salditt, *Two-dimensional x-ray waveguides and point sources*, Science **297** (2002), 230–233.

[56] Cam plus Micro Tantec Inc., Contact angle meter, www.tantecusa.com.

[57] M. Poulsen, A. Egebjerg, O. Bunk, M. Nielsen, M.M. Nielsen, R. Feidenhans'l, and F. Jensen, *Towards a microscopic understanding of plasma activated bonding*, Semiconductor Wafer Bonding VII: Science, Technology, and Applications - Proceedings of the International Symposium and Electrochemical Society Proceedings **19** (2003), 248–258 (English).

[58] M. Poulsen, F. Jensen, O. Bunk, R. Feidenhans'l, and D.W Breiby, *Silicon waveg-uides produced by wafer bonding*, Applied Physics Letter **87** (2005), 261904–1.

[59] M. Poulsen, F. Jensen, O. Bunk, R. Feidenhans'l, D.W Breiby, and A. Jensen, *Two-dimensional x-ray waveguides made by wafer bonding*, Article in progress.

[60] Lord Rayleigh, *A study of glass surfaces in optical contact*, Proceedings of the Royal Society of London. Series A, Mathematical and Physical Sciences **156** (1936), no. 888, 326–349.

[61] M. Reiche, M. Wiegand, and U. Gösele, *Infrared spectroscopic analysis of plasma-treated si(100)-surfaces*, Mikrochimica Acta **133** (2000), no. 1-4, 35–43.

[62] F. Rieutord, J. Eymery, F. Fournel, D. Buttard, R. Oeser, O. Plantevin, H. Moriceau, and B. Aspar, *High-energy x-ray reflectivity of buried interfaces created by wafer bonding*, Physical Review B (Condensed Matter and Materials Physics) **63** (2001), no. 12, 125408/1–5.

[63] F. Rieutord, H. Moriceau, C. Bataillou, B. Moreles, and J. Eymery, Semiconduc-tor Wafer Bonding VII: Science, Technology, and Applications - Proceedings of the International Symposium and Electrochemical Society Proceedings **2005-02** (2005), 338–345 (English).

[64] A. Sanz-Velasco and P. Amirfeiz, Solid State Electronic Laboratory at Chalmers Tecnical University, Göteborg, Sweden. Private communication.

[65] A. Sanz-Velasco, P. Amirfeiz, S. Bengtsson, and C. Colinge, *Room temperature wafer bonding using oxygen plasma treatment in reactive ion etchers with and without inductively coupled plasma*, Journal of the Electrochemical Society **150** (2003), no. 2, G155–G162 (English).

[66] E. Spiller and A. Segemüller, *Propagation of x-rays in waveguides*, Appl. Phys. Lett. **24** (1974), no. 60.

[67] T. Suga, T.H. Kim, and M.M.R. Howlader, *Combined process for wafer direct bonding by means of the surface activation method*, Electronic Components and Technology, 2004. ECTC '04. Proceedings (2004), 484–490 Vol.1.
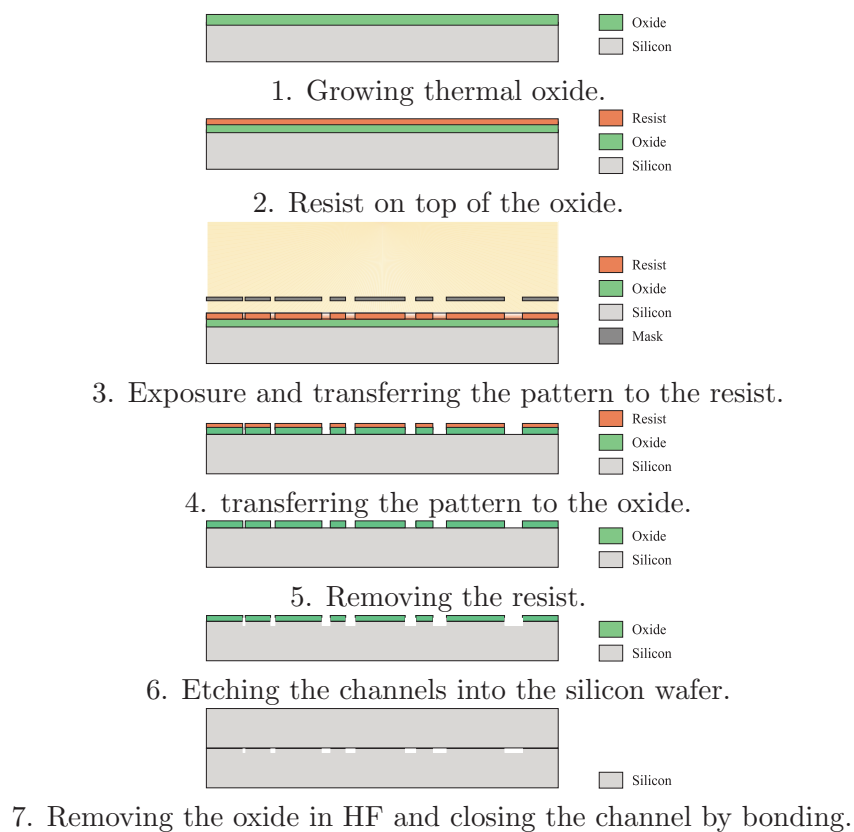
[68] G.-L. Sun, J. Zhan, Q.-Y. Tong, S.-J. Xie, Y.-M. Cai, and S.-J. Lu, *Cool plasma activated surface in silicon wafer direct bonding technology*, Journal de Physique Colloque **49** (1988), no. C-4, 79–82.

[69] T. Suni, VTT Information Technology, Espoo, Finland. Private communication.

[70] Q.-Y. Tong and U. Gösele, *Semiconductor wafer bonding: Science and tecnology*, John Wiley & Sons, Inc., 1999.

[71] Parratt32 v.1.5, Hahn Maitner Institut, The Berlin Neutron Scattering center.

[72] Ö. Vallin, K. Johnson, and U. Lindberg, *Adhesion quantification methods for wafer bonding*, Materials Sceince and Engenering R 50 (2005), 109–165.

[73] M.M. Visser, S. Weichel, R. de Reus, and A.B. Hanneborg, *Strength and leak testing of plasma activated bonded interfaces*, Sensors and Actuators A: Physical **97-98** (2002), 434–440.

[74] K. Wan, N. Aimard, S. Lathabai, R. Horn, and B Lawn, *Interfacial energy states of moisture-exposed cracks in mica*, Journal of Material Reseach **5** (1990), no. 1, 172–182.

[75] S. Weichel, *Silicon to silicon wafer bonding for microsystem packaging and formation*, Ph.D. thesis, Technical University of Denmark, 2000.

[76] A. Weinert, P. Amirfeiz, and S. Bengtsson, *Plasma assisted room temperature bonding for mst*, Sensors and Actuators A: Physical **92** (2001), no. 1-3, 214–222.

[77] M. Wiegand, M. Reiche, and U. Gösele, *Time-dependent surface properties and wafer bonding of o−2/-plasma-treated silicon (100) surfaces*, Journal of the Electrochemical Society **147** (2000), no. 7, 2734–2740 (English).

[78] M.L. Williams, *Continuum interpretation for fracture and adhesion*, Journal of Applied Polymer Science **13** (1969).

[79] X. Zhang and J.-P. Raskin, *A dynamic study for wafer-level bonding strength uniformity in low-temperature wafer bonding*, Electrochemical and Solid-State Letters **8** (2005), no. 10, G268–G270 (English).

[80] M. J. Zwanenburg, J. F. Peters, J. H. H. Bongaerts, S. A. de Vries, D. L. Abernathy, and J. F. van der Veen, *Coherent propagation of x-rays in a planar waveguide with a tunable air gap*, Physical review Letters **82** (1999), no. 8, 1696–1699.

[81] M. J. Zwanenburg, F. van der Veen, H. G. Ficke, and H. Neerings, *A planar x-ray waveguide with a tunable air gab for the structural investigation of confied fluids*, Review of scientific instruments **71** (2000), no. 4, 1723–1732.

Appendix A

Process step overview for waveguide fabrication

A.1 UV-process - one dimensional guides

Oxide
Silicon

1. Growing thermal oxide.

Resist
Oxide
Silicon

2. Resist on top of the oxide.

Resist
Oxide
Silicon
Mask

3. Exposure and transferring the pattern to the resist.

Resist
Oxide
Silicon

4. transferring the pattern to the oxide.

Oxide
Silicon

5. Removing the resist.

Oxide
Silicon

6. Etching the channels into the silicon wafer.

Silicon

7. Removing the oxide in HF and closing the channel by bonding.

A.2   e-beam process- two dimensional guides

1. Dry oxidation, t_{oxid} = 200nm
   Polysilicon, t_{poly} = 100nm.

2. 100nm ZEP700A resist.

3. E-beam litografi at CHALMERS.

4. RIE etch of polySi.

5. Removal of resist. Further
   RIE etch of polySi.

6. RIE etch of Oxide.

7. RIE etch of Si.

8. Remove Oxide in 5%HF

9. Bonding + Annealing 30 min
   at 1000 ^{0}C.

Appendix B

Examples of measurements on one dimensional waveguides

B.1 Measurements on 454Å high guides

The expected mode number and positions are calculated from the theory, and for a 545Å guide three modes were expected.

x	α_i	mode number
2.431	0.0605	0
4.778	0.1190	1
6.777	0.1688	2

Table B.1: Transcendental equation parameter x and corresponding incidence angle α_i at E = 10keV, for a 454Å guide.

Calculated and examples of measured far field intensities for the 454Å guide:
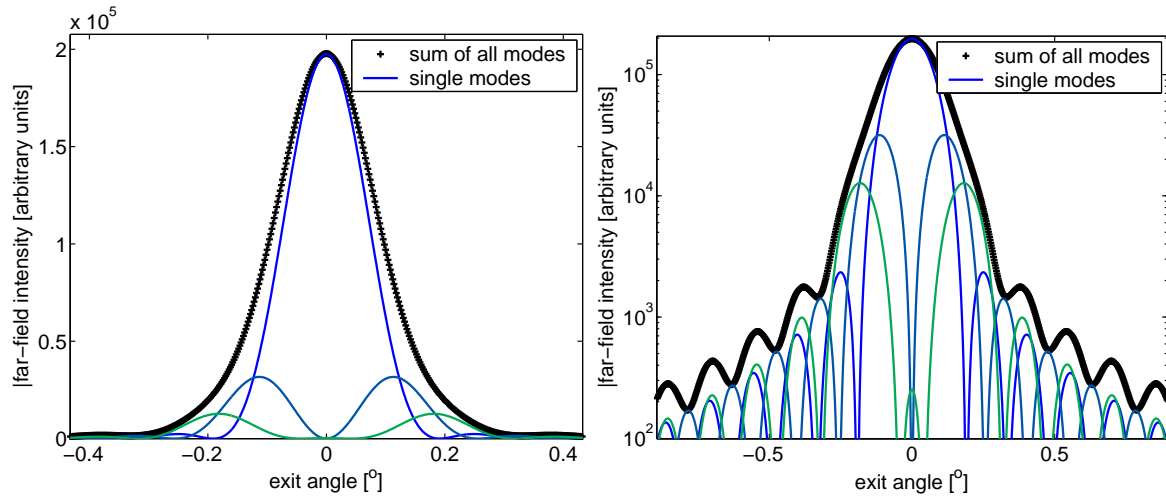
Figure B.1: Calculated far-field intensities for a 454 Å high guide on linear and logarithmic scale.
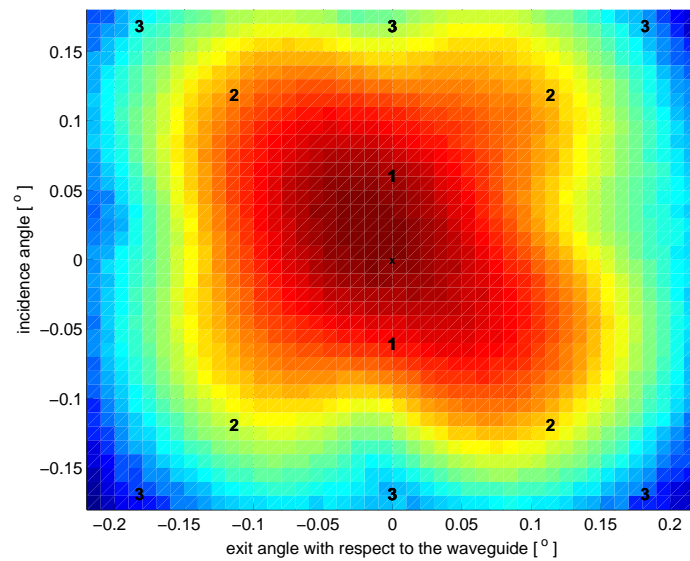
Figure B.2: Measured farfield intensity map for a 454Å high, 3mm long and 100μm wide guide. Intensity ratio is 0.47.
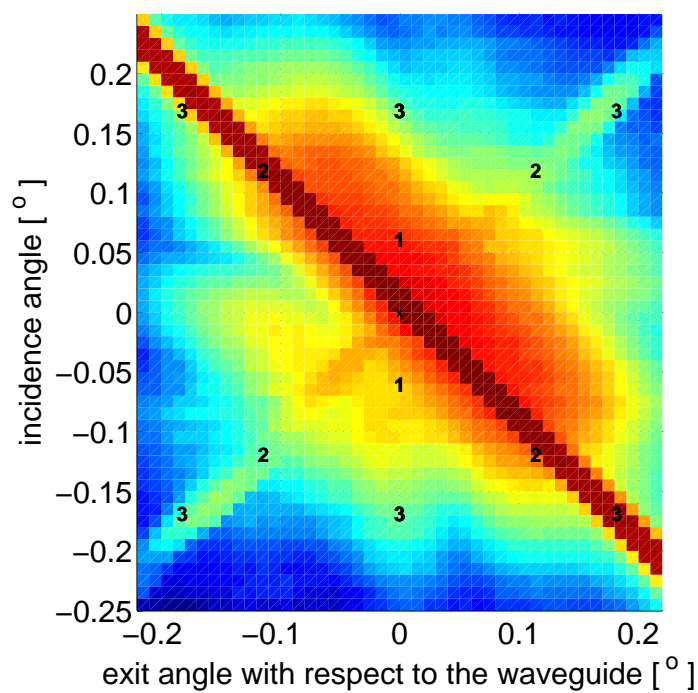
Figure B.3: Measured farfield intensity map for a 454Å high, 1mm long and 100μm wide guide. Intensity ratio is 2.05
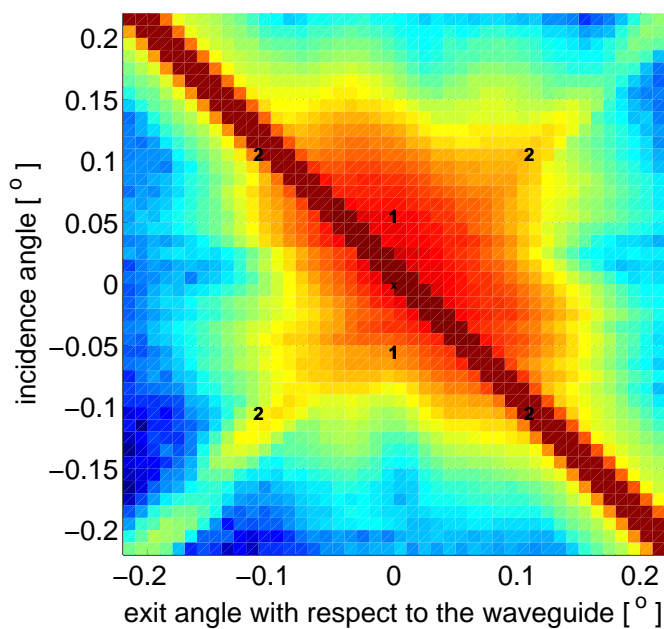

Figure B.4: Measured farfield intensity map for a 454Å high, 1 mm long and 100μm wide guide with ethylene glycol. Intensity ratio is 1.78.

B.2   Measurements on 1351Å high guides

The expected mode number and positions are calculated from the theory, and for a 1351Å guide seven modes were expected.

x	α_i	mode number
2.865	0.0240	0
5.725	0.0479	1
8.575	0.0718	2
11.405	0.0954	2
14.204	0.1189	2
16.945	0.1418	2
19.537	0.1636	2

Table B.2: Transcendental equation parameter x and corresponding incidence angle α_i at E = 10keV, for a 454Å guide.

Calculated and examples of measured far field intensities for the 1351Å guide:
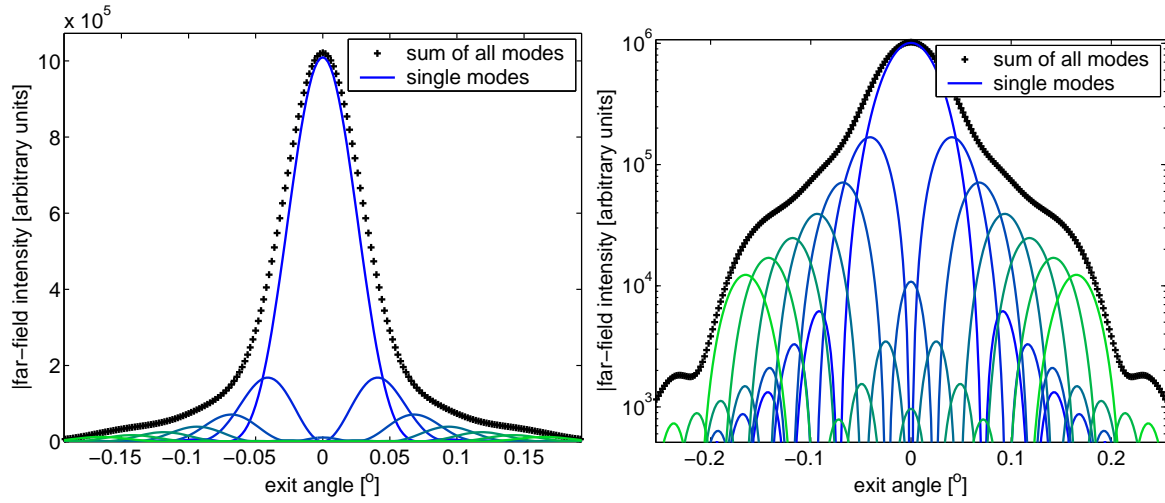

Figure B.5: Calculated far-field intensities for a 454 Å high guide on linear and logarithmic scale.
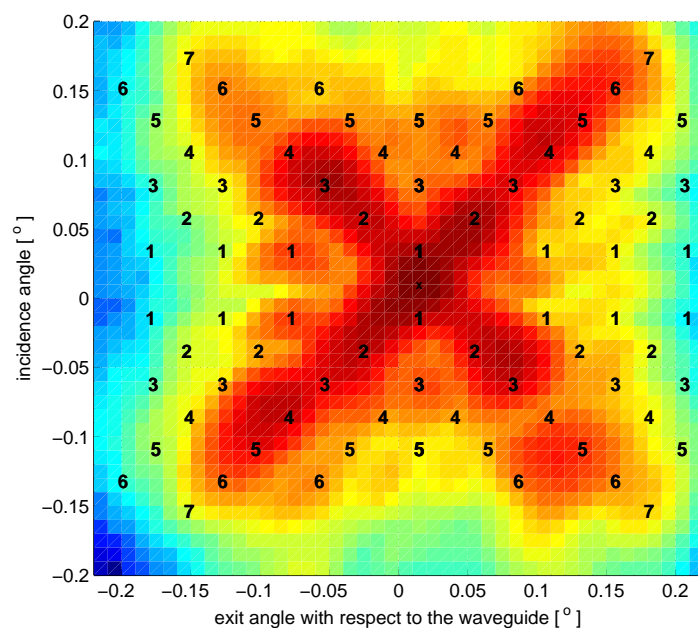
Figure B.6: Measured farfield intensity map for a 1351Å high, 3mm long and 100μm wide guide. Intensity ratio is 0.98
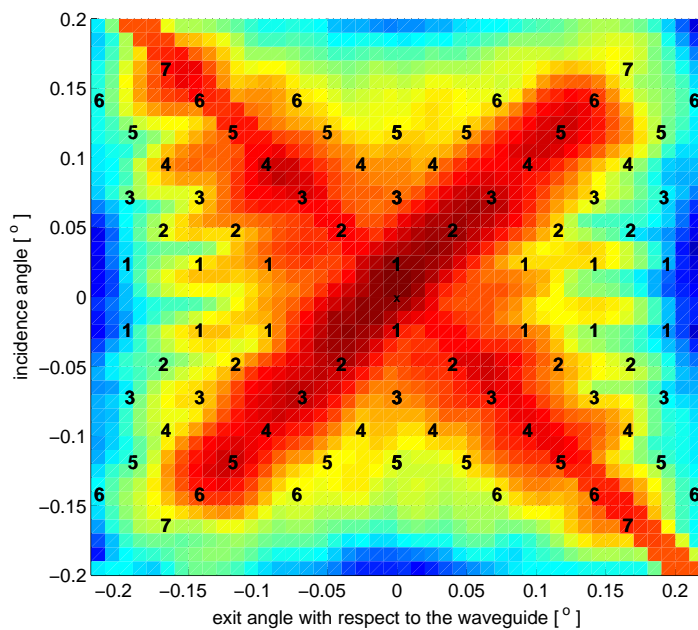

Figure B.7: Measured farfield intensity map for a 1351Å high, 1mm long and 100μm wide guide. Intensity ratio is 1.23

Appendix C

Articles

C.1 Silicon Waveguides produced by Wafer Bonding

.

side 2/3 artikel 1

side 3/3 artikel 1

C.2 Towards a Microscopic Understanding of Plasma Assisted Bonding

.

side 2/11 artikel 1

side 3/11 artikel 1

side 4/3 artikel 1

side 5/3 artikel 1

side 6/3 artikel 1

side 7/3 artikel 1

side 8/3 artikel 1

side 9/3 artikel 1

side 10/3 artikel 1

side 11/3 artikel 1

C.3   Mapping Strain Fields in Ultrathin Bonded Si Wafers by X-ray Scattering

.

side 2/3 artikel 1

side 3/3 artikel 1